Max-Planck-Institut
für Meteorologie

MAX-PLANCK-GESELLSCHAFT

International Max Planck Research School
on Earth System Modelling

Analysis of Arctic Sea-Ice Leads from Advanced Microwave Scanning Radiometer

David Alexander Bröhan

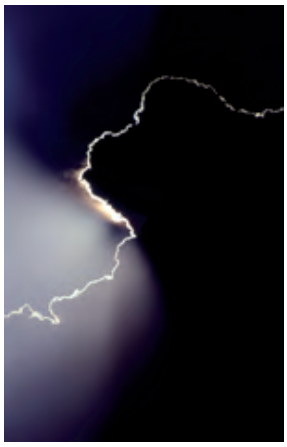

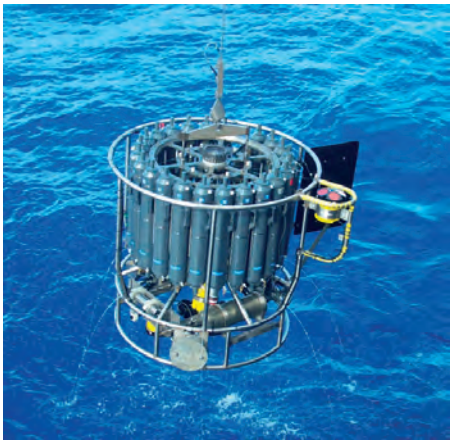

Berichte zur Erdsystemforschung 153/2014

Reports on Earth System Science

Hinweis

Die Berichte zur Erdsystemforschung werden vom Max-Planck-Institut für Meteorologie in Hamburg in unregelmäßiger Abfolge herausgegeben.

Sie enthalten wissenschaftliche und technische Beiträge, inklusive Dissertationen.

Die Beiträge geben nicht notwendigerweise die Auffassung des Instituts wieder.

Die "Berichte zur Erdsystemforschung" führen die vorherigen Reihen "Reports" und "Examensarbeiten" weiter.

Notice

The Reports on Earth System Science are published by the Max Planck Institute for Meteorology in Hamburg. They appear in irregular intervals.

They contain scientific and technical contributions, including Ph. D. theses.

The Reports do not necessarily reflect the opinion of the Institute.

The "Reports on Earth System Science" continue the former "Reports" and "Examensarbeiten" of the Max Planck Institute.

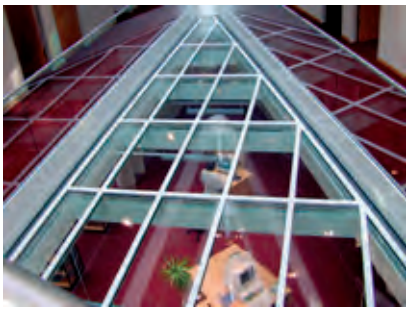

Anschrift / Address

Max-Planck-Institut für Meteorologie
Bundesstrasse 53
20146 Hamburg
Deutschland

Tel.: +49-(0)40-4 11 73-0
Fax: +49-(0)40-4 11 73-298
Web: www.mpimet.mpg.de

Layout:

Bettina Diallo, PR & Grafik

Titelfotos:
vorne:
Christian Klepp - Jochem Marotzke - Christian Klepp
hinten:
Clotilde Dubois - Christian Klepp - Katsumasa Tanaka

Berichte zur Erdsystemforschung 153/2014

Analysis of Arctic Sea-Ice Leads from Advanced Microwave Scanning Radiometer

David Alexander Bröhan

aus Buxtehude, Deutschland

Hamburg 2014

Reports on Earth System Science 153/2014

ISSN 1614-1199

David Alexander Bröhan
Max-Planck-Institut für Meteorologie
Bundesstrasse 53
20146 Hamburg

Als Dissertation angenommen
vom Fachbereich Geowissenschaften der Universität Hamburg

auf Grund der Gutachten von
Prof. Dr. Lars Kaleschke
und
Dr. Dirk Notz

Hamburg, den 26. Mai 2014
Professor Dr. Christian Betzler
Leiter des Departments Geowissenschaften

ISSN 1614-1199

Analysis of Arctic Sea-Ice Leads from Advanced Microwave Scanning Radiometer

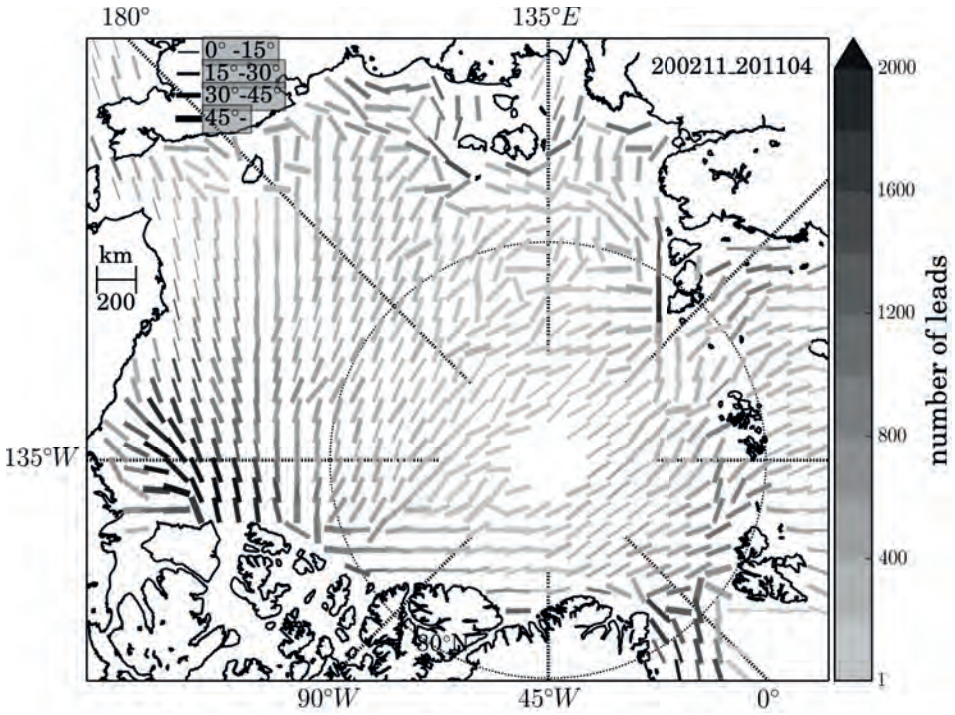

David Alexander Bröhan

Hamburg 2014

Abstract

In this thesis, we infer the fractional coverage of sea-ice leads (as concentration) in the Arctic from Advanced Microwave Scanning Radiometer for Earth Observing System (AMSR-E) brightness temperatures. The resulting lead concentration resolves large leads of at least 3 km in width. We compare the lead concentration to leads detected from Advanced Synthetic Aperture Radar (ASAR) and CryoSat-2 data. ASAR and CryoSat-2 measurements indicate that a lot more small-scale leads exist than are resolved in the AMSR-E based lead concentration map. However, almost every lead resolved by the lead concentration is confirmed by CryoSat-2 and ASAR measurements. We develop a new algorithm based on the progressive probabilistic Hough transform to automatically infer lead positions and orientations from daily lead concentration maps. Because the progressive probabilistic Hough transform often detects a single lead several times, the new algorithm clusters neighboring leads that belong to a single lead position. A reliable, but labor-intensive method is to manually infer the lead orientation. A comparison of automatically and manually detected lead positions and orientations reveals that 57% of the reference leads are correctly determined by the new algorithm. About 11% of the automatically detected leads are located where no reference lead occurs. The probability density functions of automatically detected lead orientations and reference lead orientations differ only slightly. Another comparison of automatically detected leads in the Fram Strait to leads discernible in a wide swath mode ASAR scene shows good agreement.

Based on automatically detected leads, we provide an Arctic-wide time series of lead frequency and orientation for the winters from 2002 to 2011. In general, more leads open in the beginning of winter than in the end of winter. Maxima of lead occurrence are located in the Beaufort Sea and the Fram Strait. In the Beaufort Sea, lead orientations are more isotropically distributed, while a lead orientation of 110° with respect to the Greenwich meridian prevails in the Fram Strait. North of Greenland, leads are orientated parallel to the coast throughout the entire winter. North of Siberia, the lead orientation tilts from coast-perpendicular in the beginning of winter to coast-parallel in the end of winter. By means of Monte Carlo simulations, we find significant preferred lead orientations almost everywhere in the Arctic Ocean when averaged over the entire AMSR-E time series.

We compare the climatology of lead frequency and orientation to the climatology of divergence, vorticity, and shear calculated from the AMSR-E based sea-ice drift. From the weekly to the multi-year time scale, a large divergence and shear rate coincides with a large number of lead occurrences. However, this relationship is not linear: The largest divergence and shear rate do not always coincide with the largest number of leads. The large-scale agreement between lead occurrences and divergence and shear rate is more distinct in the beginning than in the end of winter. In eight out of nine winters, the change of monthly-mean lead orientation follows the rotational drift direction of the surrounding sea ice in the Beaufort Sea. Only throughout the 2007/08 winter, the monthly-mean lead orientation rotates in a direction opposed to the rotational drift direction of the surrounding sea ice. This exceptional pattern coincides with the until then unprecedented minimum in satellite-observed sea-ice extent in fall 2007.

Zusammenfassung

In dieser Arbeit bestimmen wir die Rinnenabdeckung des Meereises (als Konzentration) in der Arktis aus Advanced Microwave Scanning Radiometer for Earth Observing System (AMSR-E) Helligkeitstemperaturen. Die resultierende Rinnenkonzentration löst große Rinnen auf, die breiter als 3 km sind. Wir vergleichen die Rinnenkonzentration mit Rinnen, die aus Advanced Synthetic Aperture Radar (ASAR) und Cryosat-2 Datensätzen bestimmt wurden. ASAR und Cryosat-2 weisen darauf hin, dass viel mehr kleine Rinnen existieren als in den AMSR-E Rinnenkonzentrationskarten aufgelöst werden. Jedoch wird jede Rinne, die in der Rinnenkonzentration auftaucht, durch ASAR und Cryosat-2 Messungen bestätigt.

Wir entwickeln einen neuen Algorithmus, der auf der sogenannten progressive probabilistic Hough Transformation basiert, um automatisch Rinnenposition und -ausrichtung aus täglichen Rinnenkonzentrationskarten zu ermitteln. Da die progressive probabilistic Hough Transformation oft eine Rinne mehrmals detektiert, fasst der neue Algorithmus benachbarte Rinnen, die zu einer Rinne gehören, zusammen. Eine zuverlässige, aber arbeitsaufwändige Methode ist es, Rinnen manuell zu ermitteln. Ein Vergleich von automatisch und manuell ermittelten Rinnenpositionen und -ausrichtungen ergibt, dass der neue Algorithmus 57% der Referenzrinnen richtig erkennt. Ungefähr 11% der automatisch detektierten Rinnen befinden sich dort, wo keine Referenzrinne vorkommt. Die Wahrscheinlichkeitsdichtefunktionen der automatisch detektierten Rinnenausrichtung und der Referenzrinnenausrichtung unterscheiden sich nur wenig. Ein weiterer Vergleich von automatisch detektierten Rinnen in der Framstraße mit Rinnen, die in sogenannten wide swath mode ASAR Szenen erkennbar sind, zeigt eine gute Übereinstimmung.

Wir verwenden die automatisch detektierten Rinnen, um eine arktisabdeckende Zeitreihe für Rinnenfrequenz und -ausrichtung für die Winter von 2002 bis 2011 zu erzeugen. Im Allgemeinen öffnen sich mehr Rinnen am Anfang als am Ende eines Winters. Maxima des Rinnenauftretens befinden sich in der Beaufortsee und in der Framstraße. In der Beaufortsee sind Rinnen eher isotrop verteilt, während in der Framstraße eine Rinnenausrichtung von 110° relativ zum Nullmeridian vorherrscht. Nördlich von Grönland sind Rinnen den ganzen Winter über parallel zur Küste ausgerichtet. Nördlich von Sibirien drehen sich die Rinnen von einer Ausrichtung senkrecht zur Küste am Anfang des Winters auf eine Ausrichtung parallel zur Küste zum Ende des Winters. Monte-Carlo-Simulationen zeigen, dass überall in der Arktis eine bevorzugte Rinnenausrichtung vorherrscht, wenn über die gesamte AMSR-E Zeitreihe gemittelt wird.

Wir vergleichen die Klimatologie der Rinnenfrequenz und -ausrichtung mit der Klimatologie von Divergenz, Wirbelstärke und Scherung, die aus der AMSR-E Meereisdrift berechnet wird. Auf der wöchentlichen bis mehrjährigen Zeitskala treten hohe Divergenz- und Scherungsraten zusammen einer hohen Anzahl an Rinnen gleichzeitig auf. Allerdings ist der Zusammenhang nicht linear: Die höchsten Divergenz- und Scherungsraten treten nicht immer mit der höchsten Anzahl an Rinnen auf. Die großräumige Übereinstimmung von Rinnenauftreten mit Divergenz- und Scherungsrate ist am Anfang des Winters ausgeprägter als am Ende. In acht von neun Wintern folgt die Änderung der Rinnenausrichtung in der Beaufortsee der Drehrichtung des

driftenden Meereises. Nur im Winter 2007/08 dreht sich die monatlich gemittelte Rinnenausrichtung entgegengesetzt zu der Drehrichtungsänderung des umgebenden Meereises. Dieses außergewöhnliche Muster fällt mit der bis dahin geringsten von Satelliten beoabachteten Meereisausdehnung im Herbst 2007 zusammen.

Contents

Chapter 1

Introduction

A sea-ice lead is defined by the World Meteorological Organisation (WMO) as a rectilinear or wedge-shaped crack in the sea-ice cover. According to this definition, a lead is wider than 50 m and ranges from several kilometers to hundreds of kilometers in length. The term lead is often used more generally as a synonym for a linear kinematic feature which describes different types of openings in the Arctic sea-ice cover like polynya, crack, fracture, and failure zone (Kwok, 2001; Hutchings et al., 2005).

Leads matter for several reasons: Although leads traverse only a very small fraction of the Arctic sea-ice cover, they dominate heat fluxes at the ocean-ice-atmosphere interface (Smith et al., 1990; Pinto et al., 2003). For example, Lüpkes et al. (2008) found in a modeling study that a change of 1% in lead coverage could result in a near-surface air temperature signal of up to 3.5 K for clear-sky conditions during polar night. Marcq and Weiss (2012) showed that turbulent heat transfers between ocean and atmosphere strongly depend on the distribution of leads in oceans covered with sea ice. Furthermore, the exchange of CO_2 is much more efficient in cracks or leads than expected under similar conditions for open water (Steiner et al., 2013). Leads are also a major source for brine release to the ocean and they are important for Arctic wildlife (Smith et al., 1990) to name just a few implications of leads.

A lead reflects and influences sea-ice dynamics (Lindsay and Rothrock, 1995). In this thesis, we focus on the dynamical effects of leads. Leads contain information about how sea ice is influenced by surface winds, ocean currents, and internal forces in the sea ice. However, only a limited observational record of leads exists. The scope of this thesis is to provide a decade-long time series of lead position, orientation, and frequency for the lifespan of the Advanced Microwave Scanning Radiometer for Earth Observing System (AMSR-E) from 2002 to 2011. For the first time, we introduce a fully automatic method to derive lead orientations. We compare the Arctic lead distribution to the deformation of sea ice on annual to weekly timescales to identify possible interactions.

Lead detection

The overall goal of this thesis is to analyze leads from spaceborne observations and to identify interactions of leads with the Arctic climate. We focus on satellite observations because they provide the best comprehensive picture of the Arctic. The earth emits

radiation in the electromagnetic spectrum. A part of the electromagnetic spectrum is represented by the passive microwave spectrum that extends from frequencies between 0.3 GHz to 300 GHz (1 m to 1 mm in wavelength) (Ulaby et al. (1981), p. 21). In remote sensing, the term 'passive' refers to an instrument that records the terrestial radiation. In order to analyze leads from space, we need an approach that is capable of detecting leads in the sea-ice cover with a sufficient temporal and spatial resolution. We choose passive microwave remote sensing as the best compromise between temporal and spatial resolution. The Advanced Microwave Scanning Radiometer for Earth Observing System (AMSR-E) is mounted on a satellite named Aqua. The instrument scans the microwave radiation (as brightness temperature) at six frequencies ranging from 6.9 GHz to 89 GHz. AMSR-E offers a continuous daily coverage of the entire Arctic combined with a moderate ground resolution of approximately 6 km. Thus, the analysis of leads in this thesis is restricted to large leads because we are using passive microwave measurements. Röhrs et al. (2012) introduced a lead detecting algorithm that is based on AMSR-E measurements.

We use this algorithm to estimate the lead concentration. Before the lead concentration is analyzed, we test the quality of the algorithm. To do so, we raise the following questions: How accurate does the approach by Röhrs et al. (2012) detect leads in comparison to other sensors? What are the major uncertainties? To answer these questions, we compare leads detected by the algorithm of Röhrs et al. (2012) with leads discernible in radar measurements obtained from other satellite sensors. The comparison reveals that the positions of large leads agree for all sensors. All this is shown in chapter 2.

Lead orientation

Both, previous and ongoing research, focus on the localized and temporal limited frequency distribution of leads (Lindsay and Rothrock, 1995; Miles and Barry, 1998; Marcq and Weiss, 2012). Creating a temporal and spatial continuous observational record of lead orientation is still missing. Inferring lead orientation on an Arctic basin-wide scale via remote sensing is not straightforward although observations of lead occurrence can be obtained from optical sensors, altimeters, and synthetic aperture radar. Optical sensors usually have a higher resolution than passive microwave sensors but they are often limited by the occurrence of clouds. Altimeter track profiles alone are not sufficient to estimate the lead orientation. Synthetic aperture radar has a high spatial resolution but the temporal coverage is mostly not continuous. Furthermore, the ambiguity between multi-year ice and frost flowers in lead signatures limits the classification of leads from synthetic aperture radar (Zakhvatkina et al., 2013).

In the face of the aforementioned limitations, we choose the algorithm by Röhrs et al. (2012) based on AMSR-E measurements as input for our approach to estimate the lead orientation. However, other sensors offer a higher spatial resolution. The lead concentration algorithm provides no directional information. Three approaches exist to estimate the orientation of leads. The first approach is to manually infer the orientation from a lead map. The second approach is a semi-automatic detection of lead orientations with still some manual workload involved (Lindsay and Rothrock, 1995). The third approach is to infer lead orientations in an automatic manner from a lead map. Because we aim to estimate a decade-long time series of lead orientations in

winters, the workload which comes with the manual approach is not feasible. Thus, we apply an automatic approach to detect the lead orientation. In most cases, a lead does not appear as an idealized, straight line in a lead concentration map. Leads show often a certain extent of curvature and they are often interrupted. Thus, we estimate and fit a lead to an idealized line in order to infer the lead orientation. The quasi-linear shape of leads challenges approaches to detect lines in images. Image analysis techniques exist to infer lines in images, however most of them are not capable of dealing with quasi-linear line input.

On the way to develop an automatic approach to detect the lead orientation, we study the following questions: What is a suitable approach to detect the orientation of quasi-linear lead structures in lead concentration maps? How do the lead orientations derived from a newly developed approach compare to manually obtained lead orientations? Fetterer and Holyer (1989); Bandfield (1992); Lindsay and Rothrock (1995) tried to develop an approach to automatically infer the lead orientation. Based on their work, we develop a method to automatically infer lead orientations from passive microwave sensors in chapter 3.

Climatology of lead frequency and orientation

Feltham (2008) stated that leads induce anisotropy at the scale of leads in the sea-ice cover because leads are orientated. Nevertheless, sea ice is often considered as isotropic or at least the constitutive laws of continuum-scale sea-ice stress are usually isotropic (Feltham, 2008). Aside from the theoretical convenience of the isotropy assumption, the most compelling argument in the favor of isotropy is that the lead distribution was considered to be nearly isotropic on length scales of 100 km (Rothrock, 1975; Hibler, 1979). However, more recent studies indicate that the lead orientation is more bimodally distributed at least in the Central Arctic (Schulson and Hibler, 1991; Hibler, 2001; Schulson, 2004).

The aforementioned studies draw their conclusions from observations made in certain subregions of the Arctic during a couple of days. These case studies have advantages and disadvantages: On the one hand, the footprint of analyzed Land Satellite (LANDSAT) or Radar Satellite (RADARSAT) scenes is certainly higher than the footprint of AMSR-E, so that the spectrum of leads contains also smaller leads than detectable with passive microwave remote sensing. On the other hand, the conclusions of these studies are based on only a few days of data. We have the advantage of a nine-year observational record from AMSR-E. This allows us to derive a climatology of statistical significant lead positions and orientations that can be prolonged into the future by applying our algorithm to Advanced Microwave Scanning Radiometer 2 (AMSR2) observations. Concerning the lead orientation, we are going to answer the following questions: How do the different spatial distributions of leads change from the monthly to the multi-year timescale? Do we observe anisotropy induced by lead orientations in the mean spatial distribution of leads over nine winters? We present maps depicting the anisotropy induced by lead orientation in chapter 4.

A possible implication of this thesis is that statistically inferred lead orientations add some value for navigating ships through the Arctic Ocean. Furthermore, the derived lead orientations can be used to evaluate lead-resolving sea-ice models. A local structure tensor in a sea-ice model as a measure of the sub-continuum anisotropy (such as

leads) of the sea-ice cover results in substantially changed sea-ice thickness and drift in comparison to a reference run (Tsamados et al., 2013). Girard et al. (2009) concluded that the poor representation of observed sea-ice deformation patterns that represent lead structures in two high-resolution sea-ice models could mainly be attributed to the used mechanical framework. The build-up of leads and the consequent anisotropy of the sea-ice deformation can be captured within an elasto-brittle or an elastic-decohesive framework (Wilchinsky and Feltham, 2004; Girard et al., 2011; Sulsky and Peterson, 2011; Wilchinsky and Feltham, 2012).

Comparison of Arctic Leads to Sea-Ice Deformation

We briefly introduce how leads interact with the deformation of sea ice: Surface wind, ocean current, and internal ice strength determine the rate of sea-ice deformation (Herman and Glowacki, 2012; Heygster et al., 2012). Deformation then generates leads and ridges in the sea-ice cover (Heygster et al., 2012). Most of the times, deformation occurs concentrated and localized at large leads (Marsan et al., 2004) because leads consist of open water and thin ice. Thin ice generally deforms easier than thick ice (Kwok, 2006; Feltham, 2008; Rampal et al., 2009; Stern and Lindsay, 2009). Because leads, consisting of open water and thin ice, are surrounded by thicker ice, leads determine the stresses that can be maintained within the sea-ice cover (Feltham, 2008).

Herman and Glowacki (2012) observed that sea-ice deformation rates are higher in the seasonal sea-ice zones. According to Herman and Glowacki (2012), higher sea-ice deformation rates can be expected for a winter following a summer for which a strong melting occurred because of a smaller mean sea-ice thickness. Herman and Glowacki (2012) found that the occurrence probability for extremely strong deformation events (largest 5% of all deformation events) is significantly higher in the following coastal regions: Along the coast of Alaska, in the East Siberian Sea, and close to the New Siberian Islands. Hutchings et al. (2005, 2011) found that in the Beaufort Sea, leads are organized into coherent structures that are controlled by the confining stress of the pack ice, which is related to wind stress and coastal line geometry. Minima in the occurrence probability for extremely strong sea-ice deformation events are located north of the Canadian Archipelago and partly in the Central Arctic probably caused by a large mean sea-ice thickness and a large resulting internal sea-ice strength (Herman and Glowacki, 2012). Herman and Glowacki (2012) identified two dominating components of variability in the frequency distribution of sea-ice deformation: A seasonal cycle with deformation rates decreasing through winters to a minimum in March and a short-term synoptic variability strongly correlated with the area-averaged wind stress.

Given all this, we expect maxima in lead occurrence and sea-ice deformation in seasonal sea-ice zones and especially in the Beaufort Sea. Furthermore, we expect to observe a coherent seasonal cycle between lead occurrence and sea-ice deformation. Using our decade-long observational record of leads, we ask the following questions: How does the spatial distribution of the sea-ice deformation rate compare to the spatial distribution of lead occurrence? Do we observe connections between the two seasonal cycles of sea-ice deformation and lead occurrence? How does the large-scale lead-orientation pattern compare to the large scale sea-ice deformation?

We use Institut francais de recherche pour l'exploitation de la mer (Ifremer)'s AMSR-E based sea drift (Ezraty et al., 2007) to calculate the deformation parameters. This

sea-ice drift product covers exactly the same time period as the derived lead orientations, because the sea-ice drift is derived from AMSR-E. In order to analyze if sea-ice deformation is localized at large lead structures, we compare lead positions to high-resolution RADARSAT Geophysical Processor System (RGPS) sea-ice drift (Kwok, 1998). We will also touch upon the scale dependence of sea-ice deformation by a comparison of high-resolution RGPS sea-ice deformation to moderate-resolution AMSR-E based sea-ice deformation. Our results indicate an agreement between the two sea-ice drift products on the large scale. Large sea-ice deformation rates agree with the positions of large lead occurrences. All this is shown in chapter 5. We conclude the results of all chapters in chapter 6.

Chapter 2

Introducing and Validating a Lead-Detecting Algorithm[1]

2.1 Introduction

Because leads can open up within several hours, leads consist of open water or young thin ice, when the water is refrozen due to the often below freezing temperatures in the Arctic. Wensnahan et al. (1993) found that in general thin ice can be distinguished from open water, first-year ice, and multi-year ice via a principal component analysis of the thin-ice emission spectra at frequencies of 19 GHz and 37 GHz. However, at that time, the ground resolution of passive microwave measurements from space did not allow one to distinguish between thin ice and first-year ice. Cavalieri (1994) developed a technique to map thin ice by using the vertically polarized components of the near 19 GHz and 37 GHz brightness temperature channels. The technique is limited to seasonal sea-ice zones, and the classification shows mixture ambiguities concerning the classification of the sea-ice type. Röhrs et al. (2012) developed an algorithm that is based on the ratio of the 89 GHz and near 19 GHz vertically polarized Advanced Microwave Scanning Radiometer for Earth Observing System (AMSR-E) brightness-temperature channels. The algorithm detects thin ice at a moderate ground resolution but is restricted to polynyas or leads. We use this algorithm to analyze leads.

Miles and Barry (1998) manually extracted lead characteristics from optical Advanced Very High Resolution Radiometer (AVHRR) satellite observations in the western Arctic for winters from 1979 to 1985. Another study by Lindsay and Rothrock (1995) based on AVHRR measurements inferred lead characteristics with a semi-automatical

[1]Sections 2.2.1 and 2.2.2 introduce the lead detecting algorithm by Röhrs et al. (2012), which has not been developed by the author of this thesis. The lead detecting algorithm is of fundamental importance for this thesis, because it is the base for an analysis of leads in the following chapters. In section 2.3, the author validates the lead detecting algorithm by Röhrs et al. (2012). This is also the author's contribution to the publication:

Röhrs, J., Kaleschke, L., Bröhan, D., and Siligam, P. (2012). An algorithm to detect sea ice leads using AMSR-E passive microwave imagery. The Cryosphere, 6(2):343-352.

Parts of this chapter have been published in this article.

approach throughout the Arctic for the year 1989. Both studies share the same advantages and disadvantages in comparison to the study of Röhrs et al. (2012). On the one hand, both studies incorporate small-scale leads. This is not possible for the approach by Röhrs et al. (2012) because of the limited resolution of a passive microwave sensor. On the other hand, both studies cannot cover the entire Arctic on the daily time-scale. Both studies cover short time slices (five winter seasons and one winter season, respectively). This is due to the high workload of manually detecting leads. Accordingly, a continuing time series of lead observations is still missing. This knowledge gap is filled by Röhrs et al. (2012) by creating an Arctic-wide time series of leads for winters from 2002 to 2011. Still, one trade-off is the limited spatial resolution of 6.25 km × 6.25 km of the AMSR-E based measurements. The successor of AMSR-E, Advanced Microwave Scanning Radiometer 2 (AMSR2) allows one to measure leads at a higher spatial resolution of 3.125 km × 3.125 km, because both (A and B) scans are available (Beitsch and Kaleschke, 2013).

The major research questions of this chapter are: What are the uncertainties that influence the lead detecting algorithm by Röhrs et al. (2012)? Does the lead detecting algorithm by Röhrs et al. (2012) correctly detect lead occurrences in the Arctic sea-ice cover?

This chapter is organized in two major sections. We present the algorithm developed by Röhrs et al. (2012) in sections 2.2.1 and 2.2.2. We mention possible limitations induced by the electromagnetic properties of sea ice on the separation between thin ice and thicker ice from passive microwave remote sensing in section 2.2.3. In section 2.3, we compare the lead observations resulting from the algorithm of Röhrs et al. (2012) to lead observations from other satellite sensors. Section 2.4 follows with a brief discussion and summary of the obtained results.

2.2 Lead Detecting Algorithm by Röhrs et al. (2012)

In this section, we introduce the basic components of the lead detecting algorithm by Röhrs et al. (2012). The algorithm consists mainly of a brightness-temperature ratio, which aids to differ between thin ice and thicker ice in the vicinity of leads. In order to highlight lead structures, Röhrs et al. (2012) applied a median filter on maps of the brightness-temperature ratio. The brightness-temperature ratio is calculated by dividing the near 90 GHz channel by the near 19 GHz brightness temperature channel.

2.2.1 Properties of the Brightness-Temperature Ratio

Eppler et al. (1992) collected microwave emissivities of several sea-ice types. A selection of sea-ice classes is shown for the near 19 GHz and 90 GHz microwave emissivities in Table 2.1. The emissivity ratio r_ϵ is defined as

$$r_\epsilon = \frac{\epsilon_{89V}}{\epsilon_{18.7V}} \tag{2.1}$$

Table 2.1: Vertically (V) polarized microwave emissivities of different sea-ice classes (Eppler et al., 1992) sorted according to their corresponding emissivity ratio from high to low values. The standard deviation is shown if available.

sea-ice class	90 GHz V	18.7 GHz V	ratio r_ϵ
water	0.792 ± 0.019	0.57 ± 0.033	1.389
new ice	0.85	0.623	1.364
dark nilas	0.885	0.76	1.164
pancake ice	0.893	0.811	1.101
gray nilas	0.915	0.837	1.093
light nilas	0.955	0.95	1.005
(summer melting)	0.953 ± 0.010	0.96 ± 0.020	0.993
first-year ice	0.926 ± 0.045	0.941 ± 0.019	0.984
flooded multi-year ice	0.902 ± 0.062	0.942 ± 0.036	0.958
frozen melt pond	0.876 ± 0.069	0.969 ± 0.030	0.904
dry multi-year ice	0.68 ± 0.105	0.85 ± 0.035	0.8
(summer-frozen surface)	0.728	0.96	0.758

with

$$\epsilon_{89V} - \text{emissivity at the vertically (V) polarized frequency of 89 GHz}$$
$$\epsilon_{18.7V} - \text{emissivity at the vertically (V) polarized frequency of 18.7 GHz.}$$

Röhrs et al. (2012) sorted the different sea-ice classes by their vertically polarized microwave emissivity ratio r_ϵ, starting with the highest values. Only water and thin ice classified into new ice, nilas, and pancake ice, show an emissivity above one while first-year and multi-year ice types show an emissivity below one (Table 2.1). Because we focus only on the winter season, the summer melting and summer-frozen surface crust ice is only of theoretical importance. In other words, the ratio between the emissivity of the vertically polarized frequency at 89 GHz ϵ_{89V} and at 18.7 GHz $\epsilon_{18.7V}$ allows one to differ entirely between thin ice and water on the one hand and thicker ice on the other hand.

The AMSR-E sensor measures the brightness temperature $T_{B,\nu}$ at a given frequency. The brightness temperature is defined as the product of the emissivity ϵ_ν at a given frequency and the effective emitting surface temperature T_S:

$$T_{B,\nu} = \epsilon_\nu T_S. \tag{2.2}$$

The effective emitting surface temperature T_S is defined as the integrated emitting layer thermometric temperature (Tonboe, 2010). The atmospheric attenuation of the brightness temperature measurements is neglected for two reasons: Firstly, the 19 GHz channel is less influenced by atmospheric attenuation than the 89 GHz channel. In the following section, we present the differing absorption coefficients at 19 GHz and 89 GHz and their link to the brightness temperature retrieval. Secondly, a spatial median filter is applied that weakens potential atmospheric influences (*cf.* section 2.2.2).

If we assume that the effective emitting surface temperature T_S at 19 GHz equals the effective emitting surface temperature T_S at 89 GHz, we can neglect the effective

emitting surface temperature at both frequencies. Assuming $T_{S18,V} \tilde{=} T_{S89,V} \tilde{=} T_S$, equations (2.1) and (2.2) yield:

$$r_\epsilon = \frac{\epsilon_{89V}}{\epsilon_{18.7V}} \tilde{=} \frac{T_{B,89V}}{T_S}\frac{T_S}{T_{B,19V}} = \frac{T_{B,89V}}{T_{B,19V}} = r. \tag{2.3}$$

The AMSR-E brightness temperature ratio r allows us to detect features like an area

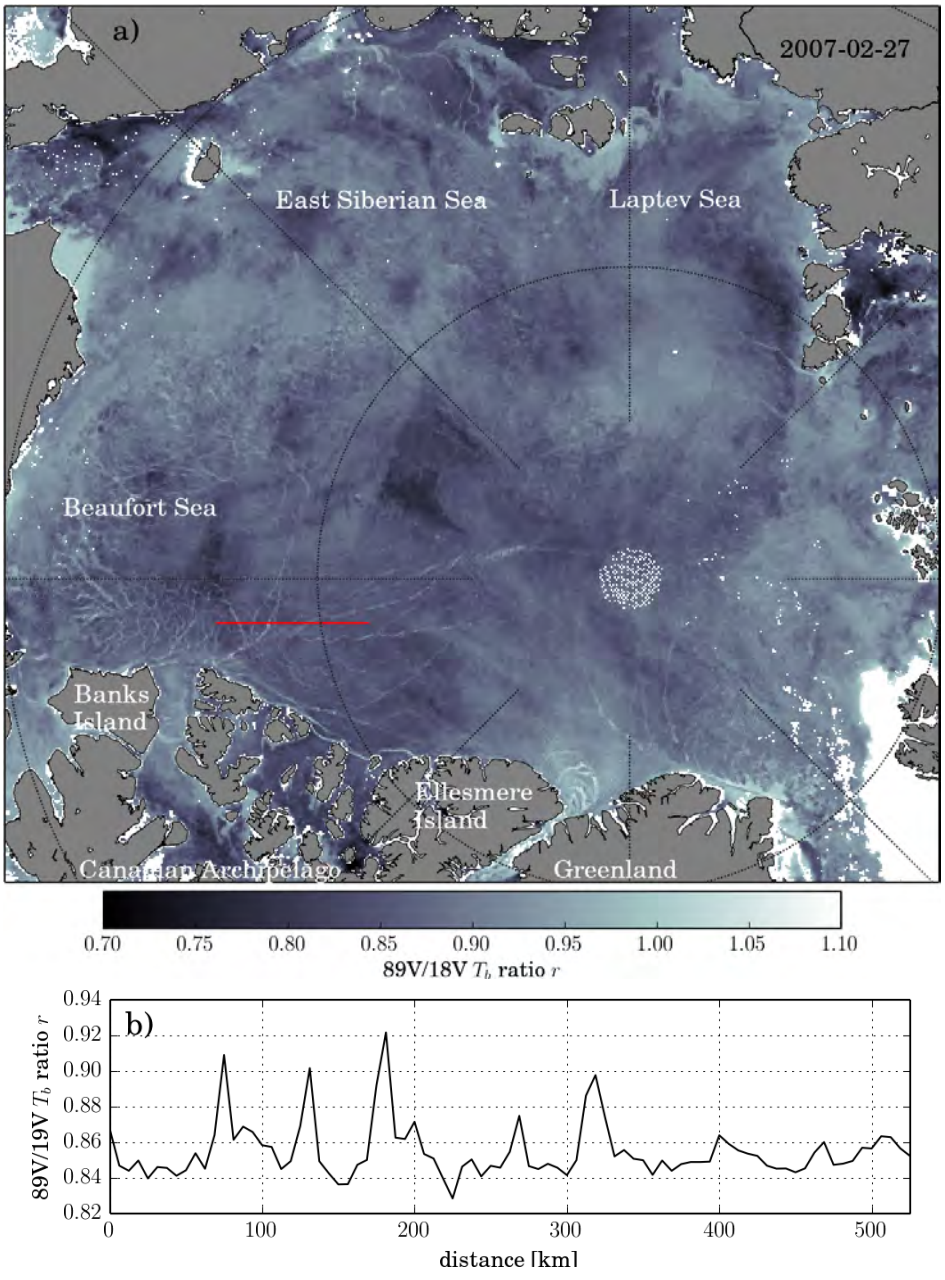

Figure 2.1: Brightness temperature ratio of the vertically polarized 89.0 GHz and 18.7 GHz channels on 27 February 2007 (**a**) and profile at the cross-section (red line) (**b**). Figure adapted from Röhrs et al. (2012).

of open water, a large lead, or a coastal polynya with $r > 1$ (Figure 2.1 a)). To sum up, the ratio enables us to differ between thin ice and thicker ice in the vicinity

Table 2.2: Specifications concerning the spatial resolution of the used AMSR-E channels. The National Snow and Ice Data Center (NSIDC) grid refers to polar stereographic map projection.

Channel	Sensor footprint	NSIDC grid
89.0 GHz	6 km×4 km	6.25 km
18.7 GHz	27 km×16 km	12.5 km

of leads. However, two effects are neglected but convey uncertainties: atmospheric attenuation of brightness temperature at a frequency of 89 GHz, as well as the effect of a vertical temperature gradient within the snow layer and ice layer on the brightness temperature. We describe these effects in section 2.2.3.

2.2.2 Median Filtering and Defining the Lead Concentration

In this section, we continue to introduce the lead detection algorithm by Röhrs et al. (2012). The spatial distribution of the brightness-temperature ratio r is depicted in Figure 2.1a). High r-values correspond to leads, as explained in section 2.2.1. Four leads are intersected by a cross-section (red line) in Figure 2.1a). The brightness temperature ratio at the cross-section is around 0.9 in the vicinity of leads (Figure 2.1b)), although from table 2.1 we would expect a value of $r > 1$ because leads consist of young thin ice and water. The AMSR-E sensor's footprint at 89 GHz and at 18.7 GHz (*cf.* Table 2.2) is often larger than the lead width. For the AMSR-E sensor, a lead signal appears as a mixture of a lead and surrounding thicker ice. Thus, the sensor cannot receive signals of the lead only. The resulting values of the brightness-temperature ratio r are lower than for the lead only. In order to adapt to lower values of the brightness temperature ratio r, Röhrs et al. (2012) assumed that leads are regions with high r values surrounded by regions with low r values. They separated r into a mean part $\overline{r}$ and an anomaly r':

$$r = \overline{r} + r'. \tag{2.4}$$

Röhrs et al. (2012) applied a spatial median filter to estimate r':

$$r' = r - \text{median}_w(r) \tag{2.5}$$

with

$$w - \text{window search size parameter [pixels]} \ (w \times w, w = 7 \mathrel{\tilde{=}} 44 \text{ km}).$$

The window search size parameter w defines the side length of a search window. The spatial median filter replaces the central pixel of the window with the median of the surrounding pixels. Röhrs et al. (2012) proved that the median filter detects leads more accurate than linear shift invariant filters. The spatial filtering does not only enhance the signal of leads, the surface signal is also filtered from the atmospheric signal due to different spatial scales.

In contrast to Röhrs et al. (2012), who named the resulting quantity *thin ice concentration*, we name the resulting quantity *lead concentration* (LC). Our motivation is that

the applied spatial filtering mostly highlights lead structures rather than larger areas of newly generated thin ice. The lead concentration (LC) is defined identically to what Röhrs et al. (2012) named thin ice concentration. An upper tie-point r'_{100} is estimated from the r' values, which sets the LC to 100 %, similarly a lower tie-point r'_0 sets the LC to 0 %. In between the two tie-points, the LC is linearly interpolated:

$$\mathrm{LC} = \begin{cases} 1 & \text{if } r' > r'_{100} \\ 0 & \text{if } r' < r'_0 \\ \frac{r'-r'_0}{r'_{100}-r'_0} & \text{if } r'_0 \leq r' \leq r'_{100}. \end{cases} \tag{2.6}$$

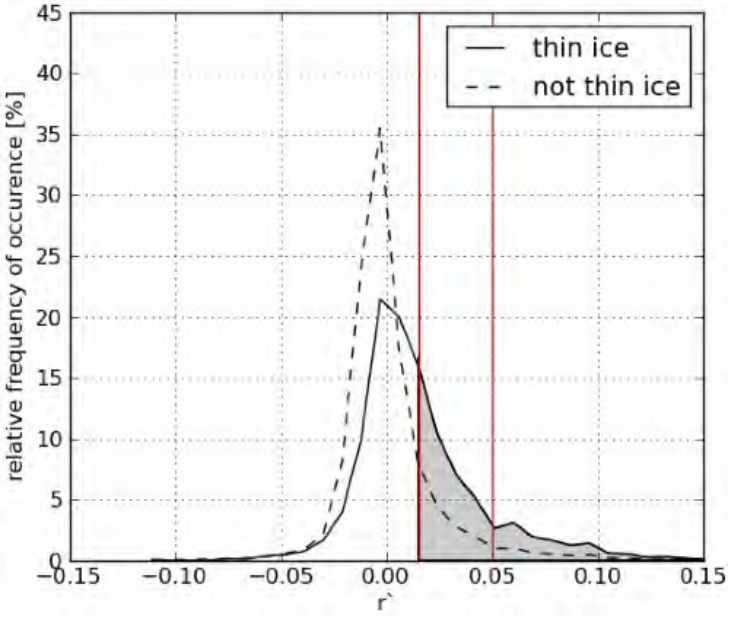

Figure 2.2: Frequency distribution of r' values for the profile on 27 February 2007. The red lines mark the lower and upper tiepoints of equation (2.6). The shaded area underneath the thin-ice curve marks lead pixels that are detected in the LC. Figure adapted from Röhrs et al. (2012).

Two classes of pixels are shown in a frequency distribution in Figure 2.2: not thin ice and thin ice and/or water. Röhrs et al. (2012) adjusted the LC tie-points from the profile shown in Figure 2.1b) via a comparison with Moderate-resolution Imaging Spectroradiometer (MODIS) band 3 images. The two classes are separated by a reflectance of 0.65. Almost no thick ice r' values appear for $r' > 0.05$, this fixes the upper tie-point. The lower tie-point is set to $r'_0 = 0.015$. The lower tie-point was confirmed by a validation with MODIS images (Röhrs et al., 2012). The validation showed that the lower tie-point allows one to detect leads narrower than the AMSR-E grid resolution. The smallest lead width that is still detectable equals 3 km. In order to focus on leads in the closed sea-ice cover, pixels with a sea-ice concentration value lower than 90% are not considered. We use Arctic Radiation and Turbulence Interaction STudy (ARTIST) Sea Ice (ASI) concentration that is also based on AMSR-E measurements.

2.2.3 Effects of Atmospheric Attenuation and Snow Cover on the Brightness-Temperature Retrieval

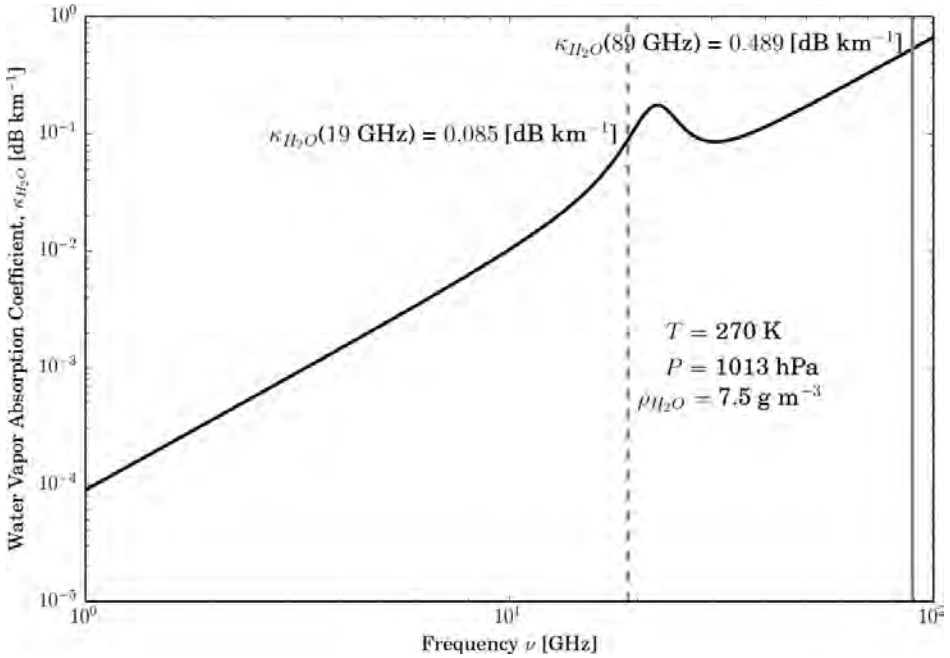

Figure 2.3: Attenuation coefficient of atmospheric water vapor κ_{H_2O} as function of frequency ν from 1 GHz to 100 GHz for Arctic sea-level conditions calculated using equation (2.7) taken from Ulaby et al. (1981), pp. 270. The grey dashed line marks the water vapor absorption coefficient at 19 GHz, the grey solid line at 89 GHz.

In this section, we describe the effects of atmospheric attenuation and a snow layer on the brightness temperature ratio r (equation (2.3)). We describe the atmospheric attenuation by reference to water vapor. Figure 2.3 shows the spectrum of the water vapor absorption coefficient κ_{H_2O} from 1 GHz to 100 GHz for Arctic sea-level conditions (T = 270 K, P = 1013 hPa, $\rho_{H_2O_{(\text{gaseous})}} = 7.5\ \frac{\text{g}}{\text{m}^3}$). We calculate the water vapor absorption coefficient κ_{H_2O} at frequencies below 100 GHz by the following equation given in Ulaby et al. (1981), p. 271:

$$\kappa_{H_2O}(\nu) = 2\nu^2 \rho_{H_2O_{(g)}} \left(\frac{300}{T}\right)^{\frac{3}{2}} \gamma_1 \left[\left(\frac{300}{T}\right) e^{\frac{-644}{T}} \frac{1}{(494.4-\nu^2)^2 + 4\nu^2\gamma_1^2} + 1.2 \cdot 10^{-6}\right] \tag{2.7}$$

where the linewidth parameter γ_1 is given by

$$\gamma_1 = 2.85 \left(\frac{P}{1013}\right) \left(\frac{300}{T}\right)^{0.626} \left[1 + 0.018 \frac{\rho_{H_2O_{(g)}} T}{P}\right]. \tag{2.8}$$

The water vapor absorption coefficient at 89 GHz is almost six times larger than the absorption at 19 GHz (indicated by grey lines in Figure 2.3). Other constituents of the atmosphere as oxygen or vertical distribution of cloud droplets also attenuate the emission at the 89 GHz and 19 GHz channels. The specific absorption coefficient κ is linked to the brightness temperature at a given frequency via $T_{B,\nu} \sim e^{-\tau_\nu}$ with the

optical thickness $\tau_\nu = \int \kappa_\nu(z)dz$ integrated over the height of the atmosphere (Ulaby et al. (1986), pp. 1347). In total, the surface emission at the 89 GHz channel is stronger attenuated than the surface emission at the 19 GHz channel.

Besides atmospheric attenuation, the physical properties that contribute most strongly to the Electro Magnetic (EM) signatures of sea ice and their uncertainties are the vertical profiles of temperature, salinity, and brine volume, together with the distribution of brine volume, brine pockets, and bubble sizes in the sea ice (Grenfell et al., 1998). We do not evaluate the uncertainties related to all parameters contributing to the EM signatures in a dedicated sensitivity study. Instead, we compare the resulting LC to independent lead observations from other sensors in section 2.3.3. However, we name a few uncertainties and introduce them briefly.

The effect of a varying snow cover imposes an uncertainty on emission signatures of sea ice at 19 GHz and 89 GHz. Perovich et al. (1998) concluded from measurements at a site near Point Barrow that the difference between the emissivity signature for bare sea ice and snow-covered sea ice is significant. Furthermore, first-year sea-ice microwave signatures change primarily due to snow cover related processes (Tonboe, 2010). Willmes et al. (2013) showed in a model study that the snow penetration depth and the emissivity at 19 GHz as well as at 89 GHz varies strongly with season. Processes at the synoptical scale can also alter the emissivity signature of snow covered sea ice. Grenfell et al. (1998) showed from measurements at a site near Point Barrow that after a warm air advection event the deepest and coldest layers of wet snow contribute to the brightness temperature only at lower frequencies, while the warmer upper layers contribute at higher frequencies. Neither are snow cover related processes considered in the algorithm by Röhrs et al. (2012), nor do we carry out an uncertainty analysis dealing with the effect of snow, mostly due to missing snow measurements with a sufficient spatial and temporal resolution. The snow cover variations add an uncertainty to the recent algorithm, which we cannot quantify.

Neglecting the effective emitting surface temperature (equation (2.3)) is a strong assumption, because of the differing emitting snow layer depths at 19 GHz and 89 GHz. Furthermore, during winter, when the atmosphere is usually colder than the ocean, the snow surface temperature is lower than the effective temperature at the penetration depth (Tonboe, 2010). Still, this is a very elegant solution, because we neglect the effective emitting surface temperature T_S, which is very difficult to measure. The ratio r reduces the effect of a varying effective emitting surface temperature relative to using only one brightness temperature channel, but the ratio can neither account for the variation of the vertical temperature gradient within the emitting snow layer, nor the implicit dependency of the emissivity on the effective emitting surface temperature $\epsilon_\nu = \epsilon_\nu(T_S)$.

2.3 Validation of the Lead-Detecting Algorithm

In this section, we compare examples of lead occurrences in the AMSR-E based LC maps from 2011 to different lead-detecting sensors. Figure 2.4 shows a LC map with a lot of lead patterns in the Arctic on 22 February 2011. The question is: How valid

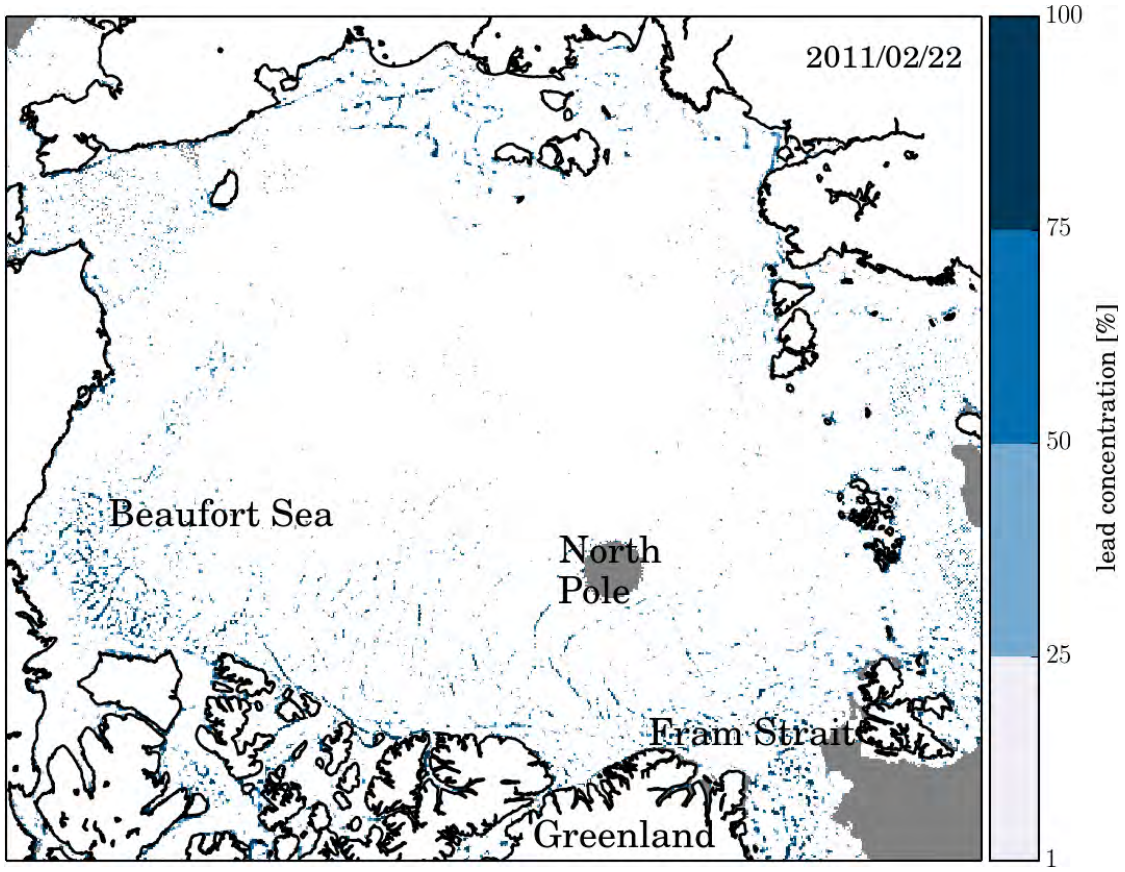

Figure 2.4: Distribution of leads in the Arctic Ocean on 22 February 2011. The blueish colors depict the LC [%]. Leads are characterized by a high LC as well as a linear and crack-like structure.

is such a LC map in comparison to observations obtained from other satellite sensors? We compare the LC maps to Advanced Synthetic Aperture Radar (ASAR) scenes and CryoSat-2 observations. Major differences between the three different sensors exist in terms of the applied measuring technique, the footprint, the spatial resolution and coverage, and the lifetime (*cf.* Table 2.3).

2.3.1 ASAR

The Advanced Synthetic Aperture Radar (ASAR) is mounted on the Environmental Satellite (Envisat) satellite. On 8 April 2012, the contact to Envisat was lost. ASAR operated in C-band at a frequency of 5.25 GHz with several measuring modes available. In this validation, we use only ASAR wide swath mode (WSM) scenes with a swath width of approximately 400 km. The ASAR technique imitates a large, stationary antenna by using the travel speed of Envisat ($\sim$ 7.5 km/s) while the radar antenna transmits radar pulses (McCandless and Jackson, 2004). ASAR WSM images depict normalized radar backscatter coefficients which are processed to a 150 m resolution. In an ASAR scene, leads are visible as linear structures in the sea-ice cover with lower normalized radar backscatter coefficients than the surrounding sea ice. Neither does

Table 2.3: Comparison of AMSR-E, ASAR, and CryoSat-2. The sensor footprint refers for AMSR-E to the 89 GHz brightness-temperature channel, for ASAR to WSM mode (ESA, 2004), and CryoSat-2 to SAR mode tracks (Wingham et al., 2006). We do not interpolate the CryoSat-2 measurements in a grid.

	AMSR-E	ASAR	CryoSat-2
Sensor type	passive microwave	active radar	active radar
Sensor footprint	6 km × 4 km	∼ 150 m × 150 m	∼ 300 m × 1500 m
Resolution (grid size)	6.25 km × 6.25 km	150 m × 150 m	-
Spatial coverage	entire Arctic	partial coverage	daily tracks
Lifetime	2002 - 2011	2002 - 2012	2011 - until now

ASAR as an active measuring sensor depend on daylight nor is the backscattered radar signal severely distorted by clouds. MODIS observations are left out of this validation, because they have been used to calibrate the LC algorithm. In the following section, we shortly introduce the lead detection based on CryoSat-2 measurements.

2.3.2 Lead Detection from CryoSat-2

The lead detection is based on a threshold assumption applied to CryoSat-2 SAR mode level-1b data. CryoSat-2 carries the Synthetic Aperature Interferometric Radar Altimeter (SIRAL). In SAR mode, the SIRAL instrument operates with a pulse-repetition frequency of 18.182 kHz (every 55 μs) for transmitting a group of 64 pulses (Wingham et al., 2006). The SAR measurements are processed to a normalized waveform (intensity wave function) at each location of the CryoSat-2 track consisting of 128 samples. The maximum value as well as the shape of the normalized waveform depend on the roughness of the underlying surface (Zygmuntowska et al., 2013; Kurtz et al., 2014).

If the surface roughness is high, the maximum value of the normalized waveform is rather small. A rough surface can be associated with older multi-year sea ice. A flat and specular surface corresponds to water or new thin ice (Onstott and Suchman, 2004). The maximum value of the normalized waveform is several orders of magnitude higher for a specular surface than for a rough surface (Sandven et al., 2001). Because a lead consists of open water or young thin ice, the corresponding high maximum value of the normalized waveform for a specular surface is used to isolate lead positions in the sea-ice cover.

Not only does the maximum value for a signal received above a rough surface differ from a signal received above a flat and specular surface, but also do the shapes of the normalized waveform differ. Here, we focus only on the maximum value of the normalized waveform. The normalized waveforms range from 0 to 65535 and correspond to a normalized power (Figure 2.5a). The normalized waveforms can be converted to power values after Mantoviani et al. (2009) via

$$P = N \times (A \times 10^{-9}) \times 2^{B} \tag{2.9}$$

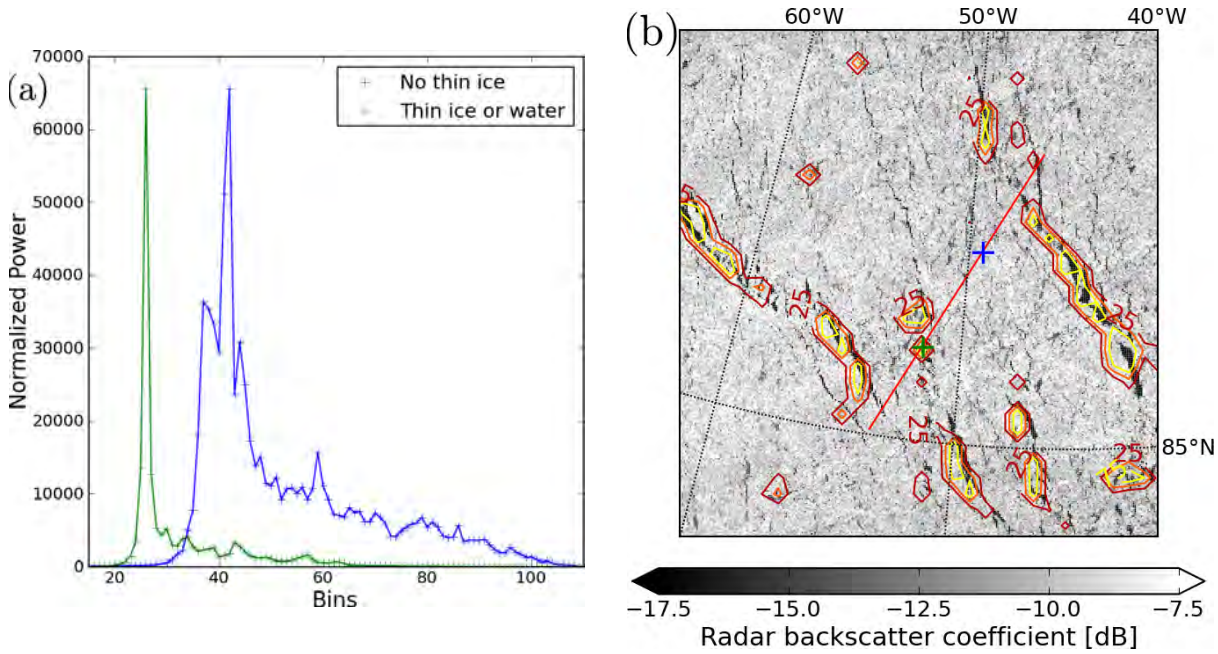

Figure 2.5: Normalized waveforms (**a**) depict the CryoSat-2 measurements at the green and blue cross in (**b**). The multi-sensor comparison (**b**) consists of an ASAR scene depicted as normalized radar backscatter coefficient [dB], AMSR-E LC [%], and a CryoSat-2 track (red line) north of Greenland on 22 February 2011. The 25%, 50%, and 75% LC contour lines are depicted in dark red, orange, and yellow.

with

P – power [W]
N – number of waveform counts
A – echo scale factor
B – echo scale power.

The values of the scale parameters A and B depend on the individual waveform. Siligam (2012) found a threshold power value of $P = 10^{-9}$ W, which separates leads and thin ice (white dots) from older sea ice (black line) in Figure 2.7.

In order to illustrate the threshold criterion and to look at the lead resolving spatial scale, we zoom in a region north of Greenland north of 85° N and between 60° W to 40° W on 22 February 2011 (Figure 2.5b). Figure 2.5 shows a multi-sensor comparison of an ASAR scene depicted as normalized radar backscatter coefficient, LC depicted as contour lines, and a part of a CryoSat-2 track depicted as a red line. Larger leads visible in the ASAR scene are collocated with lead structures visible in the LC. A green cross on the CryoSat-2 track marks a location with a high LC value and a low radar backscatter coefficient indicating a lead. The corresponding normed waveform measured by CryoSat-2 shows a distinguished peak. This indicates a specular surface which is typical for new thin ice or frozen water originating from a recently formed lead. In contrast, the normed waveform at the location of the blue cross on the CryoSat-2 track does not show a distinguished peak. The blue waveform is much broader

distributed than the green waveform. These characteristics imply a underlying rough surface, typical for older sea ice, which has already been shaped by the environment.

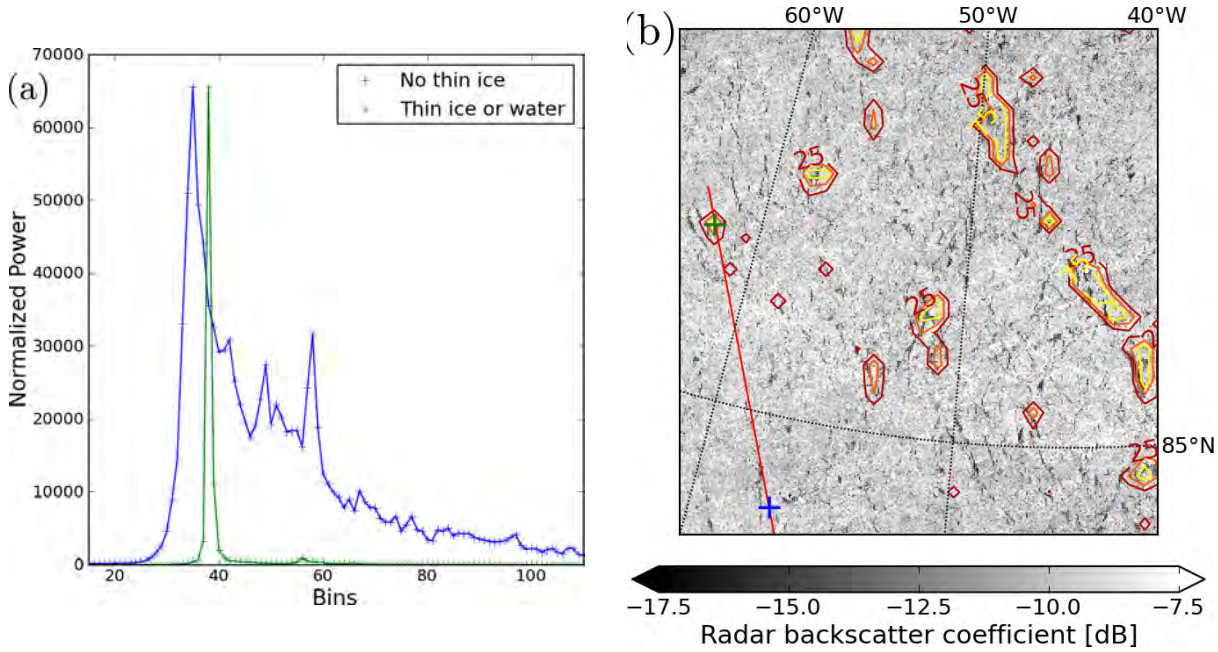

Figure 2.6: Normalized waveforms (**a**) depict the CryoSat-2 measurements at the green and blue cross in (**b**). The multi-sensor comparison (**b**) consists of an ASAR scene depicted as normalized radar backscatter coefficient [dB], AMSR-E LC [%], and a CryoSat-2 track (red line) north of Greenland on 25 February 2011. The 25%, 50%, and 75% LC contour lines are depicted in dark red, orange, and yellow.

Figure 2.6 shows the same region north of Greenland as in Figure 2.5 three days later. Again, we observe an accurate alignment between the closing lead in the AMSR-E LC and the underlying ASAR scene between 50° W to 40° W in Figure 2.6. The different shapes of the two normed waveforms show the difference between the high LC at the green cross and a randomly selected 0% LC-value at the blue cross on the CryoSat-2 track.

2.3.3 Multi-Sensor Case Study

Due to a temporal overlap of all three sensors in 2011 (*cf.* Table 2.3) and a sufficient coverage of ASAR scenes, we zoom into a region north of Greenland in order to access more details. In this section, we evaluate the accuracy of the LC not the quality of ASAR scenes or the threshold criteria applied on CryoSat-2 measurements. In order to evaluate the latter, one would need to zoom in a smaller region in order to receive a higher image resolution.

Figure 2.7 shows the AMSR-E LC depicted as two contoured lines (25 % in red and 75 % in yellow) north of Greenland on 22 February 2011. The underlying filled contour field depicts normalized radar backscatter values from a composite of ASAR scenes. Low backscatter values are associated with leads and younger ice. The crack-like and

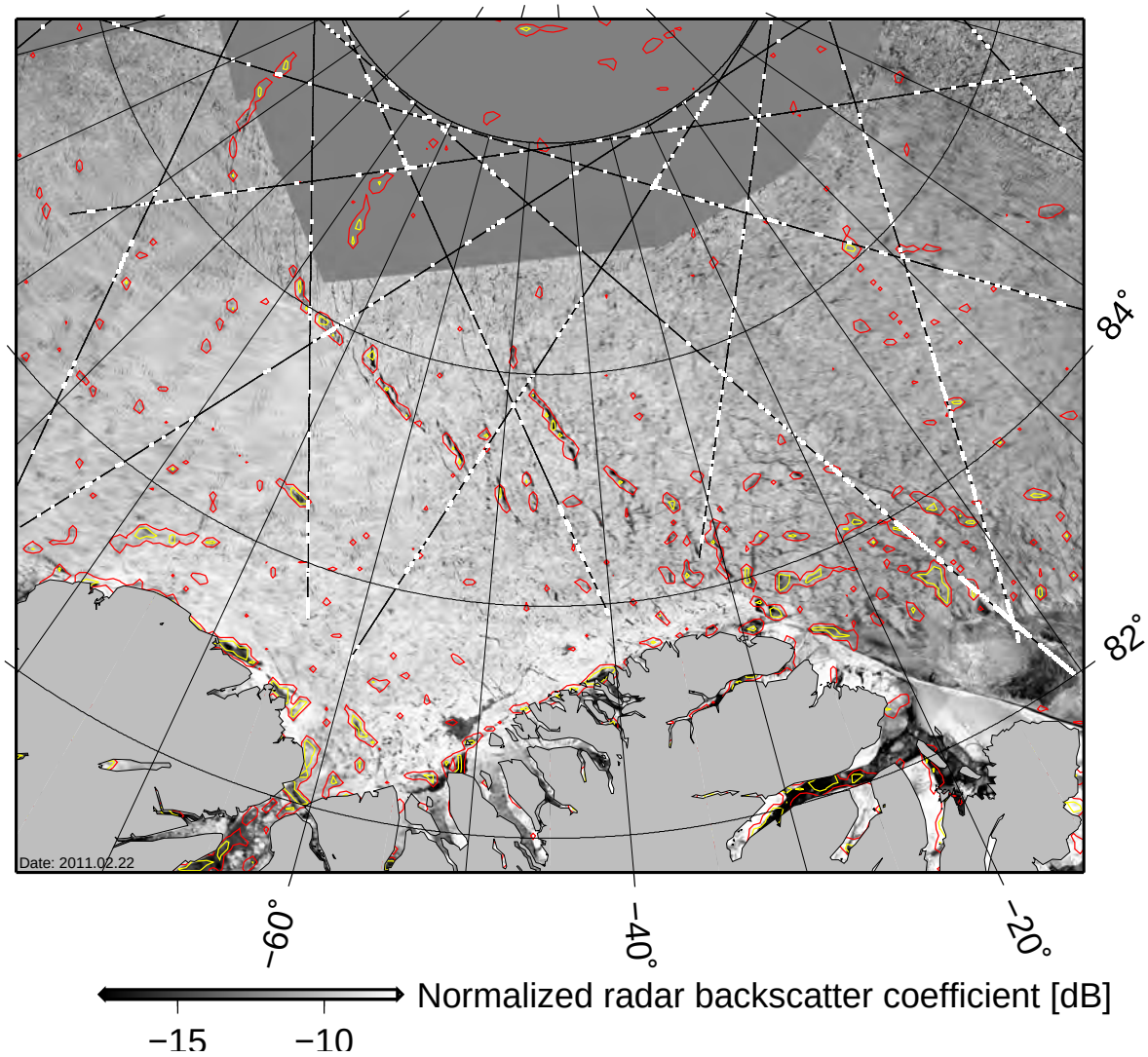

Figure 2.7: Multi-sensor comparison: Composite of ASAR scenes depicted as normalized radar backscatter coefficient [dB], AMSR-E LC [%] (red isoline - 25 %, yellow isoline - 75 %), and lead positions from CryoSat-2 (white dots on top of the black CryoSat-2 track) north of Greenland on 22 February 2011.

linear structure of the darker contours in the ASAR scene support that these patterns can often be considered as leads. We observe a rise in AMSR-E LC where we see large leads in the ASAR scenes. Additionally, we derive lead locations from CryoSat-2. We observe no mismatch between high LC values and leads depicted as white dots on the black CryoSat-2 tracks in Figure 2.7. CryoSat-2 detects a lot more leads on a track compared to leads visible in the LC, probably because of the smaller sensor footprint of CryoSat-2 compared to AMSR-E (*cf.* Table 2.3). More examples depicting the general agreement between the AMSR-E LC in comparison to ASAR scenes and lead detections by CryoSat-2 are shown in the Appendix (Figure A.1 and A.2).

As in Figure 2.7, Figure 2.8 shows the AMSR-E LC north of Greenland but on 17 April 2011. This example shows a lead (marked by a red box) with a long lifetime located northwest of Greenland (84°N, 20°W). The lead opened on 6 April 2011 (Figure A.3

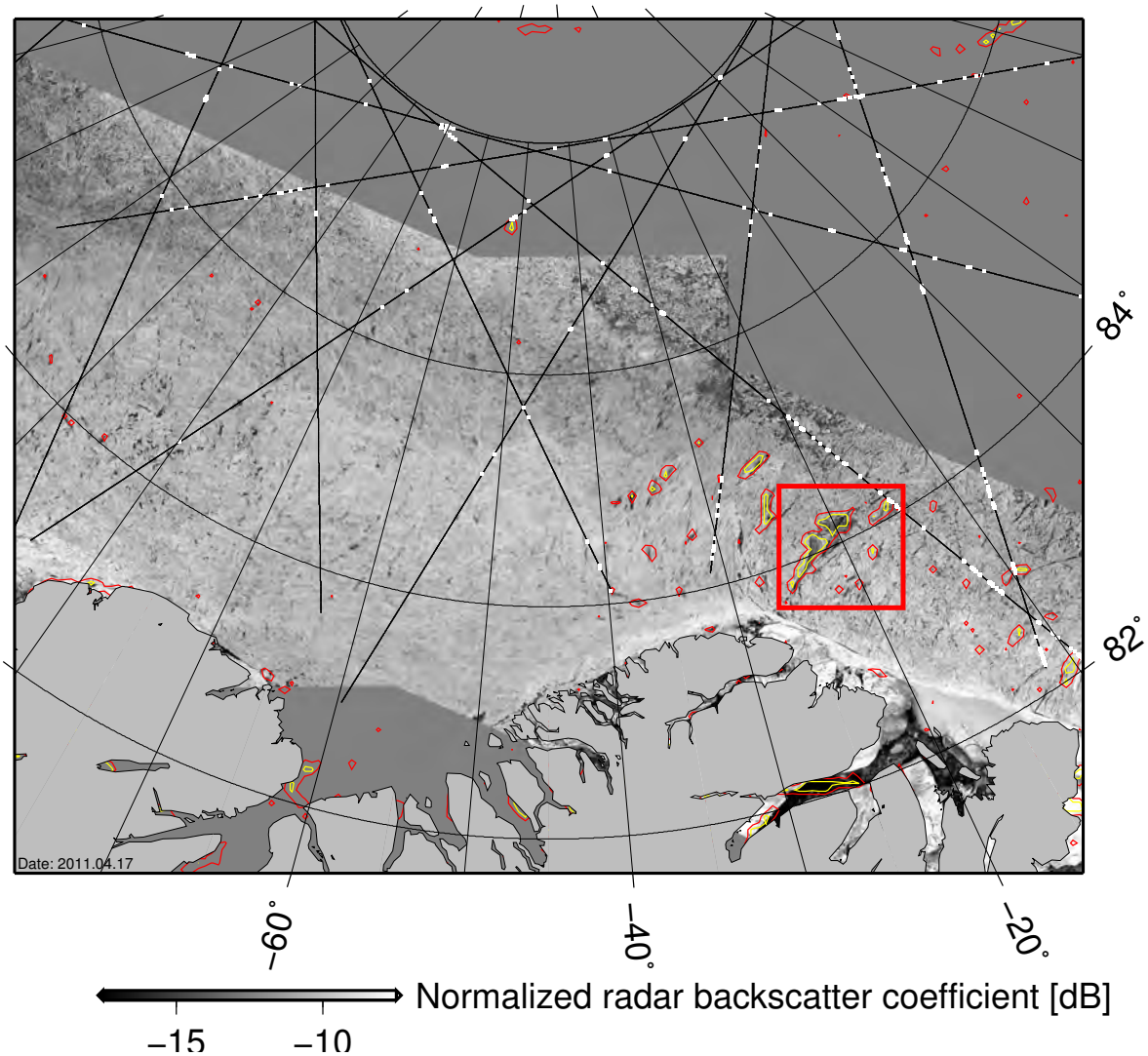

Figure 2.8: Multi-sensor comparison: Composite of ASAR scenes depicted as normalized radar backscatter coefficient [dB], AMSR-E LC [%] (red isoline - 25 %, yellow isoline - 75 %), and leads positions from CryoSat-2 (white dots on top of the black CryoSat-2 track) north of Greenland on 17 April 2011. The red box marks the position of a lead with a long lifetime.

in Appendix) and remained until the end of April 2011 (Figure A.4 in Appendix). The long lifetime of the lead is also confirmed by reoccurring of the lead in ASAR scenes.

2.4 Discussion and Summary

In this chapter, we apply the algorithm introduced by Röhrs et al. (2012), which uses the near 19 GHz and 89 GHz brightness-temperature channels instead of only the 89 GHz brightness-temperature channel. The disadvantage of the single channel algorithm is that the algorithm requires measurements of the effective emitting surface temperature, which are very difficult to obtain. Atmospheric attenuation and snow cover related processes certainly influence the quality of the algorithm. Both pro-

cesses are not explicitly dealt with in an uncertainty analysis, however the influence of atmospheric attenuation is weakened by using the brightness-temperature ratio.

We introduce a method to detect leads from CryoSat-2 measurements. The applied criterion is a threshold power value $P = 10^{-9}$ W (Siligam, 2012). The detected lead positions in the LC maps agree with lead positions observed in ASAR scenes and detected by CryoSat-2. The lifetimes of large leads observed in the LC are comparable to the lifetimes of large leads observed in ASAR scenes. The LC detects only large leads of at least 3 km in width. The ASAR and CryoSat-2 measurements indicate that a lot more small-scale leads exist than resolved in the LC. However, everywhere where the LC resolves a lead, the existence of this lead is confirmed by CryoSat-2 and ASAR measurements.

Chapter 3

Introducing and Evaluating a Method to Automatically Detect the Lead Orientation[1]

3.1 Introduction

The starting point for this chapter are evaluated Arctic-wide maps of lead concentration with a grid resolution of 6.25 km. The lead concentration algorithm provides no directional information. Thus, we need to detect line structures within the lead concentration maps from which an orientation can be inferred. Furthermore, we aim to introduce a fully automatic method to derive lead orientations for the first time.

Miles and Barry (1998) detect leads in images of the western Arctic for winters from 1979 to 1985 recorded by the operational line scanning (OLS) sensor on the Defense Meteorological Satellite Program (DMSP). They manually inferred the lead orientation by drawing a line through a lead visible in OLS images. The manual approach is still the best option to detect reference leads for an evaluation of automatically detected leads. To be less susceptible to human perception and to reduce the manual workload, we here use an automatic approach for inferring the lead orientation based on the Hough transform.

This Hough transform is an image analysis technique to detect line structures like leads in images. Fetterer and Holyer (1989) were the first to apply the Hough transform in a semi-automatic approach to detect leads from Advanced Very High Resolution Radiometer (AVHRR) satellite images. Lindsay and Rothrock (1995) list some alternative approaches to the Hough transform: the local gradient in an image (Sobel operator), 2D-Fourier transform, skeleton orientations (Bandfield, 1992), and the direction of maximum extent. Lindsay and Rothrock (1995) performed a semi-automatic detection of lead orientations from AVHRR images for the year 1989. Their method recognizes also small scale leads, but covers only small parts

[1]This chapter has been published in: Bröhan, D., Kaleschke, L. (2014). A Nine-Year Climatology of Arctic Sea Ice Lead Orientation and Frequency from AMSR-E. Remote Sens., 6(2):1451-1475.

of the Arctic. Lindsay and Rothrock (1995) rejected the Hough transform, because the Hough transform was at that time subject to rather arbitrary choices. While Lindsay and Rothrock (1995) decided to develop a semi-automatic method based on the maximum extent of a lead, we apply a more recent and a more advanced version of the Hough transform, the progressive probabilistic Hough transform by Galambos et al. (2002). This version of the Hough transform provides additional input parameters in comparison to the classical Hough transform. Furthermore, the progressive probabilistic Hough transform analyzes only a subset of image pixels which reduces the calculation time. There have been no published attempts after Fetterer and Holyer (1989) to infer lead orientations in an automatic manner using the Hough transform.

We start with a short description of the Advanced Microwave Scanning Radiometer for Earth Observing System (AMSR-E) satellite sensor in section 3.2. In section 3.3, we introduce the Hough transform and an algorithm that clusters multiple detected leads belonging to an identical lead position. We evaluate the automatically detected leads with manually detected leads and compare them to Advanced Synthetic Aperture Radar (ASAR) scenes in section 3.4. We discuss uncertainty and limitations of the developed approach to derive the lead orientation in section 3.5.

3.2 Data

We estimate the lead concentration from AMSR-E passive microwave data following an approach developed by Röhrs et al. (2012). Japan Aerospace Exploration Agency (JAXA) AMSR-E sensor is mounted on the National Aeronautics and Space Administration (NASA) Earth Observing System (EOS) Aqua satellite. The satellite was launched in 2002 and provided measurements until 2011. AMSR-E measures at six different frequencies ranging from approximately 19 GHz to 89 GHz. We use the level-3 gridded product of the 19 GHz (Cavalieri et al., 2003) and 89 GHz (Cavalieri et al., 2004) vertically polarized brightness temperature channels with a pixel resolution of 6.25 km times 6.25 km. Like Röhrs et al. (2012), we focus on leads in the closed sea-ice cover. Thus, pixels are not considered that contain more than 10% of open water according to Arctic Radiation and Turbulence Interaction STudy (ARTIST) Sea Ice (ASI) concentration (Kaleschke et al., 2001; Spreen et al., 2008).

We use Advanced Synthetic Aperture Radar (ASAR) wide swath mode (WSM) images to validate our automatically detected lead orientations with independent measurements. ASAR provides C-band measurements at a frequency of 5.25 GHz as normalized radar backscatter coefficients, which depict partly the surface roughness. ASAR WSM images are processed to a 150 m resolution. The swath width is approximately 400 km. The ASAR sensor is mounted on European Space Agency (ESA)'s satellite Environmental Satellite (Envisat). ESA provides ASAR observations until April 2012 when contact to Envisat was lost.

3.3 Methods

In this section, we briefly present the algorithm by Röhrs et al. (2012) to infer the lead concentration (section 3.3.1). The core of the new algorithm is the Hough transform (section 3.3.2) together with a cluster algorithm (section 3.3.3). In section 3.3.4, we introduce the C-score to evaluate a detected lead with the underlying lead concentration. We connect the individual pieces in an outline of the entire algorithm in section 3.3.5.

3.3.1 Lead Concentration

When sea water freezes in winter, nilas is formed as the first consolidated type of thin ice. Röhrs et al. (2012) found that nilas shows a unique signature in the emissivity ratio between the 19 GHz and 89 GHz vertically polarized brightness temperature channels. We estimate the lead concentration by calculating the emissivity ratio between the two AMSR-E brightness temperature channels. In order to highlight lead structures, Röhrs et al. (2012) applied a spatial median filter on the brightness temperature ratio r. We apply the same tie points of the brightness-temperature ratio ($r_{0\%} = 0.015$ and $r_{100\%} = 0.05$) as Röhrs et al. (2012) to estimate the lead concentration (Integrated Climate Data Center (ICDC), 2013). The algorithm detects leads having a width of at least 3 km in the sea-ice cover although the grid resolution of the lead concentration covers 6.25 km $\times$ 6.25 km.

AMSR-E resolves the radiometric signal of a lead fraction approximately greater than 50% in a grid cell. Leads smaller than 3 km in width are sometimes depicted as fragments visible as pixels showing no distinct structure. In order to reduce the number of fragments, we remove single pixels in the binary lead concentration maps with a morphological hit-or-miss transform. The binary lead concentration consists of two classes: 0 for 0% lead concentration and 1 for 1% to 100% lead concentration. From a lead concentration map one can manually determine the lead orientation by drawing a line through a lead structure and estimating the orientation of this line. We apply this manual approach in order to obtain reference leads for a comparison with automatically detected leads. The automatic detection of lead orientations is explained in the following sections.

3.3.2 Hough Transform

The principle of the Hough transform is shown in Figure 3.1. Paul V.C. Hough originally invented the Hough transform in 1962 to recognize complex lines in photographs or other pictorial representations (Hough, 1962). Duda and Hart (1972) applied the Hough transform to picture analysis. With the Hough transform we seek to answer the question: Which line connects points that are stringed together? Due to unresolved lead fragments the lead concentration shows a lot of none line-like patterns. The purpose of the Hough transform is to discern lead structures with a line shape from other geometrical fragments.

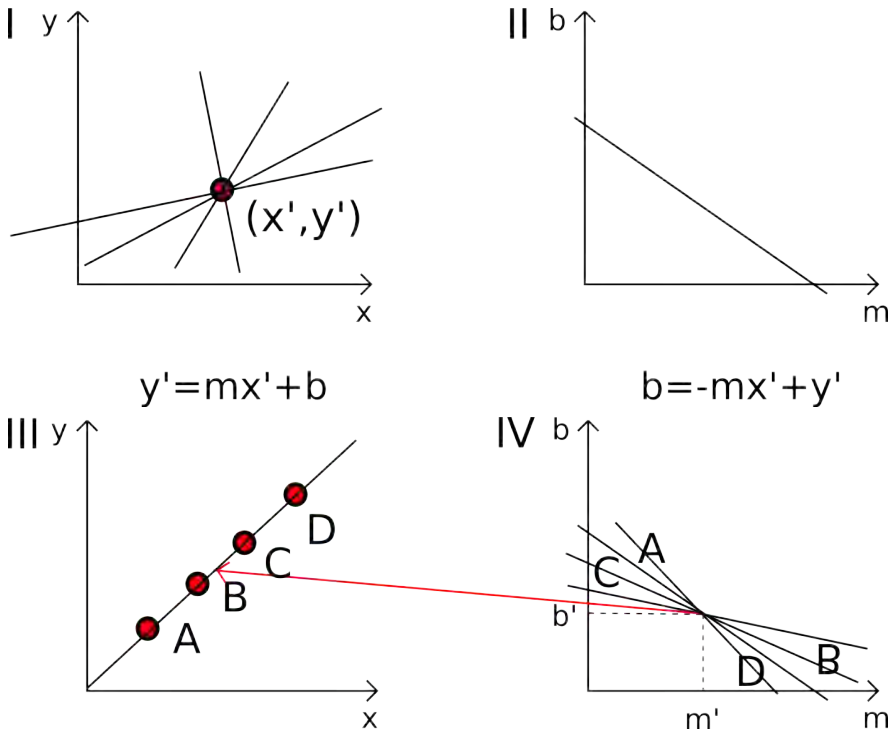

Figure 3.1: Principle of the Hough transform: An arbitrary point (x', y') in a coordinate system is intersected by lines with arbitrary slopes m and y-offsets b (**a**). All lines are described by one parameter line (**b**). The parameter lines (**c**) belong to a chain of corresponding points (**d**). The points are connected via a line with the slope m' and the y-intersect b' indicated by a red arrow.

Figure 3.1a shows a point in a coordinate system. The point is intersected by lines with all possibles slopes m and y-intersects b:

$$y' = mx' + b. \tag{3.1}$$

Equation (3.1) can be rewritten to

$$b = -mx' + y' \tag{3.2}$$

representing all lines in the normal space that intersect in the point (x', y') as one parameter line in the parameter (m, b) space (Figure 3.1b). Figure 3.1d shows a chain of unconnected points. The corresponding parameter lines are shown in Figure 3.1c. In our example, four entries accumulate where the parameter lines intersect. Therefore, the space is named accumulator space. We determine the line that connects the points A, B, C, and D in Figure 3.1d with the slope m' and the y-intersect b' at the intersection of the four parameter lines inserted in equation (3.1).

Because if the slope m reaches zero the linear formulation will fail, the normal parametrization of a line is often chosen for the Hough transform:

$$l = x\cos(\theta) + y\sin(\theta) \tag{3.3}$$

$$l - \text{normal line distance from the origin}$$
$$\theta - \text{angle between distance and the x-axis}$$
$$x, y - \text{x,y - plane coordinates.}$$

We use an alternative implementation of the Hough transform, the progressive probabilistic Hough transform by Galambos et al. (2002). The major difference to the classical Hough transform is that the progressive probabilistic Hough transform uses only a randomly selected sample of image pixels. The progressive probabilistic Hough transform offers three input parameters:

1. Threshold value—pixels with a lower number of occurrences in the accumulator space are not considered as a lead. For every randomly selected point, the progressive probabilistic Hough transform tests the hypothesis if the number of occurrences in the accumulator space could be due to random noise. The classical Hough transform also uses a threshold value as input, but the classical Hough transform calculates the number of occurrences for every pixel and not only for a sample of pixels.

2. Minimum line length—leads shorter than this length are neglected. A minimal line length reduces the computing time significantly (Galambos et al., 2002).

3. Maximum line gap—distance (in pixels) the progressive probabilistic Hough transform is allowed to fit when a lead is interrupted.

A major advantage of the progressive probabilistic Hough transform over the classical Hough transform is that the progressive probabilistic Hough transform detects finite lines. A detailed algorithm outline of the progressive probabilistic Hough transform can be found in Galambos et al. (2002). We refer to the term probabilistic progressive Hough transform henceforth with the term Hough transform.

3.3.3 Cluster Algorithm

Because the Hough transform often detects identical lead positions several times we cluster lead detections that are located around only one lead position in a lead concentration map (Figure 3.3). The criterion is the maximal euclidean distance d a cluster is allowed to have to a neighboring cluster. In order to illustrate the functionality of the cluster algorithm, we create an idealized test data set consisting of six leads (Figure 3.2a).

The cluster algorithm uses a proximity matrix (Figure 3.2b) to evaluate the criterion of for example $d = 2$ pixels. The matrix elements consist of distances between the lead centers. Only distances smaller than $d = 2$ pixels are shown. Distances smaller than $d = 2$ pixels indicate that two leads belong to the same cluster. By looking at the rows and columns of the matrix, we see that lead center 3 misses a lead center within the distance $d = 2$. Lead centers 4 and 5 build a cluster. The remaining lead centers 1, 2, and 6 build the last cluster. Lead centers 2 and 6 are clustered indirectly via the remaining lead center 1. We apply the developed cluster algorithm with a maximal

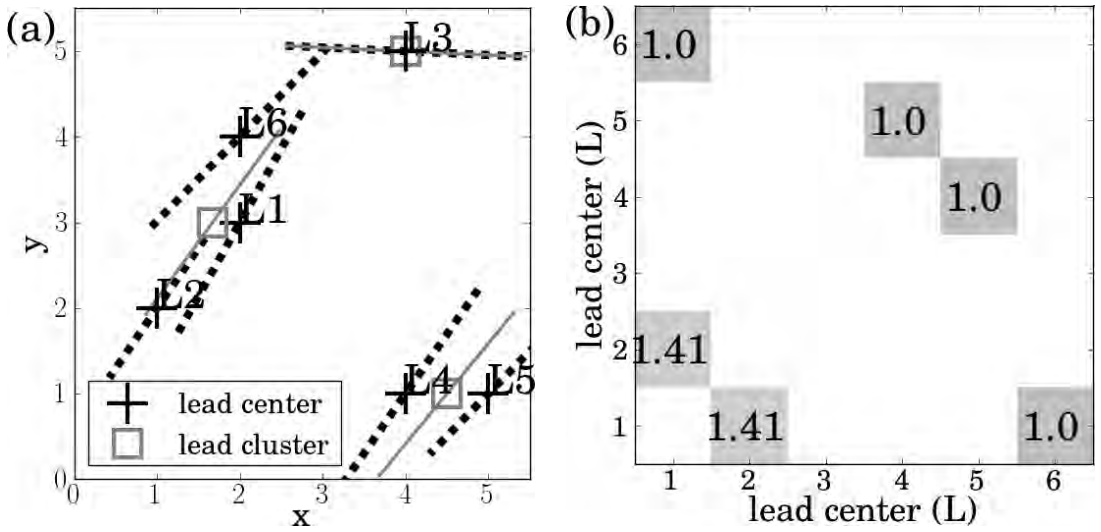

Figure 3.2: Principle of the cluster algorithm: Leads (black dotted lines) are reduced to lead centers (black cross, abbreviated to L) in a test data set (**a**). The numbers in the proximity matrix (**b**) represent the distance between the lead centers. All distances greater than the maximal distance d = 2 are whitened. Intersecting rows and columns with an entry identify lead clusters belonging to one cluster. The clustered lead centers are depicted as gray squares and the clustered leads as gray lines (a).

distance $d = 4$ pixels to the leads detected by the Hough transform. The cluster algorithm greatly reduces the number of leads like for an example north of Greenland on 14 March 2011 (Figure 3.3). In this example, the cluster algorithm reduces ten leads to four clustered leads.

We tested maximal distances ranging from $d = 2$ to $d = 7$ in varying sub-regions of the Arctic on different days. We conclude that if we increase the maximal distance the total number of leads will further decrease, but we run a higher risk to cluster leads that do not belong to the same lead. With the subjective choice of a rather small maximal distance $d = 4$ pixels, we accept that some leads are still detected several times (Figure 3.3). Otherwise, no lead was misplaced by the clustering in the evaluated examples with a maximal distance $d = 4$ pixels.

3.3.4 C-Score

In order to check if for example a lead is misplaced by the clustering, we evaluate the lead via the consistency (C) or C-score:

$$\mathrm{C} = \frac{\text{lead concentration pixels}}{\text{Hough pixels}} \tag{3.4}$$

The C-score checks if pixels covered with a lead detected by the Hough transform is underlaid by lead concentration pixels. The more pixels of a lead detected by the Hough transform are covered with pixels of lead concentration, the closer the C-score gets to 1.

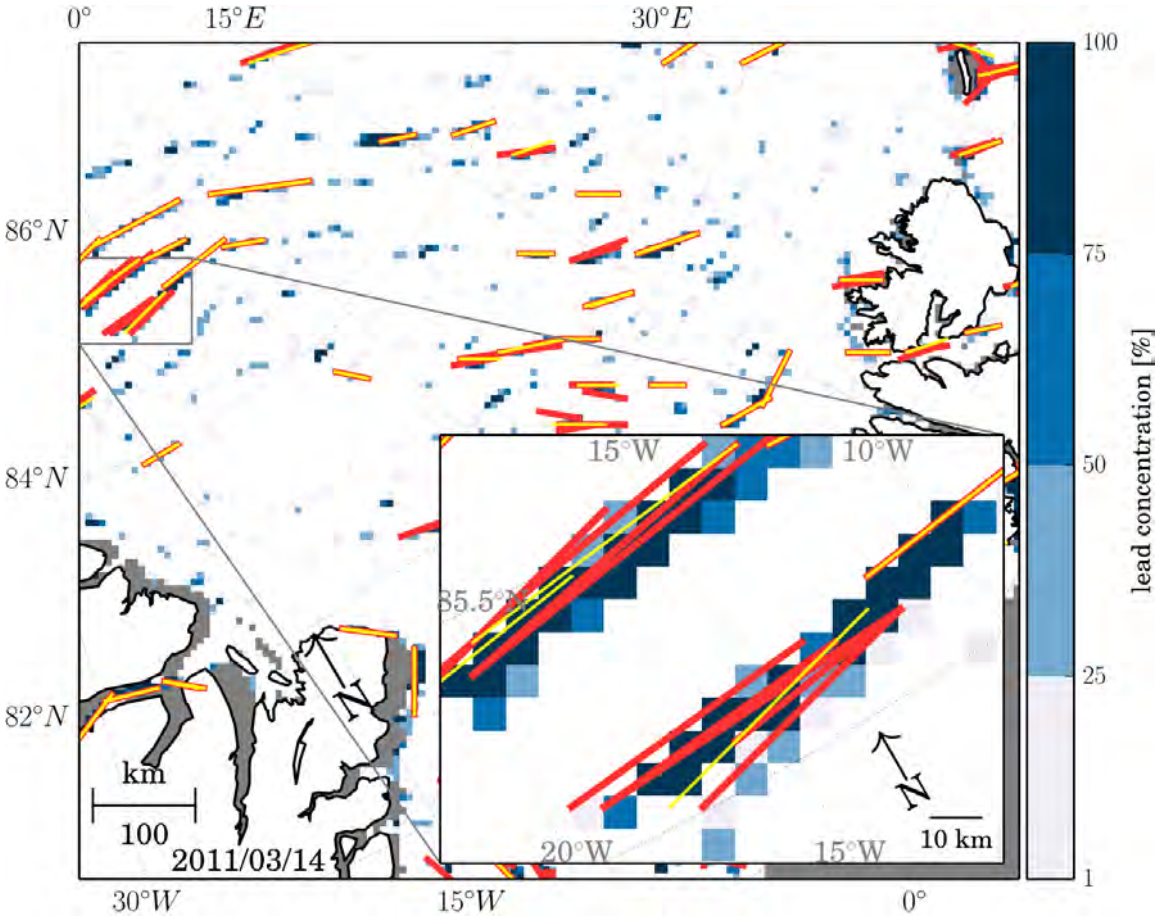

Figure 3.3: Comparison between unclustered leads (red lines) and clustered leads (yellow lines) in the Fram Strait and a regional zoom north of Greenland on 14 March 2011. The lead concentration is depicted in blueish colors. The cluster distance d equals 4 pixels or 25 km.

3.3.5 Algorithm Outline

In the end of this section, we bring all components comprising the algorithm to infer the lead orientation together in an outline of the algorithm. The Hough transform needs a threshold value and a minimal line length as input parameters in order to detect leads. We keep the maximum line gap (section 3.3.2) fixed to one pixel. We test several threshold parameter and minimal line length combinations and conclude that one combination that is most accurate for every day does not exist.

Because one combination of input parameters does not exist, we use a set of varying input parameter combinations for every day. We evaluate the quality of an input parameter combination for the Hough transform via the daily mean C-score (section 3.3.4). We test all possible Hough transform input combinations for threshold values between 5 and 50 and minimal line lengths between 5 and 15 pixels. We select 50 Hough input parameter combinations out of 506 options that are closest to $C = 1$ for a test period covering the whole Arctic and lasting from February to April 2011 (*cf.* Table A.1 in the Appendix).

Figure 3.4 summarizes the steps of the complete algorithm. First, we apply an algo-

rithm by Röhrs et al. (2012) to obtain the lead concentration. Afterwards, we remove single pixels in the binary lead concentration maps with a morphological hit-or-miss transform. This step reduces the fragments in the image caused by unresolved small-scale leads. The Hough transform by Galambos et al. (2002) is applied on the preprocessed binary image. We apply the most accurate 50 parameter combinations to every day of the AMSR-E time series and select the three most accurate parameter combinations via the C-score (equation (3.4)). We select all leads with an individual C-score $C \geq 0.85$ detected by the Hough transform from the three most accurate parameter combinations. The resulting leads are clustered if the lead centers are closer than 4 pixels to one another. On these clustered leads, we apply the consistency criterion with $C \geq 0.5$ once again in order to remove leads that got heavily misplaced during the clustering. As the final step, we calculate the lead orientation as angle from the leads.

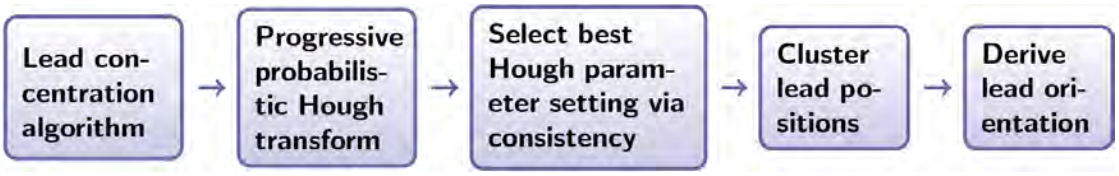

Figure 3.4: Sketch of the algorithm outline.

3.4 Evaluation

In this section, we evaluate leads detected by the Hough transform by using leads manually detected from a lead concentration map. Because we detect leads from daily lead concentration maps, we evaluate leads on the daily time-scale. The focus is in detail on the Fram Strait region on 14 March 2011 and the Beaufort Sea on 14 November 2004. We choose the Fram Strait and the Beaufort Sea, because lead patterns occur that are representative of the Arctic. Additionally, leads detected by the Hough transform are validated with leads visible in ASAR scenes.

3.4.1 Evaluation of Leads Detected by the Hough Transform with Manually Detected Leads

In order to compare manually detected reference leads with automatically detected leads, we zoom in the Fram Strait region on 14 March 2011 for a case study (Figure 3.5). We analyze a similar map that is not shown here in the Beaufort Sea on 14 March 2011. To be less depending on the evaluation of only one day we extend the evaluation of the Beaufort Sea on 14 November 2004 (Figure 3.6).

We compared in total 155 reference leads to 173 clustered leads. On average, 57 % of the reference leads are detected, 11 % of the clustered leads are located where no reference lead occurs, and 17 % of the reference leads are detected multiple times despite clustering (Table 3.1). In the next section 3.4.2, we compare the lead distributions and test for a biased distribution of clustered leads.

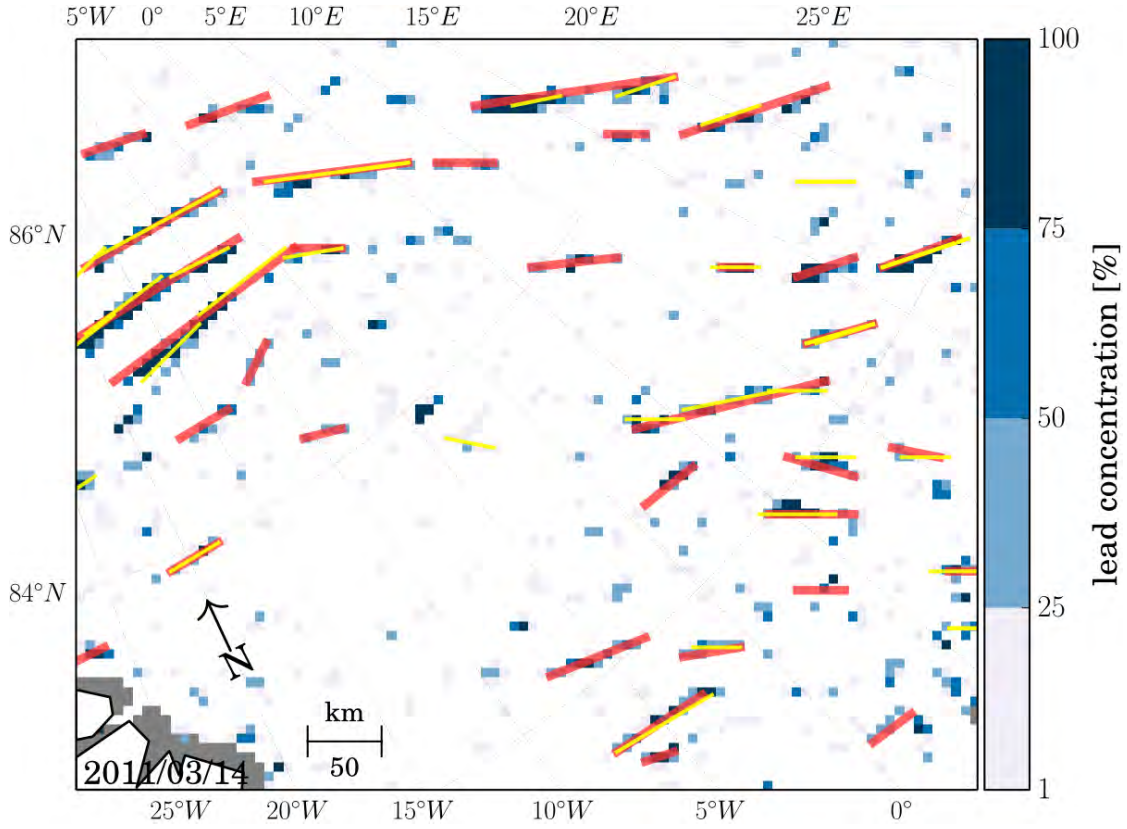

Figure 3.5: Comparison between reference leads (red) and clustered leads (yellow) detected by the Hough transform in the Fram Strait (F) on 14 March 2011.

Table 3.1: Summary of a comparison of reference leads with leads detected by the Hough transform in three regions: Fram Strait (F) on 14 March 2011 (Figure 3.5), Beaufort Sea (B1) on the same day (map not shown), and Beaufort Sea (B2) on 14 November 2004 (Figure 3.6).

	Region		
	F	**B1**	**B2**
percentage [%] of reference leads correctly detected Hough transform	55	58	57
percentage [%] of leads detected by the Hough transform that are located where no reference lead occurs	10	9	13
percentage [%] of reference leads that are detected multiple times	25	22	5
average length [km] of a reference lead	57	65	60
average length [km] of a lead detected by the Hough transform	48	50	53
number of reference leads	33	42	80
number of leads detected by the Hough transform	37	49	87

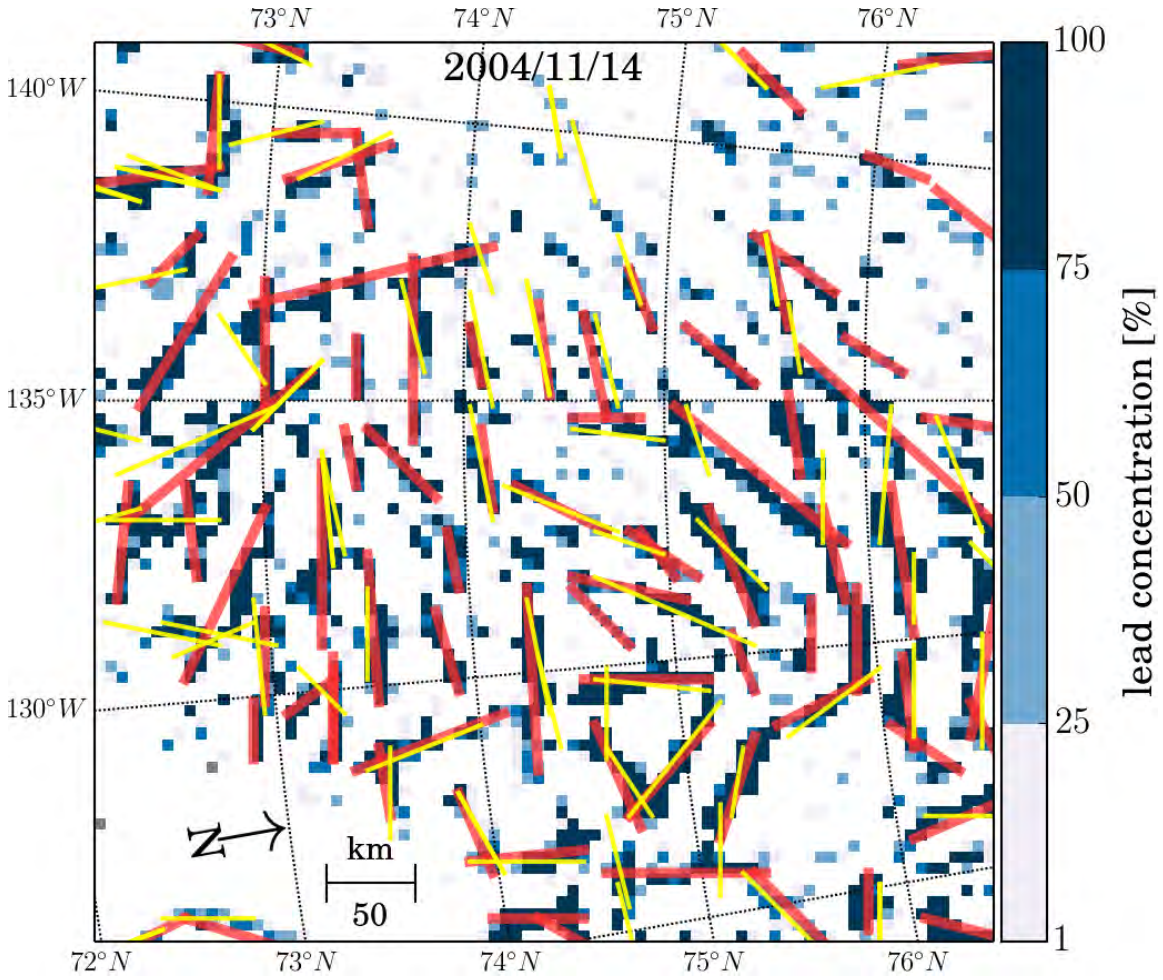

Figure 3.6: Comparison between reference leads (red) and clustered leads (yellow) detected by the Hough transform in the Beaufort Sea (B2) on 14 November 2004.

3.4.2 Distribution of Lead Orientations

After the qualitative comparison, we apply basic statistics to answer the question: Does the distribution of reference leads differ from the distribution of leads detected by the Hough transform? Before we present the basic statistical parameters, we introduce the concept of lead orientations described by angles. The lead orientation is defined as the angle between the 0° Greenwich meridian and the lead itself. A lead orientation of 0° or 180° is equal and is orientated parallel to the Greenwich meridian. The lead orientation is defined clockwise.

The need to calculate mean and standard deviation differently for circular data arises from the transition between 0° to 180°. We estimate the angular mean orientation

from a set of orientations after a common approach by Mardia and Jupp (2000):

$$\overline{X} = \sum_{i}^{N} \cos(2\theta_i) \tag{3.5}$$

$$\overline{Y} = \sum_{i}^{N} \sin(2\theta_i) \tag{3.6}$$

$$\overline{\theta} = \frac{\arctan(\overline{X}, \overline{Y})}{2} \tag{3.7}$$

with

$\overline{X}, \overline{Y}$ – unit vector components

θ – orientation angle between a lead and Greenwich meridian.

Olson (2011) showed that the four-quadrant arc tangent is line variant. Therefore, we multiply the lead orientations θ_i, which range from 0° to 180°, by 2 and divide the mean lead orientation $\overline{\theta}$ by 2.

We choose to calculate the angular standard deviation comparably to the classical standard deviation for data on a line. The advantages are that the standard deviation is well known and provides results in the same dimension as the angular mean whereas the angular standard deviation is non-dimensional and ranges between 0 and 1 (Miles and Barry, 1998; Mardia and Jupp, 2000). We can calculate the classical standard deviation, if lead orientations are distributed over a range smaller than 90°. If lead orientations are distributed over a range greater than 90°, we calculate the angular standard deviation by weighting the lead orientations around the angular mean that represents the center of the distribution. The source code of the algorithm written in the programming language python can be found in Listing A.1 in the Appendix. When we refer to mean or standard deviation, we refer henceforth to the angular mean or angular standard deviation.

The distribution of both, reference leads and leads detected by the Hough transform, show a similar shape in the histogram (Figure 3.7a). The mean values and standard deviations differ only by 2°. We use a bin width of 10° although the number of bins k should be estimated with Sturges' rule via $k = 1 + \frac{\log N}{\log 2}$ with N being the number of measurements and log being the decimal logarithm (Scott, 1992). For our example this would result in a number of bins $k = 6$.

We calculate the Probability Density Function (PDF) for the two distributions with a kernel-density estimate (Figure 3.7b). We select Scott's rule as bandwidth estimator: $h = \sigma N^{-1/(i+4)}$ with h being the bandwidth, σ being the kernel standard deviation, and i being the number of dimensions (Scott, 1992). In order to test if the two distributions origin from the same distribution we apply the two-sided Kolmogorov-Smirnov test. The two-sided Kolmogorov-Smirnov test works with the null hypothesis that two independent samples are drawn from the same continuous distribution. We cannot reject the null hypothesis at 25% or lower alpha values since the p-value of 0.21 almost equals 25%. The Kolmogorov-Smirnov test indicates that the two distributions differ slightly

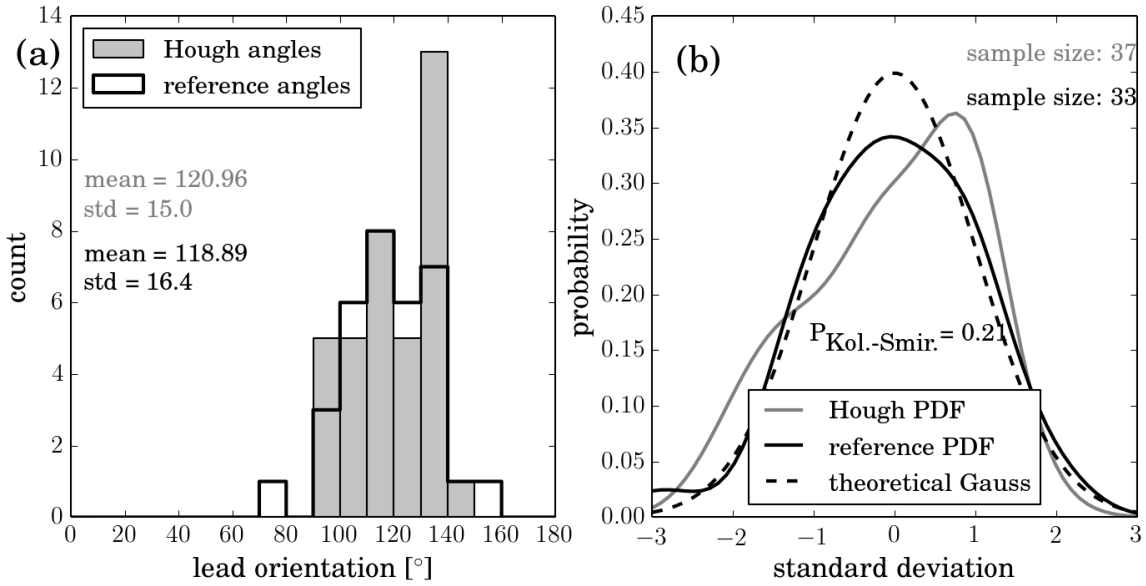

Figure 3.7: Comparison between lead orientations detected by the Hough transform with reference lead orientations in a histogram (**a**) and as probability density functions (**b**) in the Fram Strait on 14 March 2011. The Gauss curve in (**b**) is shown as reference.

although the PDFs obtained from a kernel density estimation differ when compared visually.

The mean orientation of the reference leads (29°) differs by 6° from the leads detected by the Hough transform (23°) in the Beaufort Sea on 14 March 2011 (not shown). The standard deviation is 9° smaller for leads detected by the Hough transform (18°). We cannot reject the null hypothesis at 17% or lower alpha values since the p-value is high (53%). The Kolmogorov-Smirnov test indicates that the two distributions are samples from the same distribution.

The distribution of both, reference leads and leads detected by the Hough transform, show a similar shape in the histogram of the Beaufort Sea on 14 November 2004 (Figure 3.8a). The mean values differ only by 1°, the standard deviations are identical. We cannot reject the null hypothesis at 11% or lower alpha values since the p-value is high (63%). The Kolmogorov-Smirnov test indicates that the two distributions are samples from the same distribution. The shapes of the PDFs show also a similar pattern.

We observe a strong accordance for mean and standard deviation in all examples. The distributions of lead orientation differ slightly or look similar. Leads detected by the Hough transform do not show a biased distribution of lead orientations in comparison to a distribution of reference lead orientations. The differences in the PDFs in Figure 3.7b might indicate an influence of multiple detections of some leads by the Hough transform. Even though we do not detect every reference lead, we still obtain a sufficient sample size to be capable of determining the regional mean lead orientation.

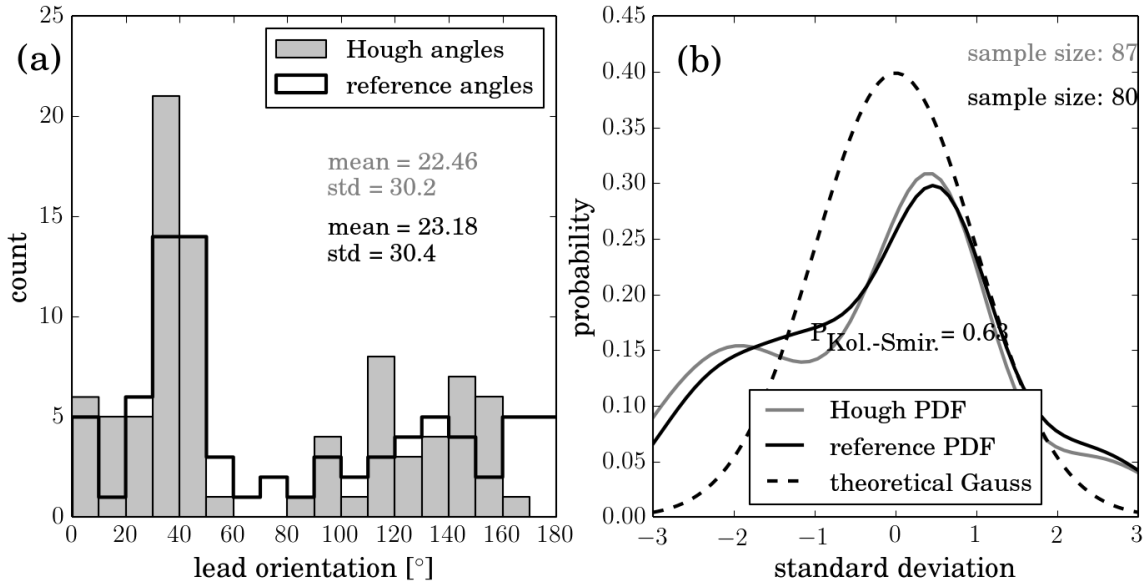

Figure 3.8: Comparison between lead orientations detected by the Hough transform with reference lead orientations in a histogram (**a**) and as probability density functions (**b**) in the Beaufort Sea on 14 November 2004. The Gauss curve in (**b**) is shown as reference.

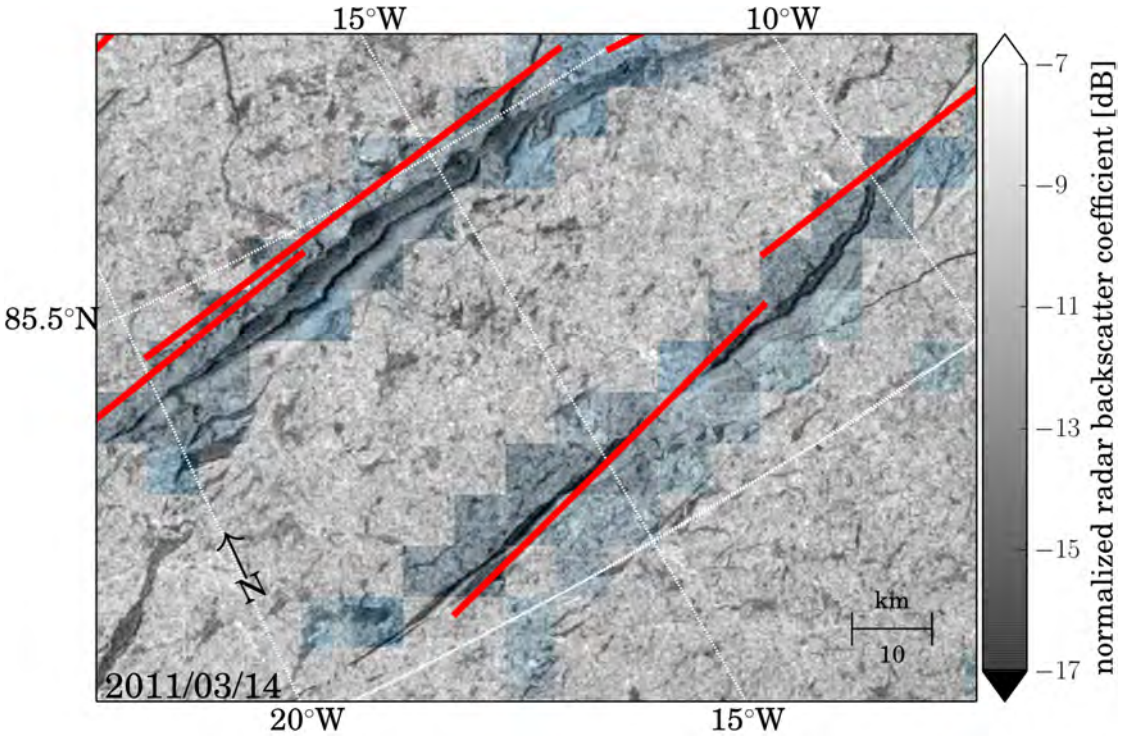

Figure 3.9: Validation of clustered leads detected by the Hough transform with an ASAR scene shows a high accordance for larger leads. Leads (red lines) inferred from AMSR-E lead concentration (blueish pixels) are compared to ASAR observations north of Greenland (box in Figure 3.3) on 14 March 2011.

3.4.3 Validation with ASAR

We validate the leads detected by the Hough transform with ASAR images. Compared to AMSR-E, ASAR WSM scenes have a finer ground resolution (∼70 m *vs.* ∼6 km). Accordingly, small leads and cracks, which are not resolved in an AMSR-E based lead concentration, are visible in an ASAR scene. We do not apply the Hough transform on ASAR scenes, because we choose to visually compare the orientation of automatically detected leads to leads in ASAR scenes. We compare 142 ASAR scenes to corresponding lead concentration maps and leads detected by the Hough transform from lead concentration maps. For consistency, we present an example in the Fram Strait on 14 March 2011 (Figure 3.9). Envisat ASAR scenes often cover the Fram Strait and the central Arctic. The Beaufort Sea is rarely covered by Envisat ASAR scenes.

Leads detected by the Hough transform (red lines) are located close to large leads visible in the AMSR-E based lead concentration (blueish pixels) and in the ASAR scene (Figure 3.9). In the upper part of Figure 3.9, we observe a small displacement between the leads detected by the Hough transform and leads visible in the lead concentration and in the ASAR scene. The small displacement is caused by the clustering as a comparison with Figure 3.3 shows. For each of the two large leads visible in the ASAR image in Figure 3.9, still two automatically detected leads remain despite clustering. However, this is rather the exception when we compare with Figure 3.3 and 3.5. Multiple detections of leads probably do not cause a bias in the distribution of lead orientations (*cf.* section 3.4.2).

The quality of the lead concentration is substantial, because the Hough transform can only detect leads that are resolved by the AMSR-E based lead concentration. We compare the lead orientation to ASAR and CryoSat-2 scenes in section 2.3. An extensive evaluation of the lead concentration can also be found in Röhrs et al. (2012).

3.5 Discussion

In the following sections, we discuss the uncertainties and limitations of the applied algorithm, which derives the lead orientation.

3.5.1 Uncertainties

The Hough transform by Galambos et al. (2002) does not include an internal uncertainty estimate for a detected line. Therefore, we cannot provide an individual uncertainty for every detected lead. In order to estimate the uncertainty, we distinguish between two types of lead detections: a lead that results from only one detection and a lead that results from at least two lead detections, which are clustered to one resulting lead. For every detected lead, we provide the C-score (equation (3.4) introduced in section 3.3.4) as a first measure of uncertainty. For every clustered lead orientation resulting from at least two lead detections we provide an uncertainty angle. We define the uncertainty angle as the angular standard deviation (*cf.* Section 3.4.2) of detected

leads which are clustered to one lead. To give an example, the uncertainty angles for the three clustered leads in the zoom of Figure 3.3 are 2.4°, 1.0°, and 5.4° from top to bottom.

In Table 3.2 we provide three average uncertainty estimates for the Fram Strait and the Beaufort Sea obtained on two different days. The root mean square deviation is calculated between reference lead orientations and corresponding lead orientations detected by the Hough transform. The root mean square deviation is lowest in the Fram Strait (F) compared to higher values in the Beaufort Sea (B1, B2). The mean uncertainty angle is lowest in the Fram Strait (F) and highest in the Beaufort Sea (B2) on 14 November 2004. A possible explanation for the differences is that leads are located closer to neighboring leads in the Beaufort Sea (B2). Furthermore, almost the entire directional range is covered with entries (Figure 3.8) and the number of leads is twice as high as in the Beaufort Sea (B2) compared to the Fram Strait (F).

Table 3.2: Root mean square deviation, uncertainty angle, and C-score calculated for three regions: Fram Strait (F) on 14 March 2011 (Figure 3.5), Beaufort Sea (B1) on the same date (map not shown), and Beaufort Sea (B2) on 14 November 2004 (Figure 3.6).

	Region		
	F	**B1**	**B2**
Root mean square deviation [°]	8.5	13.5	12.9
Mean uncertainty angle [°]	2.9	7.2	14.9
Mean C-score	0.94	0.94	0.88

Another source of uncertainty is the impact of a quantization effect. By quantization effect we mean that the shorter the lead length is, the less options the Hough transform has to fit a line through this lead. The quantization effect would become more pronounced if we detected for example leads with a length of only two pixels. The only possible lead orientations would be 0°, 45°, 90°, and 135°. We set the minimal line length of a lead to five pixels resulting in considerably more options for a possible lead orientation. The clustering of leads reduces the quantization effect by averaging leads with slightly different orientations. Nonetheless, the peak between 130° and 140° in the distribution of the Hough angles in comparison with the reference angles could partly be due to the quantization effect (Figure 3.7). However, the bin width should be 30° instead of 10° following Sturges rule given a sample size of around 35 angles.

Uncertainty is also caused by the tendency that the daily standard deviation of lead orientations is lower in the Fram Strait than in the Beaufort Sea. We assess this observation as a hint for more unidirectional lead orientations in the Fram Strait. On some days, the Hough transform detects unidirectionally distributed leads more accurately than isotropically distributed leads. Thus, lead orientations might be more robust in the Fram Strait, as well as north of Siberia, and the central Arctic than in the Beaufort Sea, where leads are more isotropically distributed and less certainly detectable.

3.5.2 Limitations

A limitation of our approach is the resolution of the AMSR-E based lead concentration. The applied algorithm to infer the lead concentration detects leads down to 3 km in width smaller than the AMSR-E pixel size of 6.25 km × 6.25 km by using an edge detecting filter (Röhrs et al., 2012). Due to both (A and B) 89 GHz scans available, AMSR2 allows to produce brightness temperature maps with a pixel size of 3.125 km × 3.125 km (Beitsch and Kaleschke, 2013). We did not yet apply the Hough transform on AMSR2 based lead concentration. Nonetheless, the AMSR-E sensor is able to detect fragments of leads narrower than 3 km in width. The structure of the fragments in the sea-ice cover is often none line-like and to infer a lead orientation from these geometrical structures is not robust. In order to get rid of single pixels originating from unresolved leads, we apply a morphological hit-or-miss transform that erases all single pixels in a binary lead concentration map. Furthermore, we are able to isolate lead structures from unresolved lead fragments by applying the Hough transform on the lead concentration.

As mentioned in section 3.3.5, we cannot find a combination of one threshold parameter and one line length that accurately fits for every day. This finding is a consequence of the spatial (between regions) and temporal (between days) variability. While on certain days longer leads prevail, a longer minimal line length combined with a lower threshold value accurately depicts the longer lead patterns. On other days, shorter leads prevail that are accurately depicted by a shorter minimal line length combined with a higher threshold value.

We do not analyze the distribution of lead length for two reasons: Firstly, the Hough transform tends to underestimate the lead length as visible in Figure 3.5. Secondly, the lead concentration does not resolve small lead structures. Thus, we cannot tell from the lead concentration alone where a lead begins or ends.

Chapter 4

A Nine-Year Climatology of Arctic Sea-Ice Lead Orientation and Frequency from AMSR-E[1]

4.1 Introduction

After evaluating the automatically detected lead orientations with manually detected lead orientations and comparing the automatically detected leads to measurements of the independent Advanced Synthetic Aperture Radar (ASAR) sensor in chapter 3, we present the first results covering the entire time series from 2002 to 2011. The scope of this chapter is to provide a time series of lead orientation for the lifespan of Advanced Microwave Scanning Radiometer for Earth Observing System (AMSR-E) from 2002 to 2011. This allows us to derive a climatology of automatically-obtained lead positions and orientations that can be prolonged into the future by applying our algorithm to Advanced Microwave Scanning Radiometer 2 (AMSR2) observations.

This chapter is organized as follows: First results of Arctic-wide lead distributions are presented in section 4.2. In section 4.3, the resulting lead distributions are discussed and compared to former studies.

4.2 Lead Orientation

We apply the Hough transform to derive the lead orientation for every day in winters from 2002 to 2011. In section 4.2.1, we present a map showing the mean lead orientation from 2002 to 2011. Maps of monthly nine-year average lead orientations are shown in section 4.2.2. We present the monthly variability of lead orientations in the Fram Strait and the Beaufort Sea in section 4.2.4.

[1]This chapter (except for section 4.2.3 and Figure 4.7) has been published in: Bröhan, D., Kaleschke, L. (2014). A Nine-Year Climatology of Arctic Sea Ice Lead Orientation and Frequency from AMSR-E. Remote Sens., 6(2):1451-1475.

4.2.1 Average Lead Orientation from 2002 to 2011

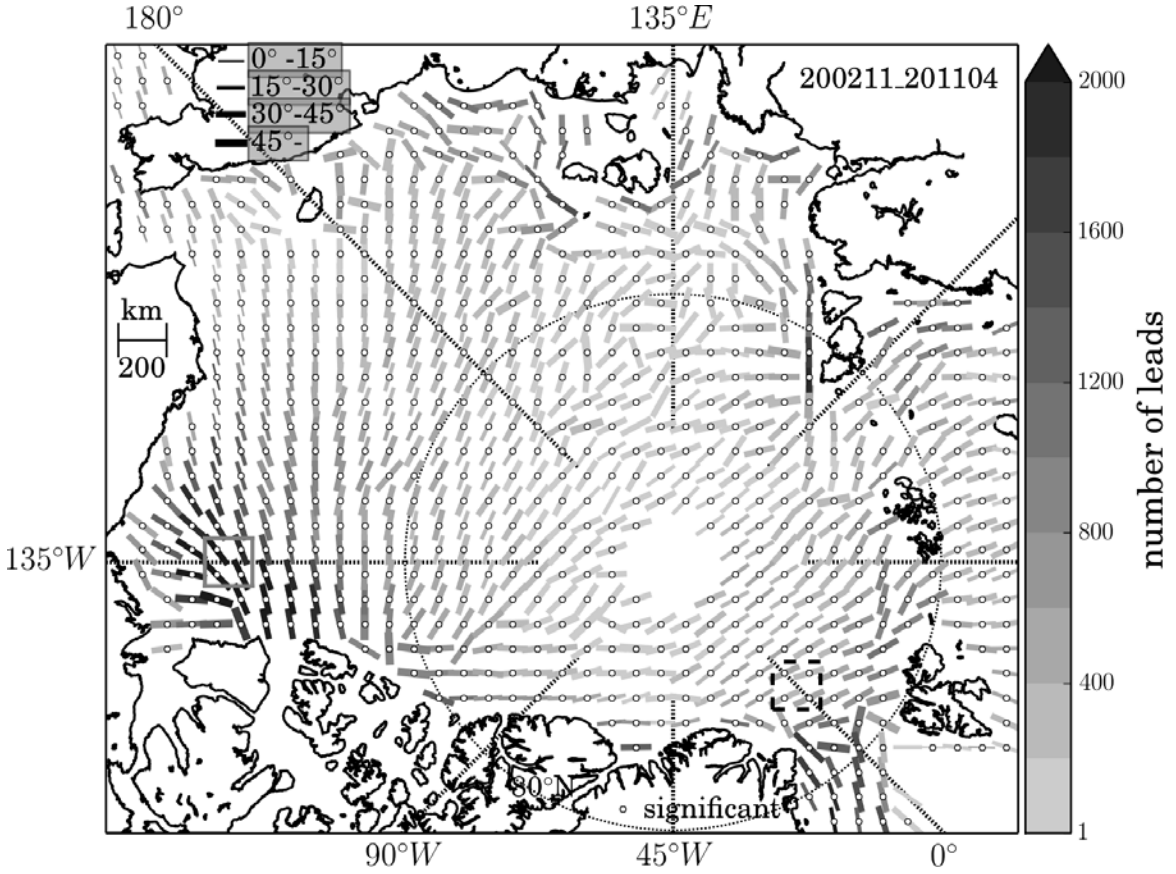

Figure 4.1: Average lead orientation for winters from 2002 to 2011. Grey colors depict the number of leads while the width of a lead measures the standard deviation of all lead orientations in a 100 km × 100 km cell. White dots on top of a line indicate that the lead orientations are not randomly distributed on a confidence level of 99%. The black dashed and gray squares mark sub regions which are going to be analyzed in section 4.2.4.

We show the spatial distribution of lead orientation in the Arctic in Figure 4.1. All lead observations from 2002 to 2011 are spatially averaged in cells of 100 km in length. The line orientation in a cell represents the mean lead orientation. Grey colors indicate the number of measurements - the darker, the more measurements. The line thickness depicts the standard deviation of all lead orientations in a cell. The standard deviation of random lead orientations in a cell equals roughly 55°. The pole hole is due to missing observations and due to some artificial pattern detected by the Hough transform at the edge of the pole hole which were cut out.

In order to identify cells in which the lead orientations are equally distributed from 0° to 180°, we conduct a χ^2-test within a Monte Carlo test for each cell. We apply the χ^2-test for two distributions: the distribution of observed lead orientations detected by the Hough transform H_{obs} in a cell and the distribution of random lead orientations H_{rand} from 0° to 180°. We calculate the frequency of occurrence from the observed and random distributions. The χ^2-test is applied 10.000 times to the observed as well as the random frequencies with changing random lead orientations for every individual

χ^2-test. The χ^2-test checks the null hypothesis whether the observed lead orientations have the given frequencies of the random lead orientations. The χ^2-test returns one probability for the null hypothesis not being rejected in each loop. The 10.000 individual probabilities are averaged to a mean probability $\overline{p}$. If the mean probability $\overline{p}$ is smaller than 0.01, the lead orientations in a cell will belong to a confidence level of 99% statistically significant non-random distribution, which is marked by a white dot in Figure 4.1. A prerequisite of the χ^2-test is that at least five measurements must occur in each cell. With this test we do not check whether one, two, or several statistically significant mean lead orientation prevail. We check whether the lead orientations belong to a statistically significant non-random distribution.

We observe some distinct pattern in Figure 4.1: Leads are often orientated coast-parallel except for some regions like the Canadian Archipelago near Alaska or the region north of Spitsbergen and Franz Josef Land. Most leads occur in the southern Beaufort Sea. Local maxima of lead occurrence are located north of Siberia and in the Fram Strait exit region.

The overall spatial pattern of the average lead orientation is rather smooth, spatial variations in lead orientation occur over larger distances. In the Fram Strait, leads are orientated parallel to a line drawn from northern Greenland to northern Spitsbergen. Lead orientation varies more in the Beaufort Sea: From almost being perpendicular to the coastline of Alaska to tilting more to Greenwich meridian for leads located away from the coastline.

4.2.2 Monthly Nine-Year-Average Lead Orientation

In section 4.2.1, we presented the spatial distribution of lead orientations that does not contain information about the spatio-temporal variability from 2002 to 2011. In this section, we show monthly averages that represent the temporal variability of all years (Figure 4.2). The standard deviation is again shown as line thickness and white dots on top of a cell indicate that the shown lead orientations belong to a statistically significant non-random distribution. We use the Monte Carlo approach as presented in section 4.2.1 to test if lead orientations have a random distribution.

The overall spatial pattern is not that smooth for every month. Lead orientations vary especially in the central Arctic and for months from February to April as compared to the average over all years (Figure 4.1). More leads are detected at the beginning of winter with lead occurrence always peaking in the Beaufort Sea. For the Beaufort Sea, we observe that the amount of leads that are orientated perpendicular to the coastline of Alaska decreases with ongoing winter. In the Fram Strait exit region, leads are orientated almost parallel to Greenwich meridian in November, while the leads get more and more orientated perpendicular to Greenwich meridian as the winter season advances. Leads orientated parallel to the coast of Siberia build up from December/ January to April. In the central Arctic, leads perpendicular to Greenwich meridian tend to tilt parallel to the coastline of Alaska with ongoing season. Contemporary to this directional tilt, the number of detected leads declines like in every region of the Arctic.

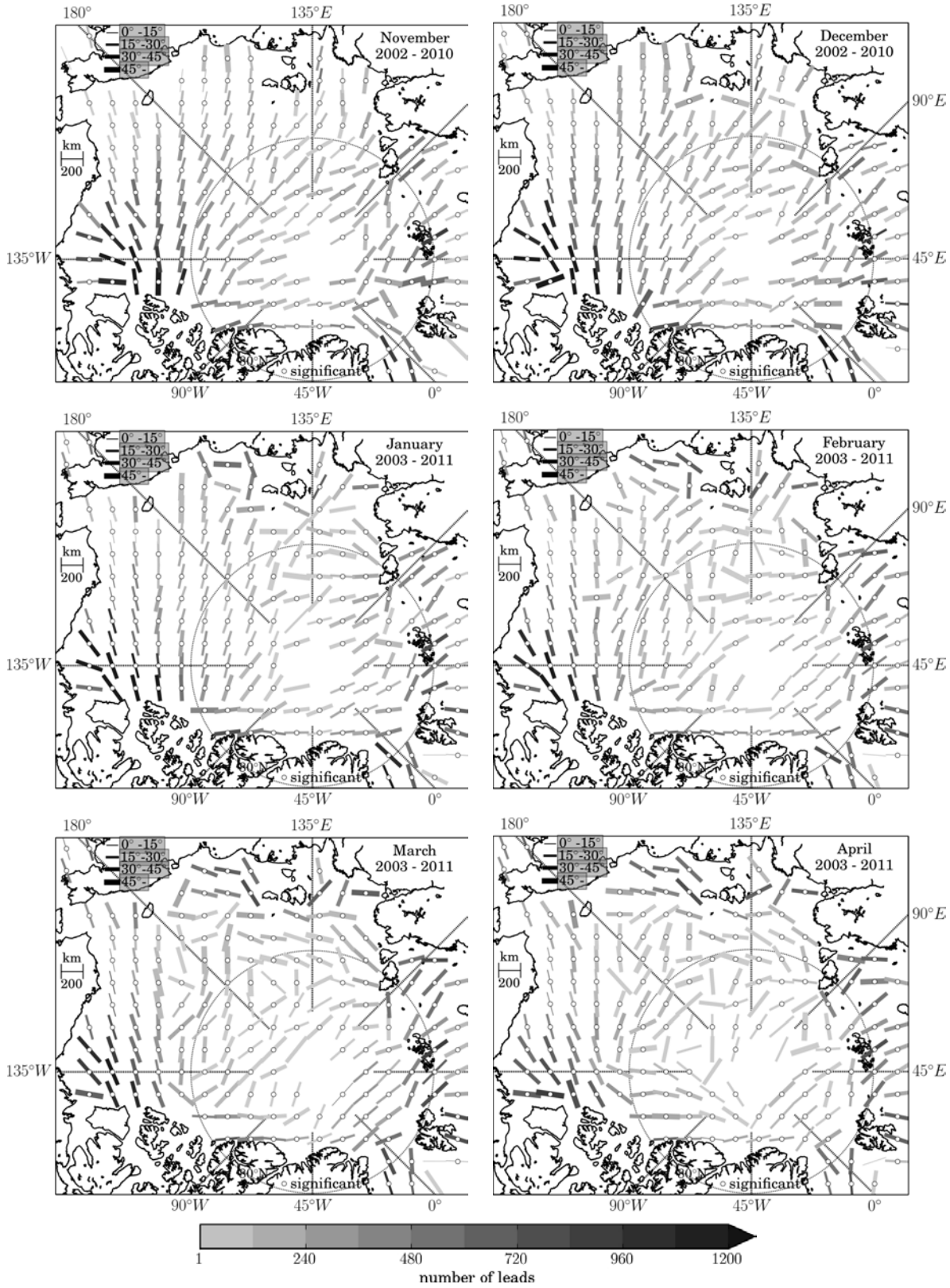

Figure 4.2: Monthly averaged lead orientation from 2002 to 2011. Grey colors display the number of leads while the width of a lead measures the standard deviation of all lead orientations in a 200 km × 200 km cell. White dots on top of a line indicate that the lead orientations are not randomly distributed on a confidence level of 99%.

4.2.3 Monthly Average Lead Orientation

In this section, we illuminate the spatial distribution of the monthly averaged lead orientation. For practical reasons, we will only present two examples: Novmeber 2002 and February 2005. In both maps of Figure 4.3, the line orientation represents the

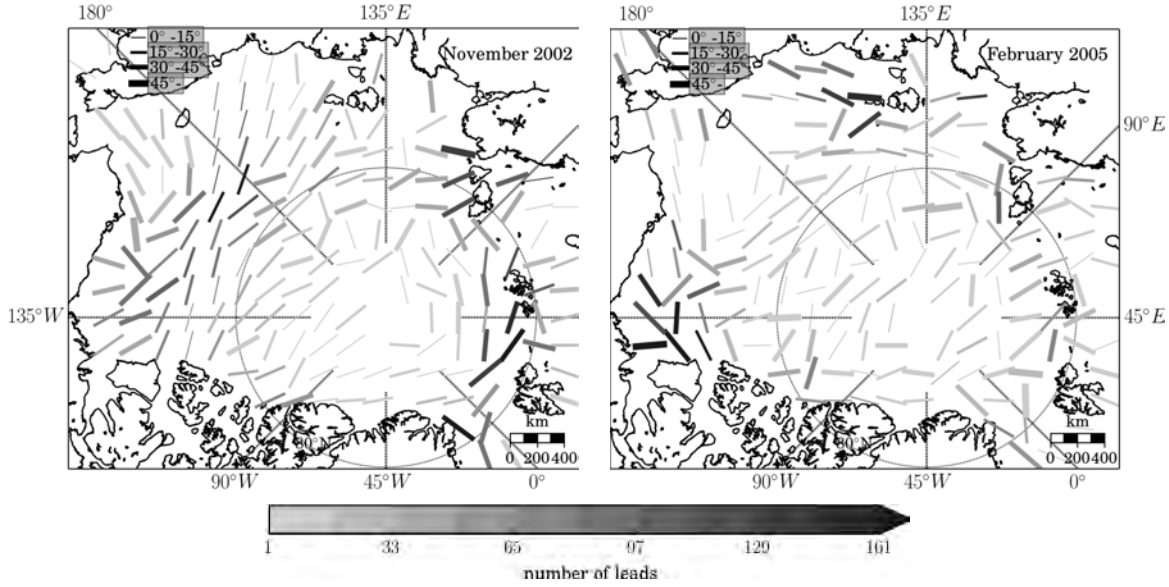

Figure 4.3: Monthly averaged lead orientation for November 2002 and February 2005. Grey colors represent the number of leads while the width of a lead measures the standard deviation of all lead orientations in a 200 km × 200 km cell.

mean lead orientation in a 200 km × 200 km cell. The standard deviation is shown as line thickness and grey colors represent the number of lead measurements.

In November 2005, leads occur frequently in the northern Beaufort Sea, east of Severnaya Zemlya, and northeast of Svalbard. The mean lead orientation reveals a lead structure similar in orientation extending from the northern Beaufort Sea to Severnaya Zemlya. In February 2005, we observe two maxima of lead occurrences located in the southern Beaufort Sea and north of Siberia. In the Central Arctic, an overall mean lead orientation dominates that is perpendicular to Greenwich meridian. Furthermore, we observe a smililar orientated band of leads extending from the Beaufort Sea to the East Siberian Sea.

4.2.4 Time Series of Lead Orientation in the Fram Strait and in the Beaufort Sea

In order to get an idea of the monthly variability, we show the lead orientation for two sub regions of the Fram Strait and the Beaufort Sea from 2002 to 2011 (Figure 4.4). Like in Figure 3.7, we depict the lead orientation as angles. The graph of the Fram Strait is depicted in black, the graph of the Beaufort Sea in gray, consistent to the gray and black boxes that mark the corresponding sub regions in Figure 4.1. Both graphs are based on monthly averages.

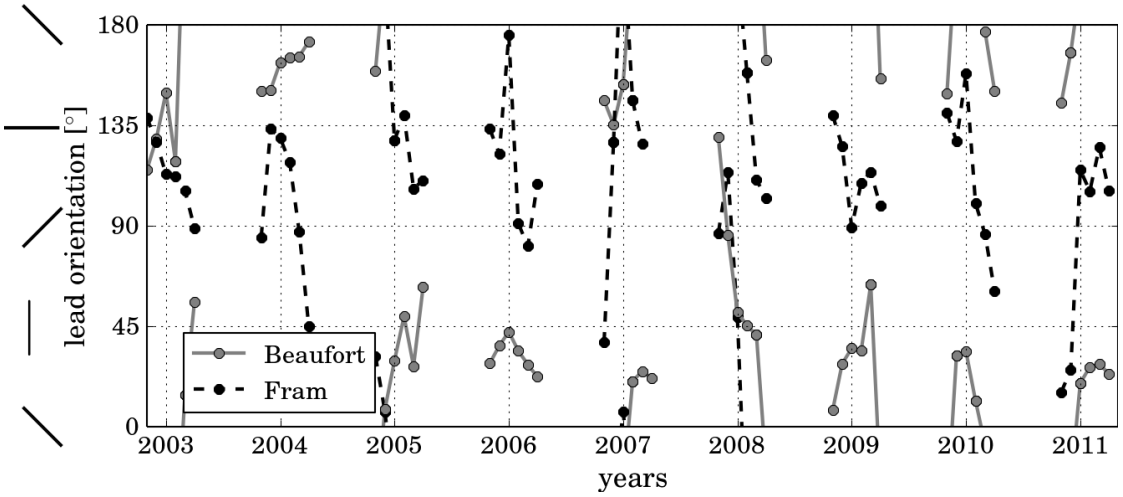

Figure 4.4: Time series of monthly averaged lead orientations in sub regions of the Beaufort Sea (black dashed) and the Fram Strait (gray) from 2002 to 2011. Both, 0° and 180°, are orientated parallel to Greenwich meridian. The precise location of the two sub regions is indicated by boxes in Figure 4.1. The lines on the left hand side illustrate the corresponding lead orientation.

The lead orientations in both regions are largely distributed. The most prominent exceptions from the large spread in lead orientation are the years 2004 and 2006 in the Beaufort Sea. In the Fram Strait, leads are orientated more parallel to Greenwich meridian in the beginning of a season, but become more perpendicular to Greenwich meridian during the season. We observe that leads get more orientated parallel to Greenwich meridian in the Beaufort Sea as the season advances. Still, all of the tendencies are dominated by large fluctuations within the seasons.

4.3 Discussion

In the discussion, we compare the results to two reference studies in section 4.3.1. In section 4.3.2, we comment on the patterns of obtained lead orientations although we cannot provide a complete explanation.

4.3.1 Comparison to Former Studies

Reference publications covering the lead orientation in the Arctic are rare. We compare our results qualitatively to the results of Miles and Barry (1998) and Lindsay and Rothrock (1995). Lindsay and Rothrock (1995) show a map of the Fram Strait for 25 February 1989 and 1 March 1989 with leads orientated perpendicular to Greenwich meridian. We often observe the same lead orientation in the Fram Strait.

Miles and Barry (1998) show maps of mean lead orientation in the Beaufort Sea for winters from 1979 to 1985. When we compare their pattern of lead orientation to mean lead orientations from 2003 to 2008 (Figure 4.5), we observe a shift away from

the coastline. The mean lead orientation of Miles and Barry (1998) remains more perpendicular to the coastline whereas the recent mean lead orientation is tilted parallel to the coastline. Near the coastline the lead orientation is similarly orientated. We do not know at this point the reasons that explain the difference between the two time periods. As a first indicator that other variables connected to lead occurrences also changed, we show the mean divergence for fall and winter in Figure A.5 in the Appendix. The divergence pattern differs from the pattern observed by Miles and Barry (1998). To find out if the difference in lead orientation can be explained by changes in sea-ice deformation and the spinning up of the Beaufort gyre during the 2000s (Giles et al., 2012; Morison et al., 2012) is subject to future work. As already pointed out in the previous section, our method may not be that robust in the Beaufort Sea due to the more isotropically distributed leads compared to other regions of the Arctic.

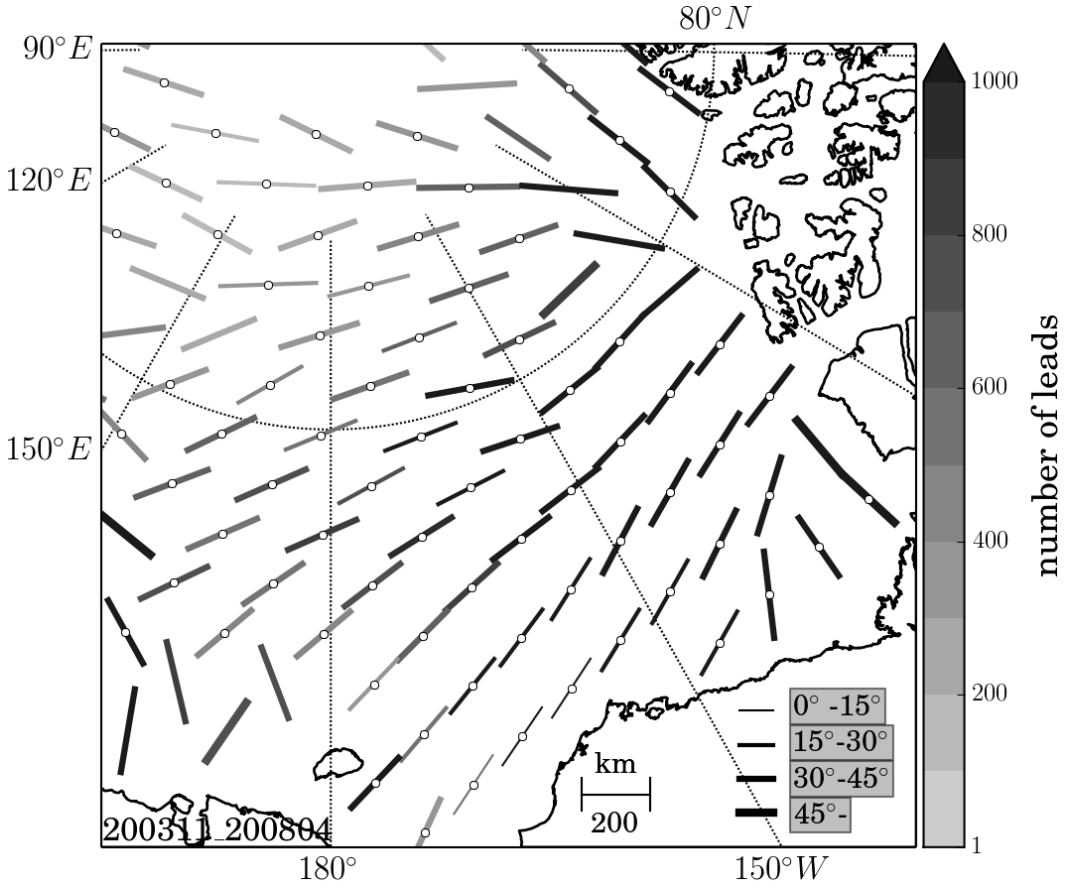

Figure 4.5: Average lead orientation from 2003 to 2008 in an identically rotated map as the map in Figure 6 of Miles and Barry (1998). Grey colors display the number of leads while the width of a lead measures the standard deviation of all lead orientations in a 200 km × 200 km cell. White dots on top of a mean lead orientation indicate a statistically significant preferred orientation (Miles and Barry, 1998).

Miles and Barry (1998) found statistically significant preferred lead orientations in a cell with the strength of preference R (Miles and Barry, 1998; Mardia and Jupp, 2000),

which is defined as:

$$R = N^{-1}\sqrt{\overline{X}^2 + \overline{Y}^2}. \tag{4.1}$$

The strength of preference R ranges from 0 for random orientations to 1 for only one orientation occurring in a cell (Miles and Barry, 1998). Miles and Barry (1998) state that a cell has a statistically significant preferred lead orientation for $R \gtrsim 0.25$ and $N \geq 60$ with N being the number of observations. We find statistically significant preferred lead orientations in 77 out of 92 grid cells in comparison to 38 out of 63 grid cells for Miles and Barry (1998). The rise of about 30% in the number of cells with statistically significant preferred lead orientation is partly due to fewer randomly orientated lead orientations north of 80°N and in the Bering Sea entrance region in our study.

We did not use the test by Miles and Barry (1998) in previous sections to check for a statistically significant preferred mean lead orientation, because we think it is more suitable to check if lead orientations are statistically significantly non-randomly distributed in a cell. Furthermore, Miles and Barry (1998) do not account with their test for a potential secondary preferred mean orientation or other shapes of the distribution.

4.3.2 Distribution of Lead Orientation

The smooth spatial pattern indicates a spatial coherence of lead orientations during the entire winter season (Figures 4.1 and 4.2). One reason for this spatial coherence might be orographically forced, because leads tend to be orientated perpendicular to a coastline. Leads are only orientated parallel to the coastline north of Greenland, north of Siberia, and partly north of Alaska. The coast-parallel lead structure north of Greenland and partly north of the Canadian Archipelago is probably due to thicker multi-year ice. In these regions, we observe that sea ice tends to break up parallel to the sea-ice thickness gradient and to the shoreline. The situation north of Siberia differs: In the beginning of winter, leads are perpendicular to the shoreline but they tilt parallel to the shoreline when the fast-ice develops north of Siberia in the Barents sea, Kara sea (Olason, 2012), and Laptev sea (Figure 4.2). In the Fram Strait exit region, leads orientated perpendicular to Greenwich meridian can be interpreted as traces of blocking events or arches (Kwok et al., 2010) from January to April (Figure 4.2).

Leads are statistically significantly non-randomly orientated almost everywhere in Arctic winters when averaged over all years (Figures 4.1 and 4.2). The few cases in which a cell with a random distribution of lead orientations occurs may partly be due to a small number of observations in that cell. The existence of a statistically significant non-random distribution of lead orientations in many cells is also connected to both the spatial dimensions of a cell and to the time period over which it is averaged. Lowering the time period and decreasing the cell dimensions results in fewer leads per cell. This causes more randomly orientated leads even in cells with many lead observations like in the Beaufort Sea.

As an example, we show the distribution of lead orientations for two sub regions (Figure 4.6) from 2002 to 2011 in order to demonstrate that we obtain statistical-significant

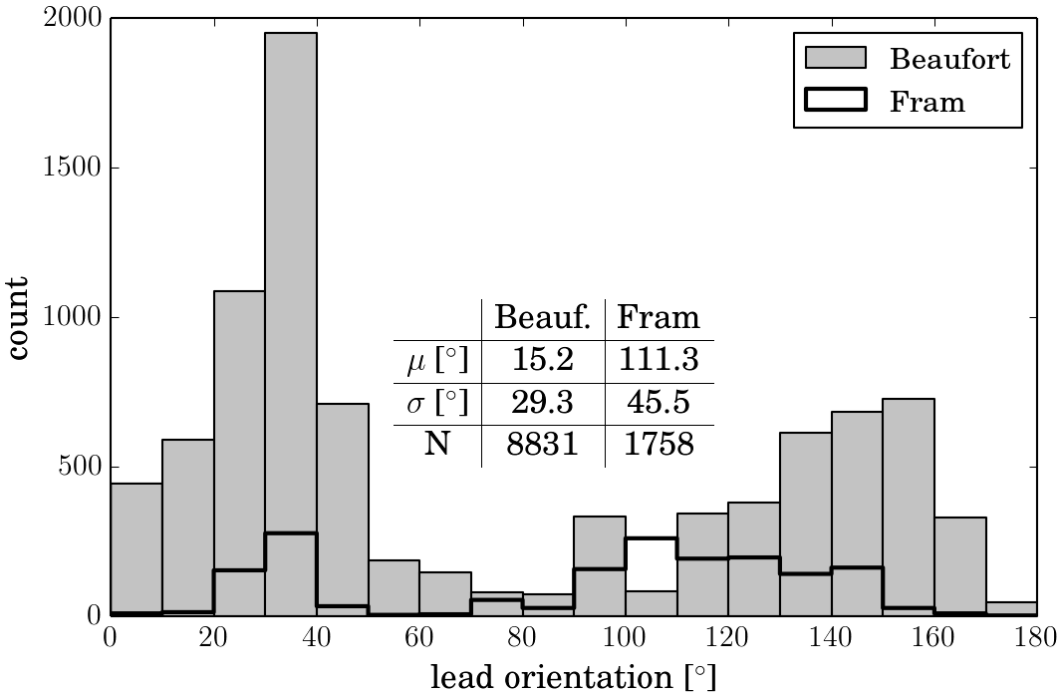

Figure 4.6: Histogram of lead orientations in sub regions of the Beaufort Sea (gray) and the Fram Strait (black solid line) from 2002 to 2011. The precise locations of the two sub regions are shown in Figure 4.1.

non-random lead distributions as indicated in Figures 4.1 and 4.2. The distribution of lead orientations in the Beaufort Sea peaks in the bin from 30° to 40° and shows a secondary peak in the bin from 150° to 160°. The distribution of lead orientations in the Fram Strait peaks in the bin from 90° to 100° and shows a secondary peak in the bin from 30° to 40°. The lead orientations in the Fram Strait are much more broadly distributed which is consistent with the larger standard deviation. Visually, the distributions show no similarity to a random uniform distribution in both regions. Consistently, the χ^2-test applied within a Monte Carlo simulation like in section 3.4.2 returns very low probabilities for randomly distributed lead orientations.

The histogram (Figure 4.6) shows that the lead orientation is not necessarily normally distributed around the mean orientation depicted in Figure 4.1. In order to get the equivalent of a histogram in each cell of Figure 4.1, we show the distribution of lead orientations in cells of 100 km in length in Figure 4.7. In each cell, the lead orientation is binned in 20° intervals while the line thickness represents the lead occurrences in a bin. In a cell with one preferred lead orientation, all lead occurrences are focused on one bin. In a cell with an isotropic distribution of lead orientations, all bins are equally covered. Both cases rarely occur in Figure 4.7, instead we often observe a mixture of both cases.

In regions with many lead occurrences like the Beaufort Sea, Fram Strait, and regions north of Siberia and Severnaya Zemlya (*cf.* Figure 4.1 for the total number of leads), we often observe a preferred mean lead orientation. We observe a strong secondary lead orientation in the southern Beaufort Sea, the Fram Strait exit region, and north of Siberia. Furthermore, all bins are covered in most cells with many lead occurrences.

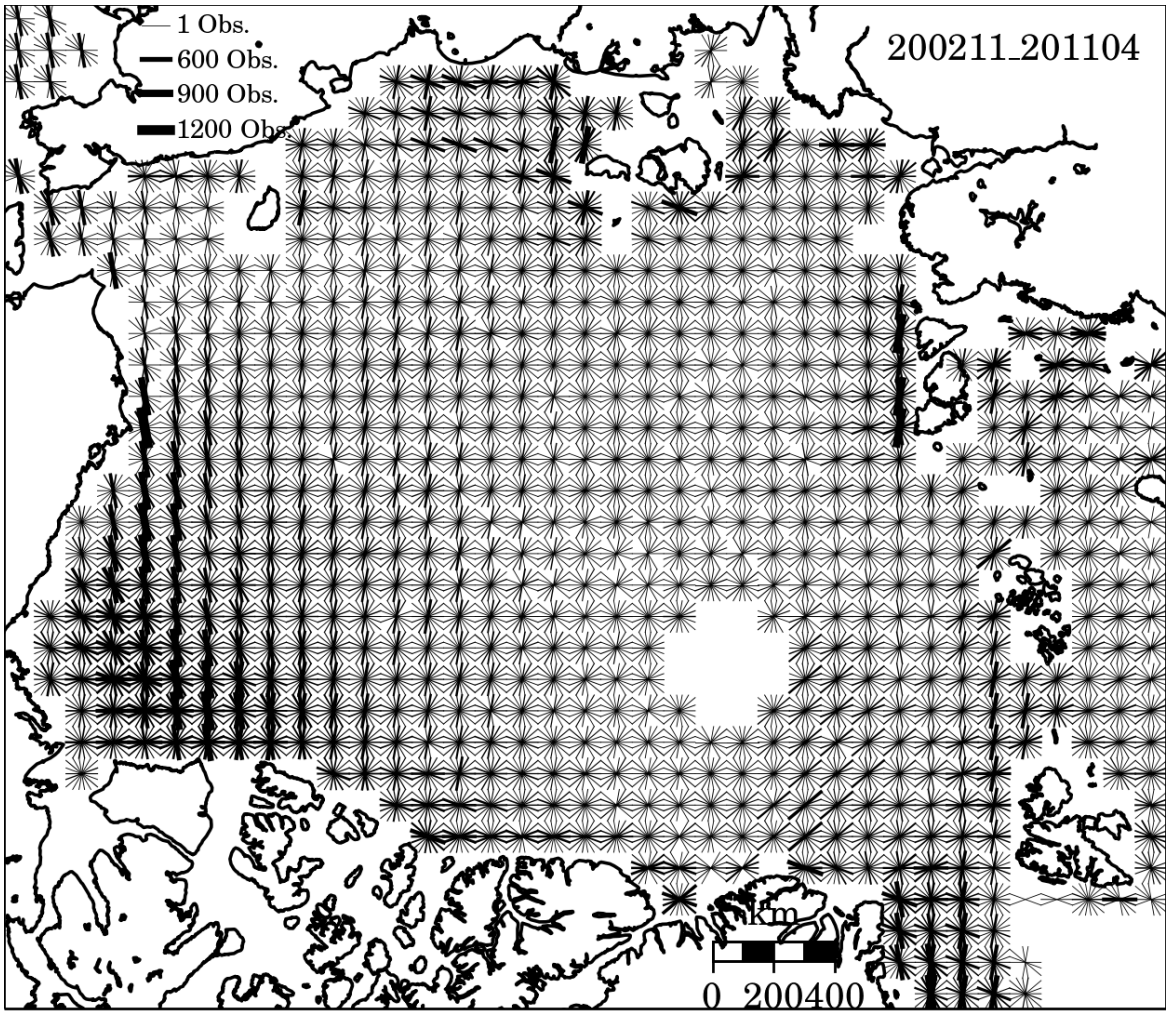

Figure 4.7: Distribution of lead orientation from 2002 to 2011. Lead orientations are binned in 20° intervals in a 100 km × 100 km cell. The width of a line represents the number of lead observations.

Lead orientations in the Central Arctic appear isotropically or randomly distributed although the lead orientation are statistically significantly non-randomly distributed. This contradiction is caused by the poor presentation of smaller lead occurrences in Figure 4.7.

When we look at the average spatial pattern of lead orientation from 2002 to 2011 (Figure 4.1), one can ask: What are the prevailing processes that cause this pattern? An in-depth answer to this question would clearly require a comparison to additional observations, like surface wind or sea-ice drift. In the following chapter, we compare the lead orientation to the sea-ice drift.

Chapter 5

Comparison of Leads and Sea-Ice Deformation

5.1 Introduction

So far, we have developed an algorithm that automatically detects the orientation of leads from Advanced Microwave Scanning Radiometer for Earth Observing System (AMSR-E) measurements. Figure 4.1 shows the mean lead orientation and occurrence from 2002 to 2011. The pattern of lead orientation has a lot of structural coherence. The question we would like to answer is: What causes the lead orientation and occurrence pattern? Because a lead results from a mechanical force acting on the sea-ice cover, the first variable to look at is the sea-ice drift. Similar to Miles and Barry (1998); Marsan et al. (2004); Heygster et al. (2012), we hypothesize that leads originate from divergence and shear of the sea-ice drift. Thus, we investigate the influence of sea-ice drift and derived deformation parameters, like divergence, shear, and vorticity, on lead occurrences and orientation.

Miles and Barry (1998) provided a climatology of leads for the western Arctic lasting from 1979 to 1985. They compared leads to deformation parameters derived from drift buoys. The most interesting parameter is the shear orientation angle, because the shear orientation angle connects the directional information of the sea-ice drift with the directional information of the lead orientation. Miles and Barry (1998) found that the mean shear orientation angle is perpendicular to the mean lead orientation. As Miles and Barry (1998) missed to provide the definition of the shear orientation angle, we try to reproduce the shear orientation angle in section 5.3.3.

In the following section, we briefly introduce the sea-ice drift datasets used in this chapter. We provide the definition of the deformation parameters in section 5.3. Section 5.4 contains the results: We compare the AMSR-E based sea-ice drift with the RADARSAT Geophysical Processor System (RGPS) drift as reference on the weekly timescale. The AMSR-E based sea-ice deformation parameters are compared to the corresponding lead distributions of all time slices covered in chapter 4. In section 5.5, we discuss resulting tendencies derived from a comparison of sea-ice deformation and lead frequency and orientation.

5.2 Sea-Ice Drift Datasets

Sea-ice drift can be estimated via buoys drifting with the ice. This Lagrangian approach is limited, if we need to monitor an area like the Arctic, because this would require a large number of drifting buoys. Another way of obtaining sea-ice drift is to derive the motion of sea ice from brightness temperature measured by satellite-borne passive microwave sensors like AMSR-E. In order to calculate deformation parameters, like divergence, vorticity, and shear rate, we use a sea-ice drift product provided by Ifremer: The product is the AMSR-E 2-day sea-ice drift with a resolution of 31.25 km $\times$ 31.25 km in grid cell size (Ezraty et al., 2007). The sea-ice drift based on AMSR-E measurements has the advantage that it covers the same time period as for the lead observations in chapter 4.

Ezraty et al. (2007) apply an algorithm based on correlation between consecutive time-lagged brightness temperature maps (maximum cross correlation) in order to derive the sea-ice drift (Girard-Ardhuin et al., 2008). The algorithm contains a set of internal controls. The internal controls partly consist of a comparison between the sea-ice drift direction and the European Centre for Medium-Range Weather Forecasts (ECMWF) modeled surface wind direction. If the angle between the sea-ice drift vector and the surface wind vector reaches 180°, the sea-ice drift vector is neglected. During the internal control, the algorithm checks also for consistent drift vectors resulting from the 89 GHz brightness temperature maps at horizontal polarization (H) and at vertical polarization (V). Drift vectors are dismissed if they do not pass the internal controls. This procedure results in data gaps for a 2-day sea-ice drift map.

In section 5.4.1, we compare the moderate-resolution (31.25 km $\times$ 31.25 km grid resolution) AMSR-E based sea-ice drift to high-resolution (10 km $\times$ 10 km grid resolution) RGPS sea-ice drift. The RGPS uses Synthetic Aperture Radar (SAR) measurements to infer the sea-ice drift via a maximum cross correlation approach. A detailed description of the RGPS sea-ice drift is given by Kwok (1998). Weekly RGPS sea-ice drift maps of the Western Arctic, covering winters and summers from 1996 to 2008, are online available at `http://rkwok.jpl.nasa.gov/graphics/index.html`.

5.3 Methods

In this section, we introduce the deformation parameters that we derive from the sea-ice drift. We apply the routines for calculating the deformation parameters to idealized sea-ice drift settings with the same grid spacing as for the AMSR-E sea-ice drift fields. All deformation parameters are computed using central differences in the interior, and first differences at the boundaries. Furthermore, we attempt to derive the shear orientation (Miles and Barry, 1998) in section 5.3.3.

5.3.1 Divergence

Horizontal divergence ϵ_d is defined as the summed component-wise fractional rate of change in the sea-ice drift for a reference area:

$$\epsilon_d = \frac{\partial u}{\partial x} + \frac{\partial v}{\partial y} \tag{5.1}$$

with

u – x-component of the sea-ice velocity
v – y-component of the sea-ice velocity.

Divergence is caused by a directional change in sea-ice velocity along an ice sea-drift trajectory, and by confluence or diffluence. Confluence means that sea-ice drift trajectories flow together, and diffluence means that ice drift trajectories flow apart. Figure

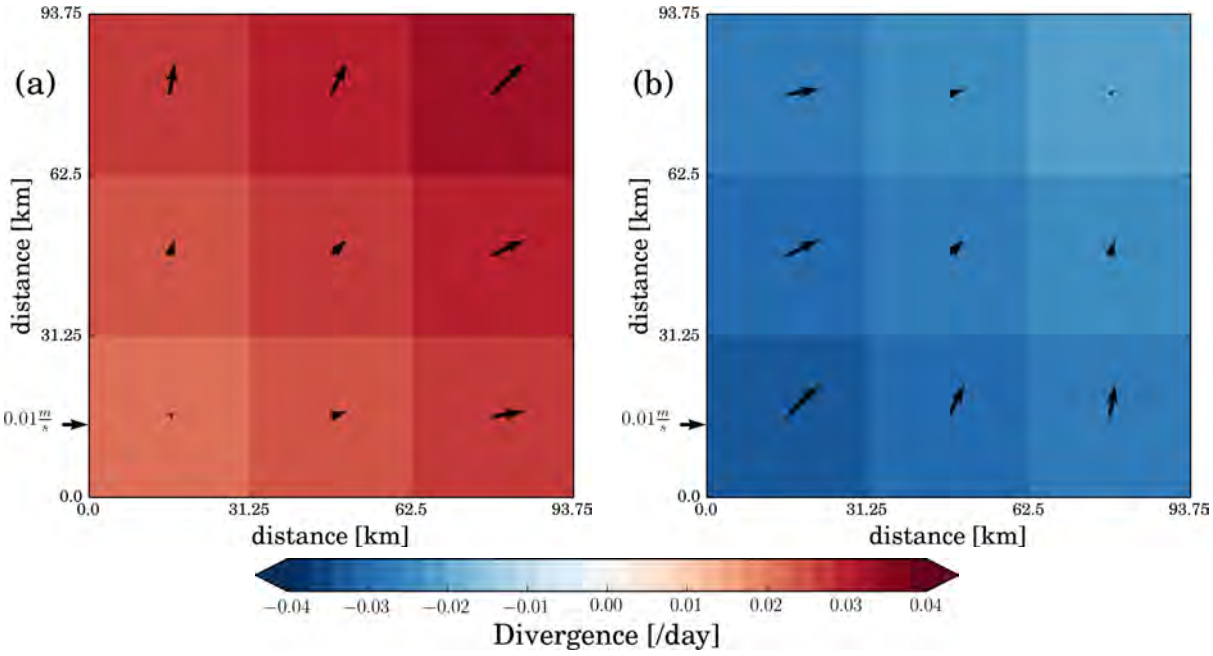

Figure 5.1: Divergence (**a**) and convergence (**b**) depicted as colored fields. The vectors illustrate idealized sea-ice drift settings. The cell size corresponds to an area of 31.25 km × 31.25 km, identical to the AMSR-E sea-ice drift.

5.1a shows divergence for an idealized sea-ice drift setting depicted by black vectors. Negative divergence is defined as convergence (Figure 5.1b).

In a field of pure divergence, vorticity (rotation) is zero. Thus, a field of pure divergence is called *irrotational*. Such a field of pure divergence shows also no shear. Measurements of horizontal divergence are independent of the rotation of the coordinate system (Bluestein, 1993). Therefore, divergence is considered as *rotationally invariant*.

5.3.2 Vorticity

Vorticity indicates the direction and strength of rotation for the sea-ice drift. The term vorticity ζ is defined as the rate of change of the velocity's x-component in y-direction subtracted from the rate of change of the velocity's y-component in x-direction:

$$\epsilon_v = \frac{\partial v}{\partial x} - \frac{\partial u}{\partial y}. \tag{5.2}$$

Positive vorticity (Figure 5.2a) is defined as anti-clockwise rotation, negative vorticity (Figure 5.2b) is defined as clockwise rotation. Vorticity is *rotationally invariant* (Bluestein, 1993).

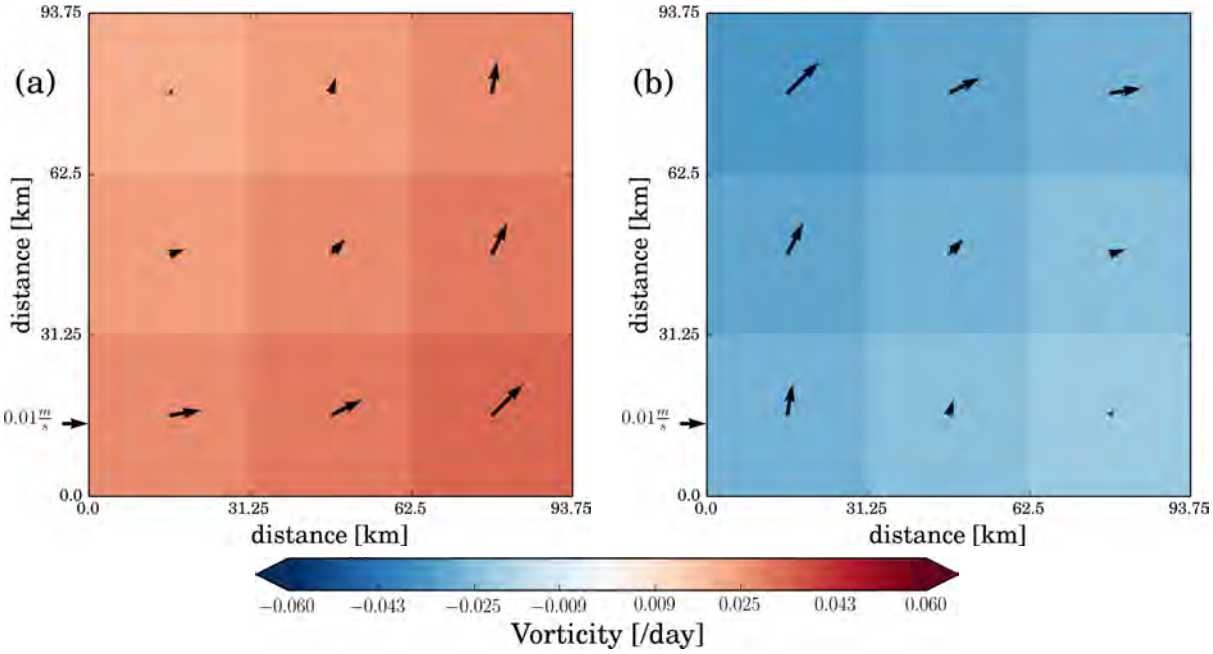

Figure 5.2: Idealized depiction of positive vorticity (**a**) and negative vorticity (**b**) as colored fields. The vectors illustrate idealized sea-ice drift settings. The cell size corresponds to an area of 31.25 km × 31.25 km, identical to the AMSR-E sea-ice drift.

5.3.3 Shear

Shear can be separated into two components: *stretching* and *shearing*. The *stretching* deformation D_1 represents stretching if D_1 is positive and foreshortening (shrinking) if D_1 is negative:

$$D_1 = \frac{\partial u}{\partial x} - \frac{\partial v}{\partial y}. \tag{5.3}$$

The effect of the stretching deformation D_1 is to deform the areal extent of an sea-ice floe only along or perpendicular to the prevailing drift direction through downstream changes in the sea-ice speed and confluence or diffluence (Figure 5.3). Divergence

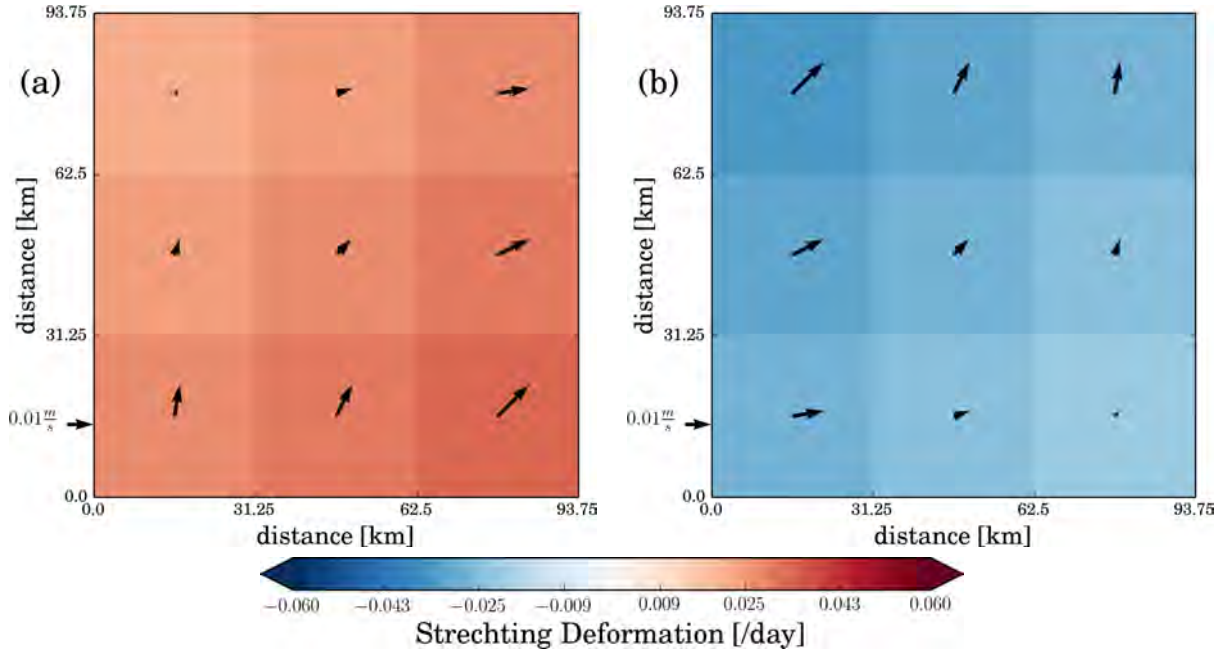

Figure 5.3: Positive stretching deformation (**a**) and negative negative stretching deformation (**b**) depicted as colored fields. The vectors illustrate idealized sea-ice drift settings. The cell size corresponds to an area of 31.25 km × 31.25 km, identical to the AMSR-E sea-ice drift.

also contains the effects of downstream changes in ice speed and confluence and diffluence. However, unlike divergence, stretching deformation is not necessarily very small, because the effects of stretching or shrinking, and confluence or diffluence do not counteract each other, as far as divergence is concerned (Bluestein, 1993).

The second quantity is called *shearing* deformation D_2, because the effect of D_2 alone is to deform the ice parcel at a 45° angle to the flow through the effects of shear and curvature (Figure 5.4):

$$D_2 = \frac{\partial v}{\partial x} + \frac{\partial u}{\partial y}. \tag{5.4}$$

Vorticity also contains the effects of shear and curvature. However, the effects of shear and curvature work in the opposite direction for shearing and deformation. Both, stretching and shearing, have the same effect, but in different directions separated by 45° or 135° (Bluestein, 1993).

A field of pure shear deformation has no vorticity, and the field is not divergent. Unlike divergence and vorticity, shear deformation is not rotationally invariant. That means, measurements of deformation depend upon the orientation of the coordinate system. However, the sum of the squares of each deformation D_1 and D_2 is rotationally invariant (Bluestein, 1993). In nature, a combination of translational, divergent, vortical, and shear ice-flow occurs.

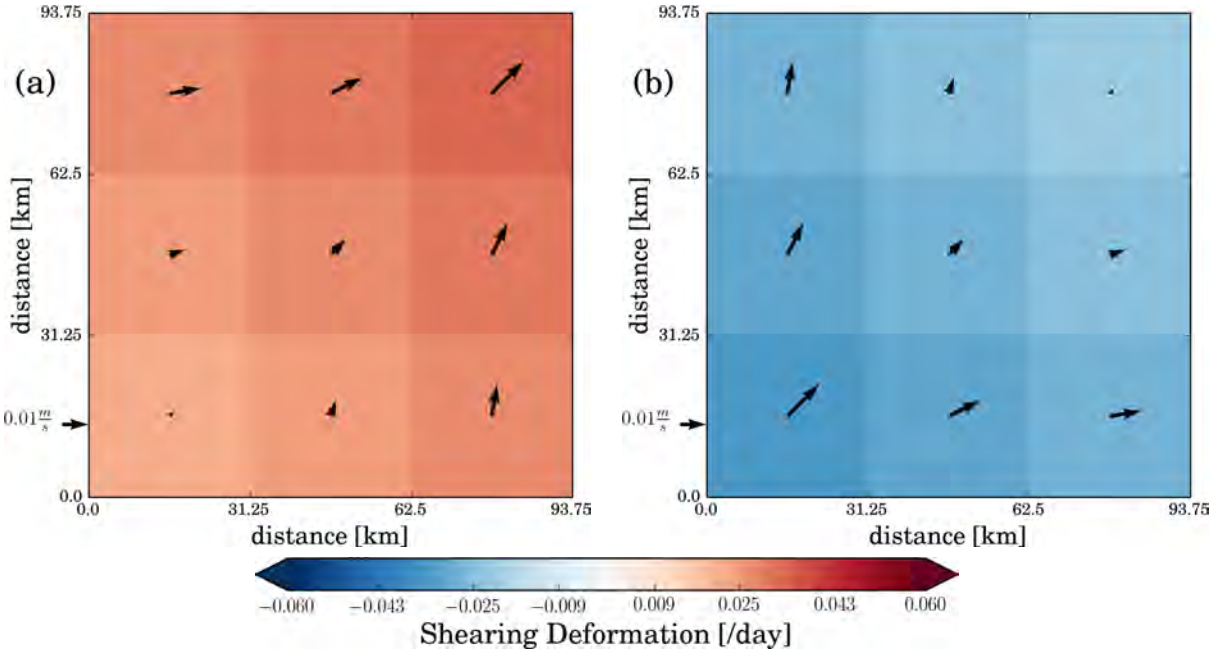

Figure 5.4: Positive shearing deformation (**a**) and negative shearing deformation (**b**) depicted as colored fields. The vectors illustrate idealized sea-ice drift settings. The cell size corresponds to an area of 31.25 km × 31.25 km, identical to the AMSR-E sea-ice drift.

Shear Rate

The shear rate of sea ice can be deduced from the strain tensor (Feltham, 2008):

$$\dot{\epsilon}_{ij} = \begin{pmatrix} \epsilon_x & \frac{1}{2}\gamma_{xy} \\ \frac{1}{2}\gamma_{xy} & \epsilon_y \end{pmatrix} = \begin{pmatrix} \frac{\partial u}{\partial x} & \frac{1}{2}\left(\frac{\partial v}{\partial x} + \frac{\partial u}{\partial y}\right) \\ \frac{1}{2}\left(\frac{\partial v}{\partial x} + \frac{\partial u}{\partial y}\right) & \frac{\partial v}{\partial y} \end{pmatrix} \tag{5.5}$$

with $\epsilon_x = \frac{\partial u}{\partial x}$, $\epsilon_y = \frac{\partial v}{\partial y}$, and $\gamma_{xy} = \frac{\partial u}{\partial y} + \frac{\partial v}{\partial x}$. Adding up the diagonal components of equation (5.5) gives the divergence $\epsilon_d = \epsilon_x + \epsilon_y$ (equation (5.1)). Subtracting the diagonal component ϵ_y from ϵ_x of equation (5.5) gives the stretching deformation $D_1 = \epsilon_x - \epsilon_y$ (equation (5.3)). Adding up the γ_{xy}-components of equation (5.5) gives the shear deformation D_2 (equation (5.4)). Feltham (2008) defines the magnitude of the shear deformation as shear rate:

$$\epsilon_s = \sqrt{D_1^2 + D_2^2} = \sqrt{\left(\frac{\partial u}{\partial x} - \frac{\partial v}{\partial y}\right)^2 + \left(\frac{\partial u}{\partial y} + \frac{\partial v}{\partial x}\right)^2}. \tag{5.6}$$

The shear rate ϵ_s is rotationally invariant (Bluestein, 1993). Miles and Barry (1998) used an equation similar to equation (5.6), but with a negative sign[1] in the first term of equation (5.6). Based on the shear rate ϵ_s, Miles and Barry (1998) calculated the shear orientation angle. The shear orientation angle elegantly links the sea-ice shear orientation to the large-scale lead orientation. Unfortunately, Miles and Barry (1998)

[1]Personal communication with Martin Miles revealed that the negative sign is most probably an error (December 2013).

did not document how the shear orientation angle was derived from the shear rate[2] (equation (5.6)).

Thorndike et al. (1975); Leppäranta (2005); Feltham (2008); Yu et al. (2013) introduced the angle θ as the ratio of shearing rate and divergence. Following these studies, we define the angle θ as

$$\theta = \arctan\left(\frac{\epsilon_d}{\epsilon_s}\right). \tag{5.7}$$

Configurations of $\theta = -\pi/2, 0$, and $\pi/2$ correspond to pure convergence ($\epsilon_s = 0,\ \epsilon_d <$

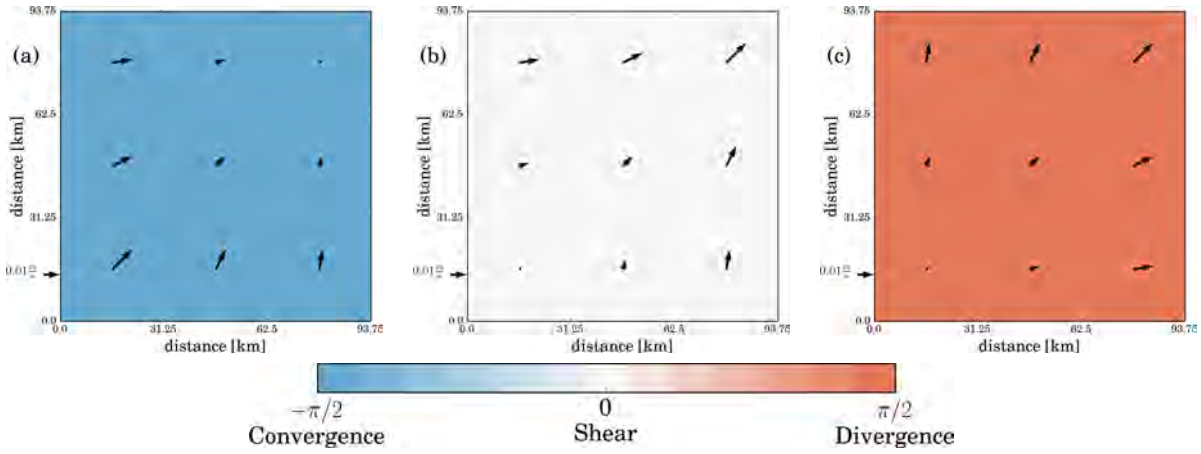

Figure 5.5: Depiction of the angle θ for pure divergence (**a**), shear only (**b**), and pure convergence (**c**) as colored fields. The vectors illustrate idealized sea-ice drift settings from Figure 5.1 for (**a**) and (**c**) and from Figure 5.4a for (**b**). The cell size corresponds to an area of 31.25 km × 31.25 km, identical to the AMSR-E sea-ice drift.

0), pure shear ($\epsilon_s > 0,\ \epsilon_d = 0$), and pure divergence ($\epsilon_s = 0,\ \epsilon_d > 0$), respectively. Figure 5.5 shows the angle θ for the idealized drift settings from Figures 5.1 and 5.4.

We assume that the angle θ (equation (5.7)) is not the angle used by Miles and Barry (1998), because Miles and Barry (1998) refer to the angle that represents the angle of maximum shear between the two principal axes of strain. The angle θ helps to disentangle the influence of divergence and shear on a drift field, but the angle does not correspond to an angle between the principal axes of strain. In the following section, we attempt to derive the shear orientation angle and define the two principal axes of strain.

Derivation of the Shear Orientation Angle

Miles and Barry (1998) defined the shear orientation θ as the angle of maximum shear between the two principal axes of strain. Strain is a concept that is also known in

[2]Personal communication with Martin Miles did not help much. The maps showing the shear orientation in Miles and Barry (1998) were probably provided by Roger Colony, who is retired (December 2013).

engineering. Here, we follow mainly engineering literature (Gross et al. (2007), pp. 70) to derive the shear orientation θ.

The strain ϵ is defined as the change in length ΔL of a body compared to the initial length L:

$$\epsilon = \frac{\Delta L}{L} = \frac{\delta}{L}. \tag{5.8}$$

The normal strain describes the elongation that is assumed to be normal (perpendicular) to the cross-section of a body. The change in length can also be replaced by the total displacement δ. The tensile strain is generally considered positive, the compressive strain negative.

From the strain tensor (equation (5.5)) follows that the strains are defined as $\epsilon_x = \frac{\partial u}{\partial x}$, $\epsilon_y = \frac{\partial v}{\partial y}$, and $\gamma_{xy} = \frac{\partial u}{\partial y} + \frac{\partial v}{\partial x}$. Figure 5.6 shows an infinitesimal reference rectan-

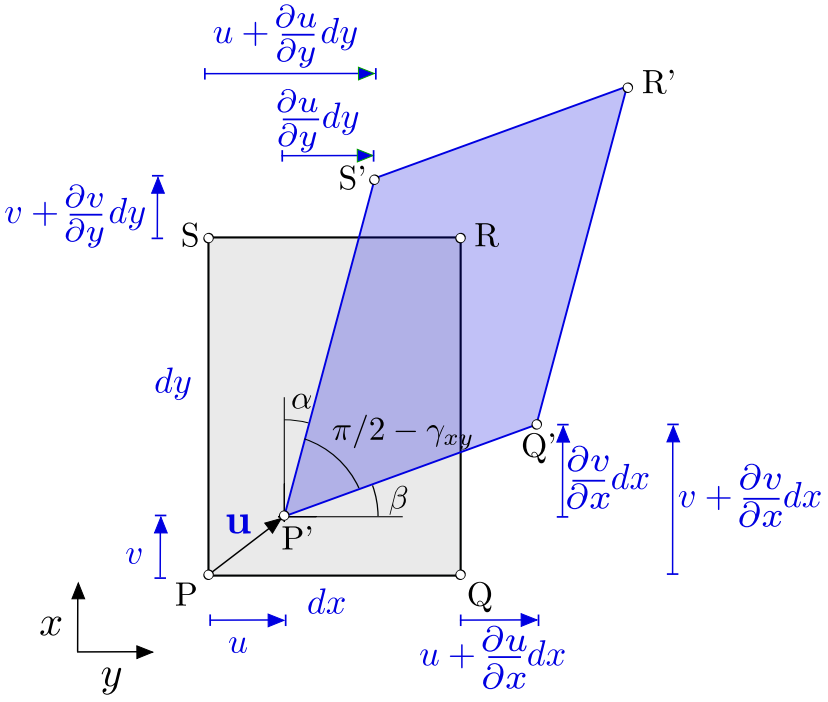

Figure 5.6: Infinitesimal reference rectangle (PQRS) with side length dx and dy. The new state after deformation is (P'Q'R'S'). The displacement vector **u** is defined by the coordinates u and v. Sketch adapted from Gross et al. (2007).

gle (PQRS), which is strained in x-direction and y-direction into a new strain state (P'Q'R'S'). Gross et al. (2007) consider only small deformations, the angles α and β are exaggerated. The strain in x-direction ϵ_x can be constructed by:

$$\epsilon_x = \frac{\overline{P'Q'} - \overline{PQ}}{\overline{PQ}} = \frac{(dx + \frac{\partial u}{\partial x} dx) - dx}{dx} = \frac{\partial u}{\partial x}. \tag{5.9}$$

The strain in y-direction can be constructed in a similar way and is therefore not shown. The change of the originally right angle for the rectangle (PQRS) is given by the angles

α and β. From Figure 5.6 follows:

$$\tan\alpha = \frac{\frac{\partial v}{\partial y}dy}{dy + \frac{\partial v}{\partial y}dy}, \qquad \tan\beta = \frac{\frac{\partial v}{\partial x}dx}{dx + \frac{\partial u}{\partial x}dx}. \tag{5.10}$$

Because we consider only small deformations, we neglect the strain in x-direction and in y-direction ($\epsilon_x, \epsilon_y \ll 1$), which gives: $\alpha \approx \frac{\partial u}{\partial y}, \beta \approx \frac{\partial v}{\partial x}$, and $\gamma_{xy} = \frac{\partial u}{\partial y} + \frac{\partial v}{\partial x} = \alpha + \beta$.

Strains at a point can be rotated to give a new strain state at any orientation of the considered body. The rotation angle θ is assumed to be positive (rotates counterclockwise). The new coordinate system is indicated by x' and y'. We do not show the strain transformation, but the resulting equations for $\epsilon_{x'}$. The detailed derivation is shown in Gross et al. (2007), pp. 47. The rotated y-component of the stress $\epsilon_{y'}$ is similar to $\epsilon_{x'}$ and is therefore not shown. Furthermore, we present the transformed equation of the two-dimensional shear strain $\gamma_{x'y'}$.

$$\epsilon_{x'} = \tfrac{\epsilon_x+\epsilon_y}{2} + \frac{\epsilon_x - \epsilon_y}{2}\cos 2\theta + \frac{\gamma_{xy}}{2}\sin 2\theta \tag{5.11}$$

$$\frac{\gamma_{x'y'}}{2} = -\frac{\epsilon_x + \epsilon_y}{2}\sin 2\theta + \frac{\gamma_{xy}}{2}\cos 2\theta \tag{5.12}$$

In order to find the principal rotation angle θ_p that produces the principal (maximum and minimum) strains, we take the derivative with respect to θ and equate to zero:

$$\frac{\partial \epsilon_{x'}}{\partial \theta} = 0 = -(\epsilon_x - \epsilon_y)\sin 2\theta_p + \gamma_{xy}\cos 2\theta_p. \tag{5.13}$$

With $\epsilon_x = \frac{\partial u}{\partial x}$, $\epsilon_y = \frac{\partial v}{\partial y}$, and $\gamma_{xy} = \frac{\partial u}{\partial y} + \frac{\partial v}{\partial x}$ follows:

$$\theta_p = \frac{1}{2}\arctan\left(\frac{\gamma_{xy}}{\epsilon_x - \epsilon_y}\right) \tag{5.14}$$

$$= \frac{1}{2}\arctan\left(\frac{\partial_y u + \partial_x v}{\partial_x u - \partial_y v}\right) \tag{5.15}$$

If we insert θ_p in equation (5.11) and (5.12), we obtain two principal axes of strain:

$$\epsilon_{1,2} = \frac{\epsilon_x + \epsilon_y}{2} \pm \sqrt{\left(\frac{\epsilon_x - \epsilon_y}{2}\right)^2 + \left(\frac{\gamma_{xy}}{2}\right)^2}. \tag{5.16}$$

The principal axes of strain are perpendicular to each other.

The angle that produces maximum shear strain can be obtained similarly to the angle that produces the principal strains:

$$\frac{\partial \gamma_{x'y'}}{\partial \theta} = 0 = -2(\epsilon_x - \epsilon_y)\cos 2\theta_{max} - 2\gamma_{xy}\sin 2\theta_{max} \tag{5.17}$$

$$\theta_{max} = \frac{1}{2}\arctan\left(-\frac{\epsilon_x - \epsilon_y}{\gamma_{xy}}\right) \tag{5.18}$$

$$= -\frac{1}{2}\arctan\left(\frac{\partial_x u - \partial_y v}{\partial_y u + \partial_x v}\right). \tag{5.19}$$

The principle rotation angle (equation (5.15)) and the maximum shear angle (equation (5.19)) are depicted for one week in Figure 5.8. We are not sure which of the two angles Miles and Barry (1998) might have used. Additionally, the factor $\frac{1}{2}$ in equation (5.15) limits the shear orientations between -45° and 45°. In general, it is also not possible to interpret both angles geometrically like in Figure 5.6. Another option could be to derive the orientation of the axis of elongation or contraction $\overline{P'R'}$, but this has not been done in the course of this study.

5.4 Results

In this section, we compare deformation parameters averaged over the same time slices as the lead distributions in chapter 4. We start with a comparison of AMSR-E based sea-ice drift to RGPS sea-ice drift on the weekly timescale in section 5.4.1. We compare the weekly lead orientation to deformation parameters derived from both sea-ice drift products. Furthermore, we show the shear orientation angles introduced in the previous section. In section 5.4.2, we compare the average sea-ice deformation from 2002 to 2011 to the corresponding average lead occurrence and orientation. Section 5.4.3 follows with a comparison of the monthly nine-year sea-ice deformation to the corresponding lead distributions. In section 5.4.4, we compare examples of monthly mean deformation to corresponding lead distributions. In section 5.4.5, we compare the time series of monthly mean lead orientations to monthly mean deformation parameters in the Beaufort Sea and the Fram Strait. When we calculate the deformation parameters for a certain time slice we always calculate the daily deformation parameter at first and average afterwards over the considered time period.

5.4.1 Comparison of AMSR-E Based Sea-Ice Drift and RGPS Sea-Ice Drift to Lead Occurrence and Orientation

In the first part of this section, we compare the AMSR-E based sea-ice drift to the high-resolution RGPS sea-ice drift from 4 February to 10 February 2007. In the second part, we show the resulting shear angles introduced in the previous section. In the third part, we compare both sea-ice drift products to the weekly mean lead orientation.

Figure 5.7: (Next page.) Figures (**a** - **d**): Large-scale mean sea-ice drift and deformation of the Arctic Ocean sea-ice cover between 4 February and 10 February 2007. The high-resolution sea-ice deformation fields are derived from SAR imagery. Mean vector field (**a**) with superimposed sea level pressure contours (Interval: 4 hPa), divergence (**b**), vorticity (**c**), shear rate (**d**) (Units for (**b** - **d**): [/day]). The grid cell size for the deformation parameters corresponds to an area of approximately 10 km × 10 km. Image taken from Kwok and Sulsky (2010). Figures (**e** - **h**): Large-scale mean sea-ice drift in the Arctic between 4 February and 10 February 2007. Ifremer provides the AMSR-E based 2-day sea-ice drift. Drift direction is indicated by arrows. Speed (Unit: [m/s]) (**e**), divergence (**f**), vorticity (**g**), and shear rate (**h**) (Units for (**f** - **h**): [/day]) are depicted as colored fields. The cell size corresponds to an area of 31.25 km × 31.25 km.

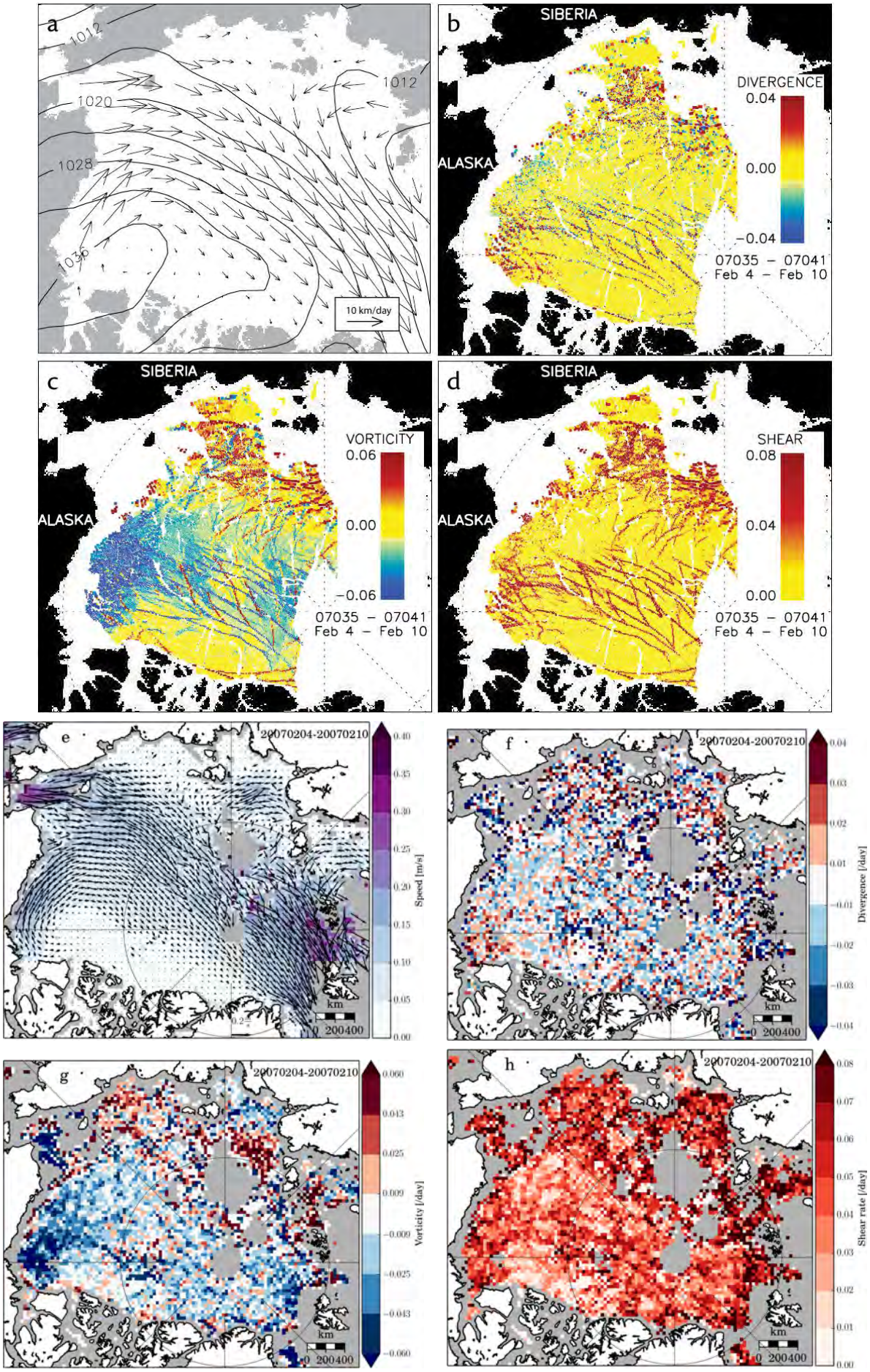

Figure 5.7: (Caption on previous page.)

Figure 5.7a–d shows the high-resolution RGPS sea-ice drift and derived deformation parameters, while Figure 5.7e–h shows the moderate-resolution AMSR-E based sea-ice drift and derived deformation parameters. Leads corresponding to large kinematic features are clearly visible in the RGPS sea-ice deformation parameters. The comparison between both sea-ice drift products reveals that no leads are discernible in the AMSR-E based 2-day sea-ice drift. We observe traces of possible lead structures, but they do not appear in all deformation parameters as opposed to the deformation parameters derived from the RGPS sea-ice drift. North of the Canadian Archipelago, the RGPS deformation parameters are very small except for a few pronounced coastal leads. In contrast, the AMSR-E based sea-ice drift does not resolve the coastal leads. The calculated sea-ice deformation fields appear noisy, and they are not comparably small in magnitude at locations where the RGPS deformation parameters show values close to zero.

Both sea-ice drift products agree with regard to the large-scale sea-ice drift and the overall deformation pattern. For example, the large-scale negative vorticity (anti-clockwise rotation) in the Beaufort Sea is similar for both sea-ice drift products. The order of magnitude agrees also for both products.

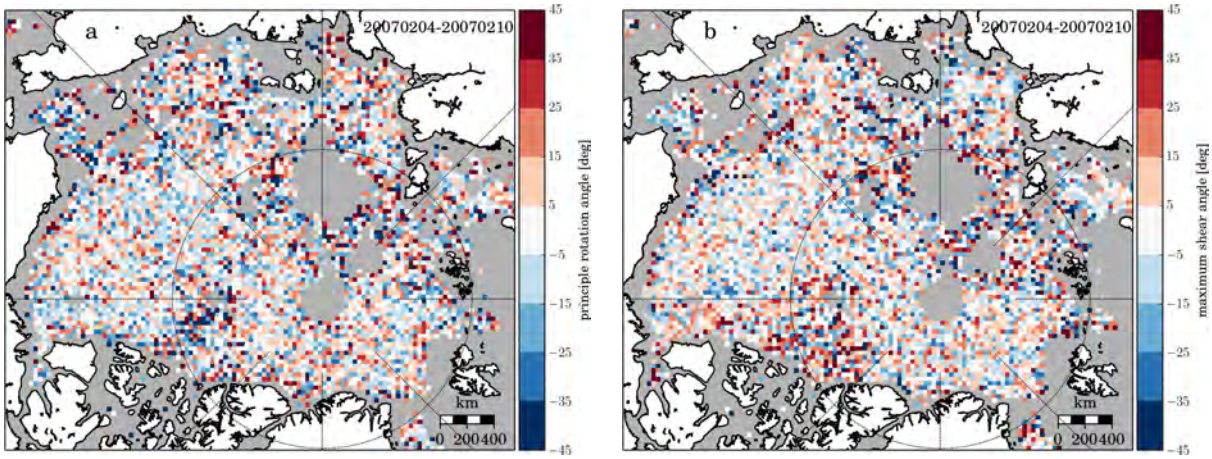

Figure 5.8: Potential shear angles derived from the mean sea-ice drift in the Arctic between 4 February and 10 February 2007. Principal rotation angle (equation (5.15)) (**a**), and angle of maximum shear strain (equation (5.19)) (**b**) are depicted as colored fields (Unit: [°]). Ifremer provides the AMSR-E based 2-day drift. The cell size corresponds to an area of 31.25 km × 31.25 km.

The angles that produce the principal (equation (5.15)) and maximum (equation (5.19)) shear strains are shown in Figure 5.8. We calculate the deformation angle defined in equation (5.7) in the Arctic between 4 February and 10 February 2007 (Figure A.7).

We show the weekly averaged lead orientation and occurrence in Figure 5.9. The lead concentration and orientation of the single days are shown in the Appendix in Figure A.6. In the Central Arctic and in the Beaufort Sea, we observe many leads cells that are orientated parallel to Greenwich meridian. North of Siberia, we observe leads orientated parallel as well as perpendicular to the coast. In the Fram Strait, the prevailing lead orientation is perpendicular to Greenwich meridian.

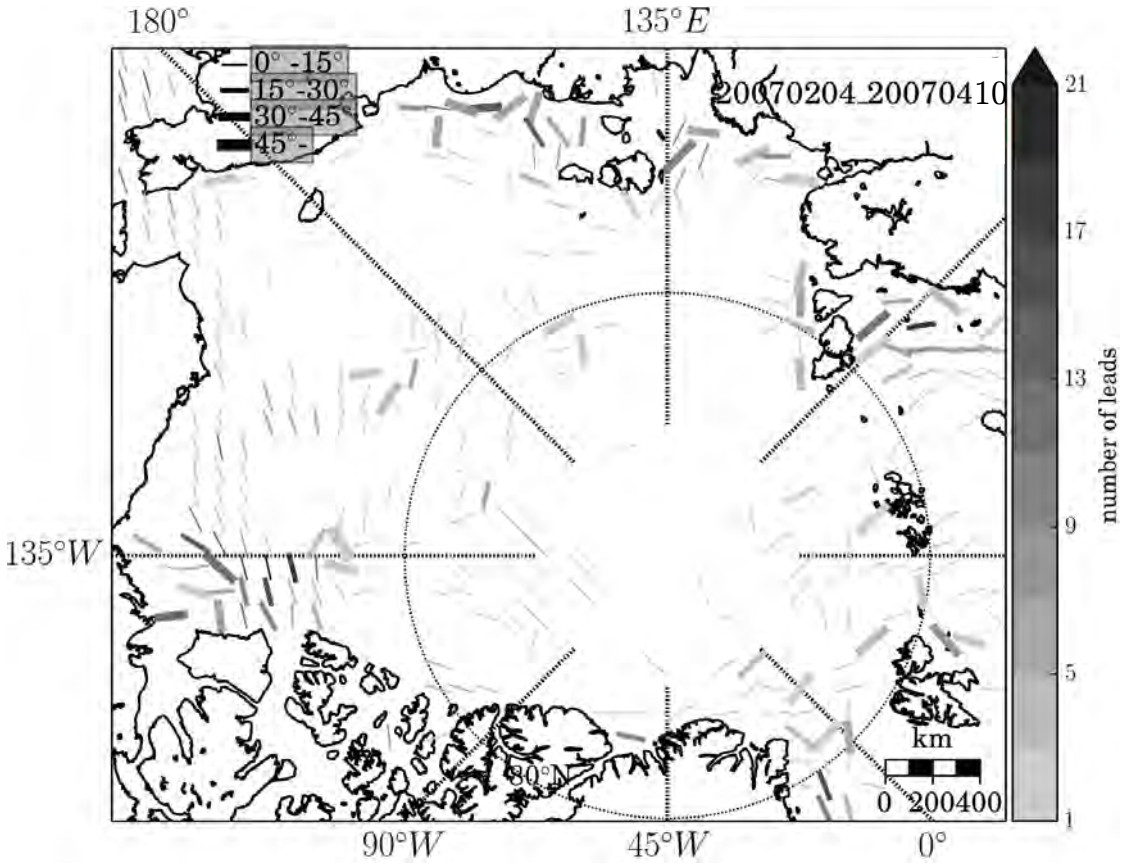

Figure 5.9: Mean lead orientation in the Arctic between 4 February and 10 February 2007. Grey colors depict the number of leads while the width of a lead measures the standard deviation of all lead orientations in a 100 km × 100 km cell.

Especially in the Central Arctic, the orientation of the lead structures in the RGPS sea-ice deformation (Figure 5.7b–d) agrees with the lead orientation in Figure 5.9. In the Beaufort Sea, the peak in lead occurrence (Figure 5.9) corresponds to divergence in both sea-ice drift products (Figure 5.7b and 5.7f). North of the Siberian Sea, maxima of the shear rate in both products (Figure 5.7h and 5.7d) do not coincide with a large number of leads in the same region (Figure 5.9). Instead, many leads occur close to the northern Siberian coastline.

5.4.2 Nine-Year Mean Sea-Ice Deformation

Following the comparison of the AMSR-E based weekly mean sea-ice drift to the weekly RGPS sea-ice drift, we present the mean sea-ice drift averaged for winters from 2002 to 2011 (Figure 5.10). The mean sea-ice drift shows several patterns: Local maxima of sea-ice drift speed located in the Beaufort Sea, the Central Arctic, the Fram Strait, and in the seasonal sea-ice zones. Furthermore, we observe anticyclonic curvature in the Beaufort Sea. The transpolar drift extends from the East Siberian Sea to the Fram Strait exit region (Figure 5.10a). The sea-ice drift is strongly divergent in the Fram Strait exit region and in the seasonal sea-ice zone east of Svalbard (Figure 5.10b). The sea-ice drift is moderately divergent in the Beaufort Sea, Laptev Sea, and east of the

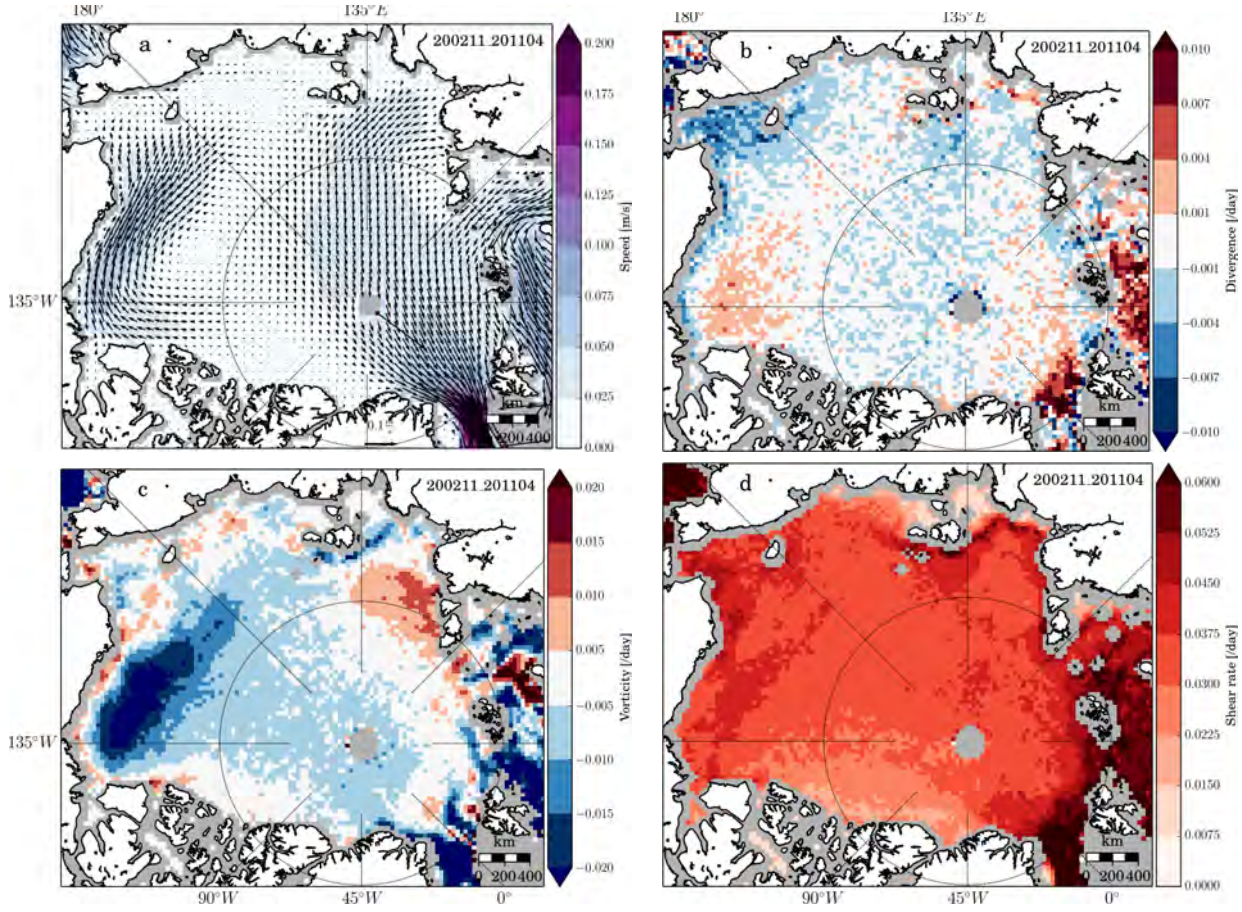

Figure 5.10: Mean sea-ice drift in the Arctic for winters (November to April) between 2002 and 2011. Ifremer provides the AMSR-E based 2-day drift. Drift direction is indicated by arrows. Speed (**a**) (Unit: [m/s]), divergence (**b**), vorticity (**c**), and shear rate (**d**) are depicted as colored fields (Units for (**b** - **d**): [/day]). The cell size corresponds to an area of 31.25 km × 31.25 km.

New Siberian Islands. We observe convergence in the Bering Sea, at the coastline of Alaska, north of the New Siberian Islands, and a few patterns of weak intensity in the Central Arctic. In the remaining Arctic, the sea-ice drift is neither divergent nor convergent. The sea-ice drift exhibits positive vorticity east of Severnaya Zemlya, close to the coast of Alaska, and partly in the Kara and Barents Sea. Negative vorticity, corresponding to anticyclonic (clockwise) rotation, is found more than positive vorticity in the Arctic. We observe maxima of negative vorticity in the Beaufort Sea, west of the New Siberian Islands, the Fram Strait, and in the seasonal sea-ice zones west of Svalbard. The shear rate is largest in the Fram Strait, the seasonal sea-ice zones, and north and west of the New Siberian Islands. Minima are located north of Greenland, the Canadian Archipelago, and Siberia.

When we compare the mean pattern of lead occurrences (Figure 4.1) to the pattern of mean sea-ice drift and derived deformation parameters (Figure 5.10), we observe that everywhere in the Central Arctic where the divergence is large the number of lead occurrences is also larger than in other regions. Exceptions are the seasonal sea-ice zones from south of Svalbard to Franz-Josef Land. The magnitude of divergence

does not linearly coincide with the number of lead occurrences. In the Beaufort Sea with the largest lead occurrence numbers, the divergence is smaller than in the Fram Strait exit region with smaller lead occurrence numbers. North of Siberia and north of Svalbard, we observe more exceptions from the agreement of large divergence and large lead numbers.

The shear rate shows a similar tendency as the divergence: The largest shear rate values do not necessarily coincide with the largest number of lead occurrences. North of Greenland and Siberia, the shear rate is small compared to the rest of the Arctic. However, the patterns of lead orientation and occurrence differ in these regions: Far more leads are located north of Siberia than north of Greenland and north of the Canadian Archipelago. North of Siberia, the lead orientation is not everywhere orientated parallel to the coastline. North of the Canadian Archipelago, a shift in lead orientation from 45° to 90° relative to Greenwich Meridian corresponds to the gradient of shear rate (Figure 5.10d).

There is another interesting feature shown in the map of the shear rate (Figure 5.10d) and in the map of the nine-winter mean lead orientation (Figure 4.1): In the Laptev Sea, a long, curved flaw lead (Martin, 2001) is located between the fast ice and the pack ice.

The vorticity differs from divergence and shear rate, because vorticity contains information directly linked to lead orientation. In the Central Arctic, a vast area with lead orientations $\sim 45°$ spatially correlates with anticyclonic rotation in the Central Arctic (Figure 5.10c). In the Beaufort Sea, the maximum of anticyclonic vorticity is nearly co-located with the maximum in lead occurrence (Figure 4.1).

5.4.3 Monthly Nine-Year Mean Sea-Ice Deformation

In this section, we compare the monthly nine-year mean lead orientation and frequency (Figure 4.2 in chapter 4) to the corresponding sea-ice drift and deformation parameters. We focus on the nine-year monthly-mean maps of November and March, because these months show from a dynamical point of view contrasting setups of the Arctic. In November, we observe larger mean sea-ice drift speeds and a larger magnitude of the sea-ice deformation parameters than in March, when fast-ice regions extend almost into the Central Arctic.

Figure 5.11 contains Arctic-wide maps of the sea-ice drift and from the sea-ice drift derived deformation parameters averaged over all Novembers from 2002 to 2010. The most striking features are the large deformation values extending from the Beaufort Sea to the Bering Sea. Concerning the monthly mean of March from 2003 to 2011, we show only the sea-ice drift and the shear rate (Figure 5.12). Maps showing vorticity and divergence are placed in the Appendix (Figure A.8) because we are not going to refer to them in much detail. In March, all deformation parameters are less pronounced in comparison to the monthly-mean sea-ice deformation of November.

For the November mean, we observe a strong agreement of the location of maximal deformation and largest lead occurrences. This agreement is less distinct in March (and April - not shown). When we look at the overall sea-ice drift pattern in comparison

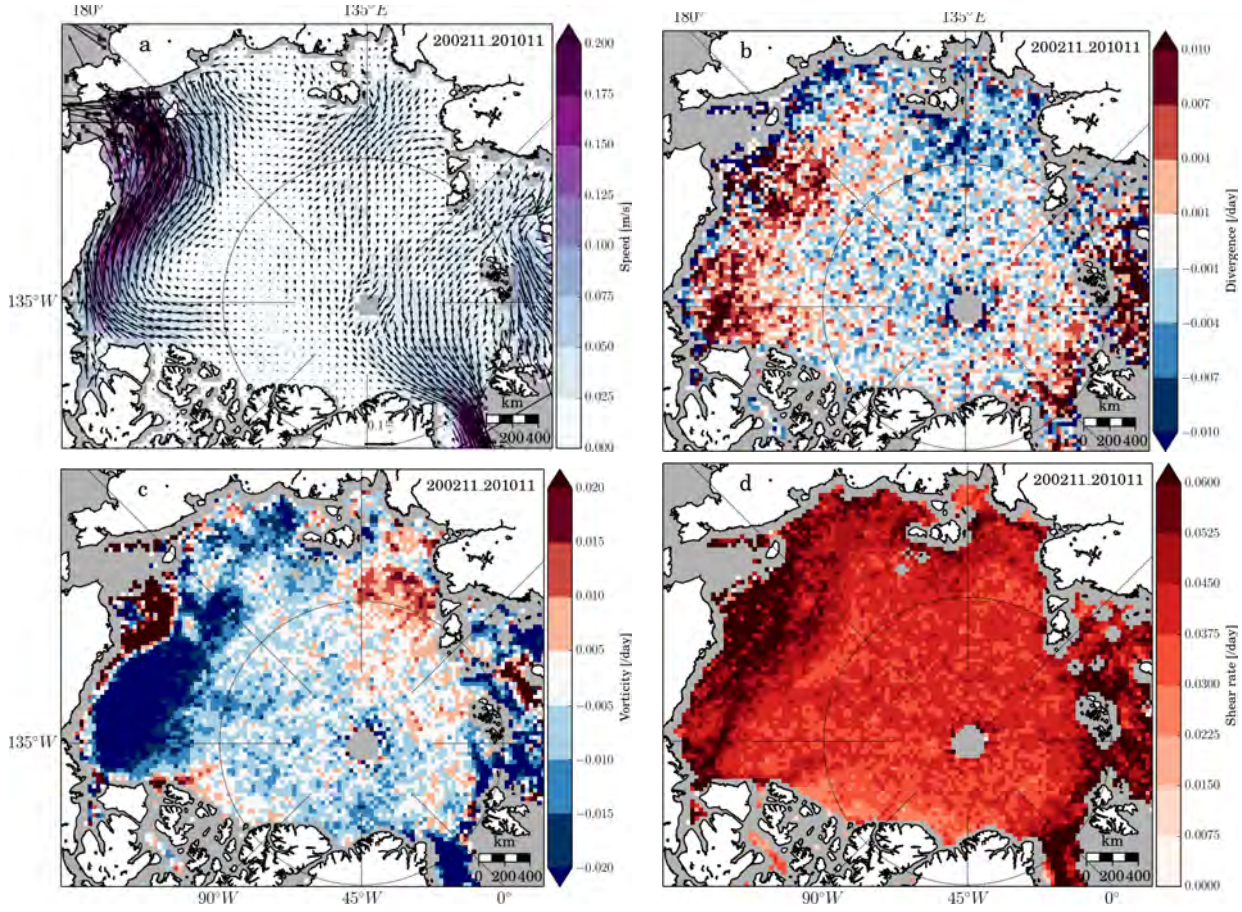

Figure 5.11: Monthly averaged sea-ice drift in the Arctic for November between 2002 and 2010. Ifremer provides the AMSR-E based 2-day drift. Drift direction is indicated by arrows. Speed (**a**) (Unit: [m/s]), divergence (**b**), vorticity (**c**), and shear rate (**d**) are depicted as colored fields (Units for (**b** - **d**): [/day]). The cell size corresponds to an area of 31.25 km × 31.25 km.

to the directional lead pattern, we observe further differences between the months. In November, the mean sea-ice drift direction is orientated parallel to the mean lead orientation. In March, the mean sea-ice drift direction is orientated perpendicular to the mean lead orientation especially in the Central Arctic (Figure 5.12a). The sea-ice drift pattern depicts the transpolar drift while the lead orientation is mostly perpendicular to this route.

Concerning the shear rate, we observe elongated structures in November that arise from linear kinematic features (Figure 5.11d). These traces of linear kinematic features corresponding to leads are similarly orientated to the mean lead orientation, especially in the northern Beaufort Sea. North of Greenland and the Canadian Archipelago, leads are orientated parallel to the coastline throughout the entire season. Interestingly, non-coastal leads are orientated more and more perpendicular to the coast of the Canadian Archipelago and Greenland, when the smallest shear rates occur in March. North of Siberia, leads are almost completely orientated parallel to the coast in March, coinciding with the smallest shear rates in this region. In the Central Arctic, where we observe the smallest amount of lead occurrences in Figure 4.2, the shear rate ranges between

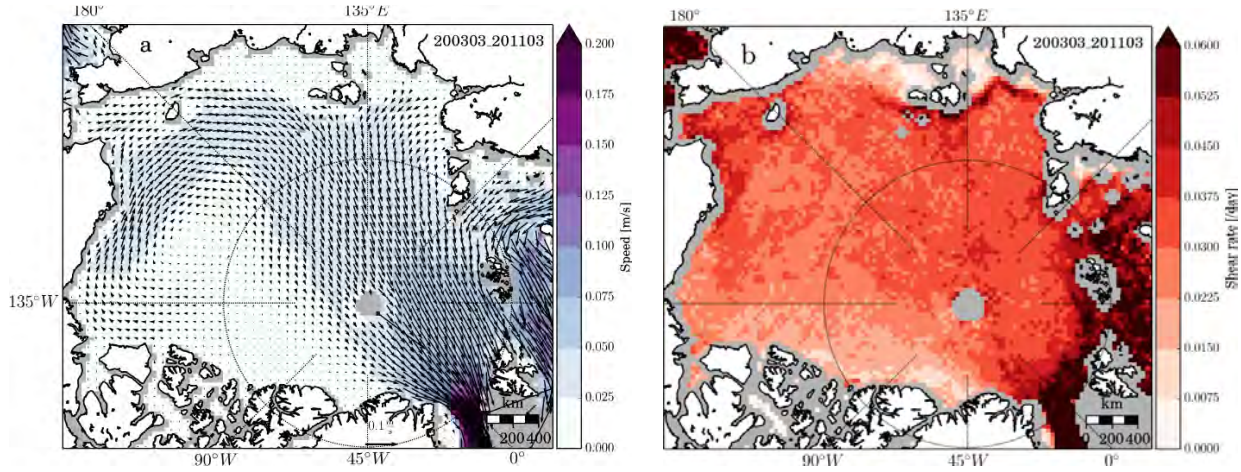

Figure 5.12: Monthly averaged sea-ice drift (**a**) (Unit: [m/s]) and shear rate (**b**) (Unit: [/day]) in the Arctic for March between 2003 and 2011. Drift direction is indicated by arrows. The cell size corresponds to an area of 31.25 km × 31.25 km. The shear rate is derived from Ifremer's AMSR-E based 2-day sea-ice drift.

0.02 /day and 0.04 /day in March (Figure 5.12b). These values are larger compared to the shear rate values of 0.01 /day north of Greenland and Siberia, where a similar or even larger amount of leads occurs. This shows again that lead occurrence and shear rate do not always linearly coincide. Like for the nine-winter mean shear rate (Figure 5.10d), flaw leads build up of in the Laptev sea. The flaw leads visible in the shear rate map (Figure 5.12b) are orientated similar to the flaw leads recognized in Figure 4.2.

5.4.4 Monthly-Mean Sea-Ice Deformation

In this section, we compare the lead orientation maps presented in section 4.2.3 to the corresponding sea-ice deformation. We compared the spatial lead distribution of every single month to the corresponding sea-ice deformation, but due to practical reasons, we describe only November 2002 and February 2005 in more detail. However, we give a short summary about tendencies that one can obtain from a comparison of all monthly averaged lead maps to the corresponding sea-ice deformation maps.

Figure 5.13 shows the mean sea-ice drift and derived deformation parameters in the Arctic for November 2002. In the western Arctic, the sea-ice rotates counterclockwise with the center of rotation placed in the north of the New Siberian Islands (Figure 5.13a). Accordingly, we observe strong negative vorticity accompanied by a strong divergence and shear rate in the same region (Figure 5.13c). In the deformation maps, we can identify long, rectilinear, and line-like shapes of maximal deformation (Figure 5.13b–d). These lines are orientated from the Beaufort Sea into the East Siberian Sea. They show nearly the same orientation as the mean lead orientation in the same region (Figure 4.3). Furthermore, the number of leads in the Beaufort Sea is also larger compared to the Central Arctic. When we compare Figure 4.3 with Figure 5.13a, we observe that the mean sea-ice drift is orientated perpendicular to the mean lead orientation in the western Beaufort Sea but not in the Central Arctic.

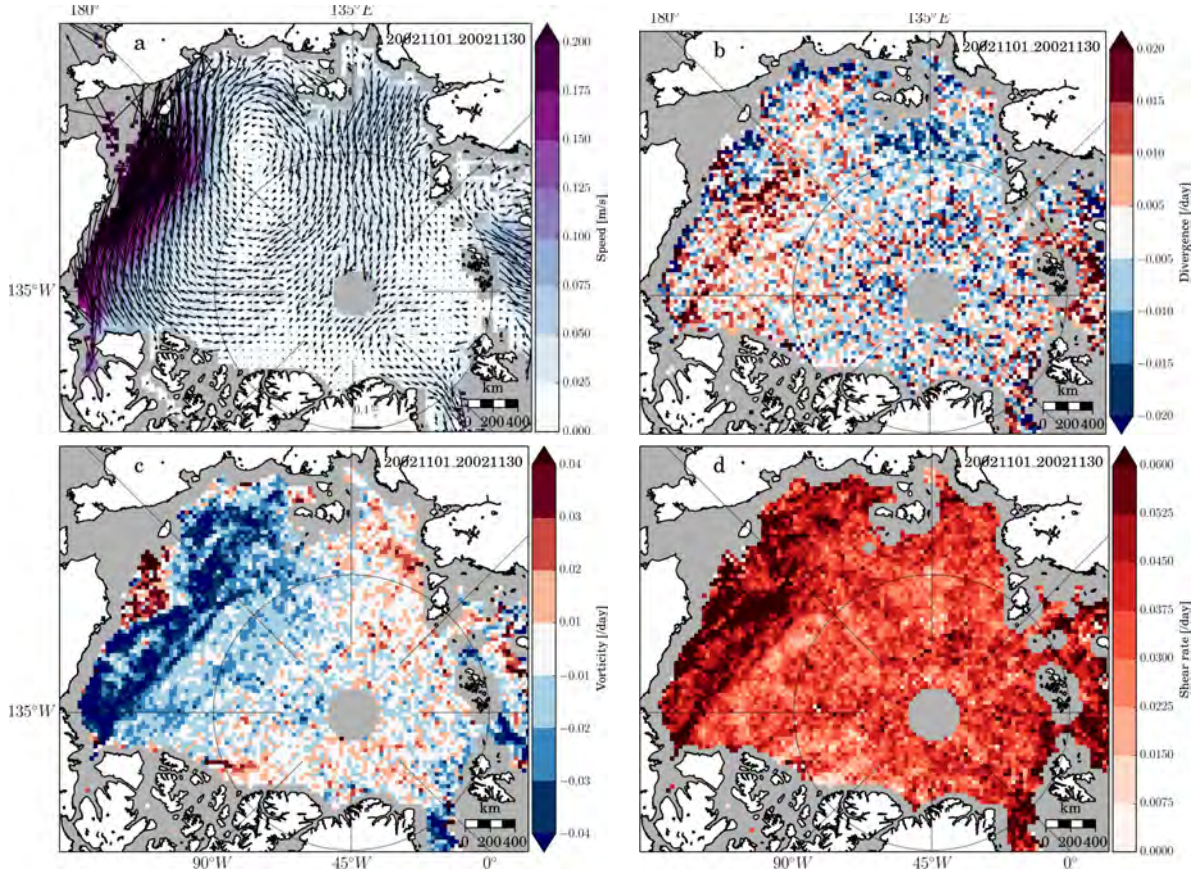

Figure 5.13: Mean sea-ice drift in the Arctic for November 2002. Ifremer provides a AMSR-E based 2-day drift. Drift direction is indicated by arrows. Speed (**a**) (Unit: [m/s]), divergence (**b**), vorticity (**c**), and shear rate (**d**) are depicted as colored fields (Units for (**b** - **d**): [/day]). The cell size corresponds to an area of 31.25 km × 31.25 km.

February 2005 represents a month in mid winter (Figure 5.14), when sea ice does not drift as freely as in November due to the freeze-up of the Arctic. Consequently, the deformation fields are overall weaker in magnitude. We observe in Figure 5.14 again a pronounced gradient in sea-ice drift in the Western Arctic. Similar to November 2002, the pattern extends in a rectilinear shape from the Beaufort Sea to the New Siberian Islands. The corresponding leads in Figure 4.3 are similarly orientated. Otherwise, the largest lead numbers do not occur in this region. Large leads numbers occur in the southern Beaufort Sea and north of Siberia. North of Siberia, all sea-ice deformation parameters show a dividing line between the fast ice and the pack ice. Monthly averaged leads are orientated parallel to this dividing line (Figure 4.3c–d). In most parts of the Central Arctic, the monthly mean sea-ice drift is orientated perpendicular to the monthly-mean lead orientation.

In the remaining months, one can observe a lot of specific patterns in the sea-ice deformation maps and the corresponding lead orientation maps. Here, we list a few patterns that reoccur in a lot of months. The first very pronounced feature is that strong divergence (< 0.015 /day) often coexists with a large number of lead occurrences. The cases are very rare for which large divergence does not agree with a large number

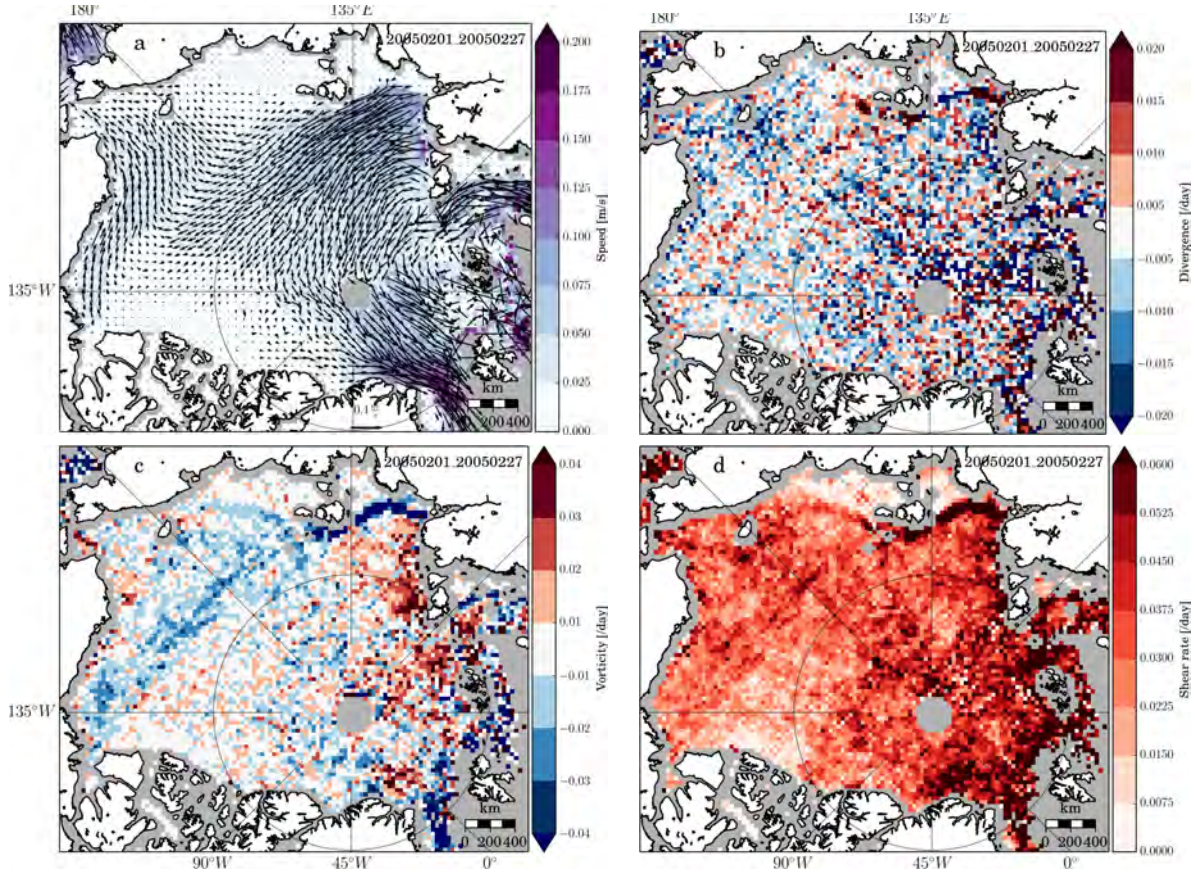

Figure 5.14: Mean sea-ice drift in the Arctic for February 2005. Ifremer provides a AMSR-E based 2-day drift. Drift direction is indicated by arrows. Speed (**a**) (Unit: [m/s]), divergence (**b**), vorticity (**c**), and shear rate (**d**) are depicted as colored fields (Units for (**b** - **d**): [/day]). The cell size corresponds to an area of 31.25 km × 31.25 km.

lead occurrences. Furthermore, large lead occurrences often coincide with pronounced anticyclonic vorticity (clockwise rotation) in the Beaufort Sea. Only a few leads occur north of Greenland from February to April. This agrees with very small shear rates in the same region. Generally, we observe a pronounced difference in the intensity of lead occurrence and sea-ice deformation between the first (NDJ) half and the second (FMA) half of a winter season.

In a lot of months, monthly-averaged leads are orientated perpendicular to the mean sea-ice drift direction. In the Kara Sea and Laptev Sea, leads are usually orientated parallel to the major axis of the shear rate (for the Kara Sea *cf.* for example Figure 5.14d). Concerning the fast ice north of Siberia, the transition zone between the fast ice and the drifting pack ice is usually depicted in the lead-orientation maps.

5.4.5 Time Series of Sea-Ice Deformation Compared to Lead Orientation

In this section, we compare a time series of monthly-mean lead orientation (Figure 4.4 in chapter 4) to the corresponding monthly-mean sea-ice deformation. Figure 5.15

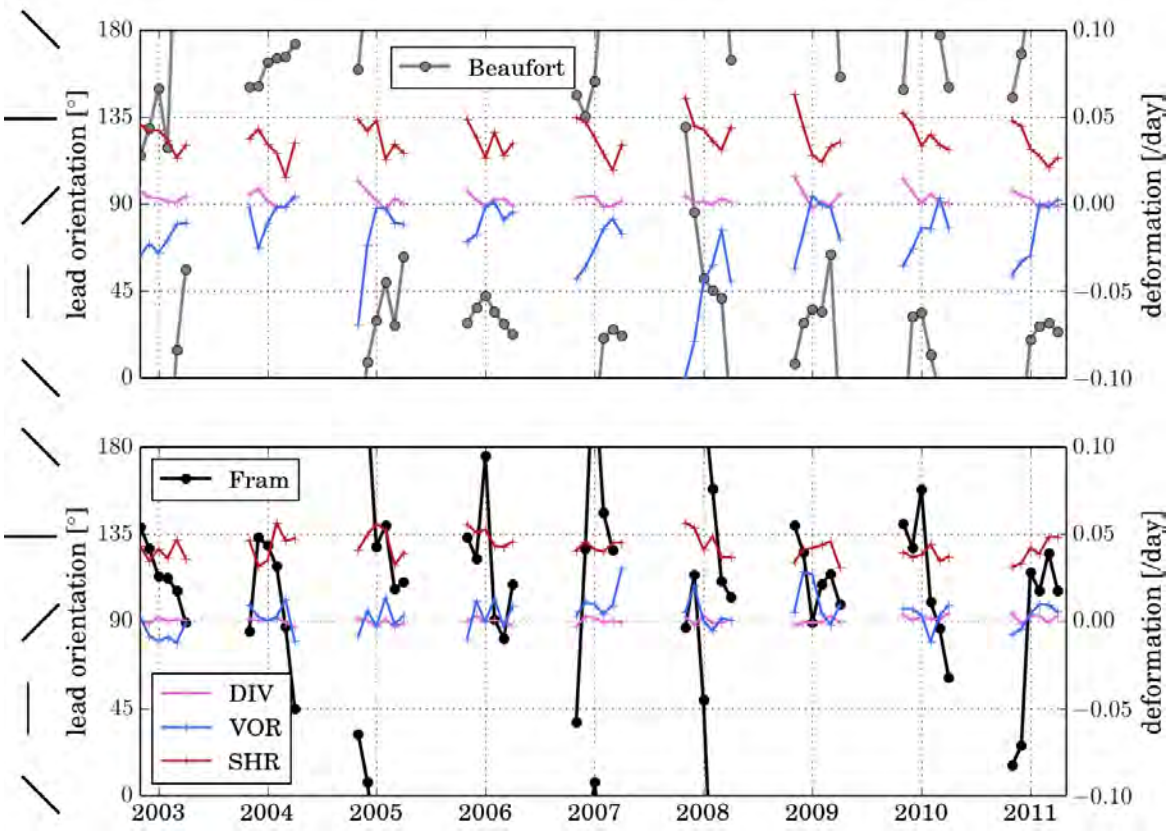

Figure 5.15: Time series of monthly-mean lead orientation and sea-ice deformation parameters in sub regions of the Beaufort Sea (black line) and the Fram Strait (gray line) from 2002 to 2011. Both, 0° and 180°, are orientated parallel to Greenwich meridian. The lines on the left hand side illustrate the corresponding lead orientation (Unit: [°]). The sea-ice deformation parameters consist of divergence [DIV], vorticity [VOR], and shear [SHR] (Unit: [/day]). The precise location of the two sub regions is indicated by boxes in Figure 4.1.

shows the mean lead orientation in the Beaufort Sea (grey circles) and the Fram Strait (black circles) for winters from 2002 to 2011. The lead orientation is illustrated by the line orientation on the left hand side of Figure 5.15. Monthly-mean values of divergence [DIV], vorticity [VOR], and shear [SHR] are each illustrated by colored crosses.

In the Beaufort Sea, the deformation of sea-ice becomes largest in the beginning of winter in November and December. On average, the magnitude of all sea-ice deformation parameters declines with ongoing winter until March and rises slightly in April. On average, leads are orientated around 135° with reference to Greenwich meridian in the beginning of a season and tilt clockwise to 45°. We observe some exceptions from this mean trend in lead orientation. The most striking exception occurs in the 2007/2008 winter, when the monthly-mean lead orientation tilts counterclockwise from 135° to 180° with respect to Greenwich meridian. In this season, negative vorticity is largest. Other exceptions occur in the 2003/04 and 2005/06 winters. In these winters, the monthly-mean lead orientation is relative persistent compared to other winters. The persistency of the monthly-mean lead orientation coincides with slightly smaller than usual monthly-mean values of divergence and shear rate and with the smallest values of negative vorticity.

In the Fram Strait, monthly-mean sea-ice deformation becomes largest in the end of winter rather than in the beginning of winter. Throughout all months, divergence is very close to zero. The directional change in lead orientation often corresponds to the directional change in vorticity although the magnitude of the vorticity is strongly reduced in comparison to the Beaufort Sea. In the beginning of the 2009/10 winter, counterclockwise tilting of the mean lead orientation coincides with an increase in positive vorticity (counterclockwise rotation). From January to March, the mean lead orientation tilts clockwise and positive vorticity decreases indicating less pronounced counterclockwise rotation of sea ice. From March to April, the mean lead orientation tilts counterclockwise and positive vorticity increases indicating stronger counterclockwise rotation of the sea ice. In other winters, we often observe a local accordance between the change of monthly-mean lead orientation and monthly-mean vorticity. Again in the 2007/08 winter, the most striking exception occurs. The monthly-mean lead orientation strongly tilts counterclockwise, while the monthly-mean vorticity only slightly changes from positive to negative vorticity indicating only a slight change from counterclockwise to clockwise rotation.

5.5 Discussion

In this section, we discuss the major results from the comparison of the lead orientation maps to the sea-ice deformation on various time scales. In section 5.5.3, we discuss the relationship of large-scale vorticity and monthly-mean lead orientation with focus on the Beaufort Sea for the years 2002 to 2011.

5.5.1 Comparison of Weekly Sea-Ice Deformation and Leads

In section 5.4.1, we compared the weekly-mean AMSR-E based sea-ice drift to the weekly-mean RGPS sea-ice drift. Furthermore, we compared both sea-ice drift products to the corresponding map of the weekly lead orientation. The AMSR-E sea-ice drift has the disadvantage of a limited spatial resolution (cell size of 31.25 km $\times$ 31.25 km) that is much larger than the width of a typical lead (3 km to 10 km) resolved in the lead concentration maps (Figure 5.7e–h, A.6, and 5.9). Contrarily, lead structures are resolved in Figure 5.7b–d because of the sufficient spatial resolution (cell size of 10 km $\times$ 10 km) of the RGPS sea-ice drift. On the weekly or daily time scale, the comparison of leads and especially their orientation to the deformation of sea ice requires a high-resolution sea-ice drift.

Marsan et al. (2004) found that sea-ice deformation occurs localized at leads. Furthermore, the mean deformation of sea ice is related to the spatial scale according to a power law with an exponent of -0.2 (Marsan et al., 2004). This implies that sea-ice deformation should be slightly larger for a sea-ice drift product with a grid cell size of 10 km $\times$ 10 km than a sea-ice drift product with a grid cell size of 30 km $\times$ 30 km. We did not apply the scaling law proposed by Marsan et al. (2004) to any of the two sea-ice drift products. From a visual comparison of the two sea-ice drift products, we cannot

tell if scale dependence plays an important role. Certainly, scale dependence of sea-ice deformation adds an uncertainty to the comparison of both sea-ice drift products.

A weakness of the RGPS sea-ice drift is that the Fram Strait is not covered. An Arctic-wide comparison of this region matters, because most of the sea-ice drift export takes place through the Fram Strait (Spreen et al., 2009). As a side note, Heygster et al. (2012) show a high-resolution sea-ice drift and deformation map derived from Environmental Satellite (Envisat) Advanced Synthetic Aperture Radar (ASAR) scenes in the Fram Strait between 15 and 16 March 2010. A visual comparison shows a good spatial agreement between the high-resolution sea-ice deformation (Figure 10a in Heygster et al. (2012)) and the lead concentration and derived lead orientation patterns.

Concerning the derivation of the shear angle between the two principal axes of strain (Miles and Barry, 1998), we cannot tell which of the angles introduced in section 5.3.3 is accurate. Equation 5.7 is a useful tool to disentangle divergence, shear, and convergence, but equation 5.7 does not define the angle between the two principal axes of strain. Beside the difficult geometrical interpretation of equations 5.15 and 5.19, they are both limited between -45° and 45°. Given all these uncertainties, we did not analyze these angles in this comparison between leads and sea-ice deformation.

5.5.2 Comparison of Sea-Ice Deformation and Leads for a Nine-Year Climatology

On all analyzed time-scales, the rates of divergence and shear rate agree with the number of lead occurrences. However, this relationship is not exactly linear. A region of high divergence rate does not have to be co-located with a large number of lead occurrences in the same region. Large lead occurrences do also not always coincide with the highest divergence rate in a lead distribution map. Furthermore, the agreement of divergence and lead occurrences is more developed in the beginning of a season (November and December) than in the end of season (March and April).

North of Siberia, we observe a lot of leads and polynyas in the lead orientation maps and in the sea-ice deformation maps. The lead orientation as well as the deformation maps show the opening of flaw leads at the border between the fast ice and the drifting pack ice. The orientation of these openings is consistent with the orientation of flaw leads mapped by Martin (2001), pp. 540. The matching orientation of flaw lead with the orientation of the flaw lead visible in the shear rate is a benchmark of the algorithm to infer the lead orientation.

5.5.3 Comparison of the Directional Change of Lead Orientation and Vorticity

In section 5.4.5, we compare the time series of lead orientation to the time series of deformation parameters derived from the AMSR-E based sea-ice drift. In this section, we focus on the vorticity, because vorticity contains the rotational information of the

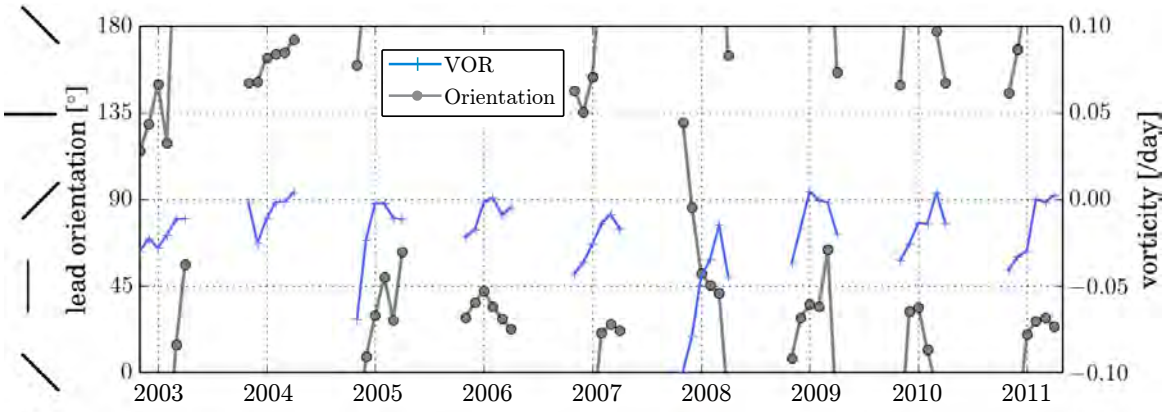

Figure 5.16: Time series of monthly-mean lead orientations (grey line) and from the sea-ice drift derived vorticity [VOR] (blue line) in the Beaufort Sea from 2002 to 2011. Both, 0° and 180°, are orientated parallel to Greenwich meridian. The lines on the left hand side illustrate the corresponding lead orientation. The precise location of the sub region in the Beaufort Sea is indicated by a box in Figure 4.1.

sea-ice drift that is linked to the change in sea-ice drift direction. In Figure 5.16, we compare the monthly-mean vorticity to the monthly-mean lead orientation in a sub region of the Beaufort Sea. The location of the sub region is marked by a box in Figure 4.1. In order to focus only on the vorticity, we do not show divergence and shear rate as in Figure 5.15.

The directional change of the monthly-mean lead orientation is linked to directional tendency of the vorticity (Figure 5.15 in section 5.4.5). For example, if we observe strong positive vorticity (anti-clockwise rotation) in two consecutive months we likely observe that the mean lead orientation tilts anti-clockwise in between the two months. This tendency is stronger pronounced in the Beaufort Sea than in the Fram Strait. This makes sense given that the magnitude of the vorticity is 2 to 3 times larger in the Beaufort Sea than in the Fram Strait. The tendency appears basically in all winters except for the 2007/08 winter.

This winter shows the opposite tendency. In the Beaufort Sea, the mean lead orientation tilts counterclockwise paired with a strong negative vorticity implying clockwise rotation of the sea ice. For the remaining eight winters, the mean lead orientation follows to tilt in the same direction as the mean sea-ice drift. We do not know why the tendency is reverted in the 2007/08 winter. We suspect the until that time unprecedented minimum in satellite-observed sea-ice extent in fall 2007 and the strong atmospheric high pressure system (induces clockwise rotation on the sea ice) triggered an inverted tilting tendency.

The agreement of the vorticity and the change in lead orientation might depend on the lifetime of a lead. We observed one lead that remained open at least for one month (section 2.3.3), and we have observed the same leads on consecutive days. However, we do not know the ratio of opening leads to closing leads on the monthly time scale. In the 2007/08 winter, more leads than usual might have opened in a direction opposed to the overall tilting tendency of already existing leads. This could have added to a reversed tendency.

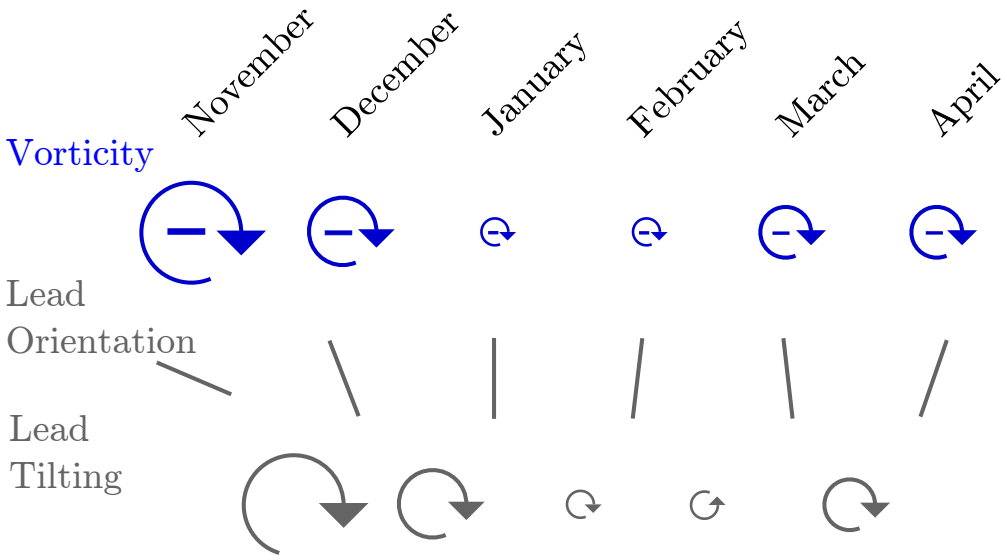

Figure 5.17: Sketch showing the large-scale monthly-mean vorticity (blue) steering the change of monthly-mean lead orientation (grey). The sketch depicts in a slightly simplified the 2005/06 winter in the Beaufort Sea.

Figure 5.17 shows a sketch that depicts the 2005/06 winter. The underlying mechanism is also valid for other winters of the time series except for the 2007/08 winter. In November and December, when the vorticity is intense the monthly-mean lead orientation tilts stronger in the rotational direction of the vorticity. In January and February, when the vorticity is near zero, the change in lead orientation is weak and arbitrary. In March and April, when the vorticity intensifies again, the lead orientation tilts in the direction induced by the vorticity.

Chapter 6

Conclusions

The aim of this thesis is to analyze leads via passive microwave remote sensing. In order to detect leads, we apply the lead-detecting algorithm of Röhrs et al. (2012) on brightness temperatures measured by the Advanced Microwave Scanning Radiometer for Earth Observing System (AMSR-E). Concerning the accuracy of the algorithm, the resulting lead concentration correctly resolves large leads of at least 3 km in width in comparison to Advanced Synthetic Aperture Radar (ASAR) and CryoSat-2 measurements. Uncertainties of the algorithm arise from atmospheric attenuation of brightness temperatures, especially at the 89 GHz channel, from the presence of snow, and from a vertical temperature gradient within the ice and snow. Furthermore, the two-channel algorithm is more feasible than a potential single-channel algorithm, because the latter requires measurements of the effective emitting surface temperature, which is difficult to measure.

In order to automatically infer the orientation of leads, we develop an algorithm to detect the orientation of quasi-linear lead structures in lead concentration maps. The probabilistic progressive Hough transform together with a clustering algorithm is capable of dealing with quasi-linear line input. The resulting algorithm reliably determines the positions and orientations of large leads. Given the rather coarse resolution of the AMSR-E data, the algorithm is not applicable for detecting the lead length, but for detecting the lead frequency and orientation.

In order to assess the quality of automatically derived lead orientations, we compare them with manually derived lead orientations. Even though the algorithm does not detect every lead, the algorithm infers the mean lead orientation and a similar spatial frequency distribution of lead orientations compared to manually obtained lead orientations. An extensive validation of detected lead orientations with ASAR scenes reveals a good agreement for large leads. Thus, the algorithm is suitable for deriving the lead orientation and frequency from lead concentration maps.

Applying this algorithm to AMSR-E based lead concentration for a period from 2002 to 2011, we find that leads are spatially not equally distributed in the Arctic. Maxima of lead occurrence are located in the Beaufort Sea, the Fram Strait, and north of Siberia. The spatial distribution of lead orientation is coherent over large distances. Leads are on average orientated parallel to their neighboring leads. On the monthly timescale,

the lead orientation varies regionally more strongly than on the yearly or multi-yearly timescale. Over the course of the winter, the frequency of lead occurrences decreases and lead orientation changes. This indicates a seasonal cycle of lead frequency and orientation.

Lead orientations induce anisotropy in the mean spatial distribution of leads in winters from 2002 to 2011. A statistically significant non-random distribution of lead orientations prevails in most regions of the Arctic. This indicates that rheologies of Arctic-wide or global-scale models should describe sea ice anisotropic rather than isotropic.

Based on a comparison of nine-year climatologies of leads and sea-ice deformation, we find that divergence and shear rate are co-located with lead occurrences in the inner Arctic. However, divergence and shear rate do not relate linearly to lead occurrences. For example, the largest divergence values do not necessarily coincide with the largest number of leads in the same location. Concerning the seasonal cycles of lead occurrence and sea-ice deformation, both quantities are stronger in the beginning than in the end of winter. Our results immediately suggest that the change of monthly-mean lead orientation between two consecutive months is steered by the intensity and rotational direction of the monthly-mean sea-ice drift vorticity.

Appendices

A.1 Multi-Sensor Case Study

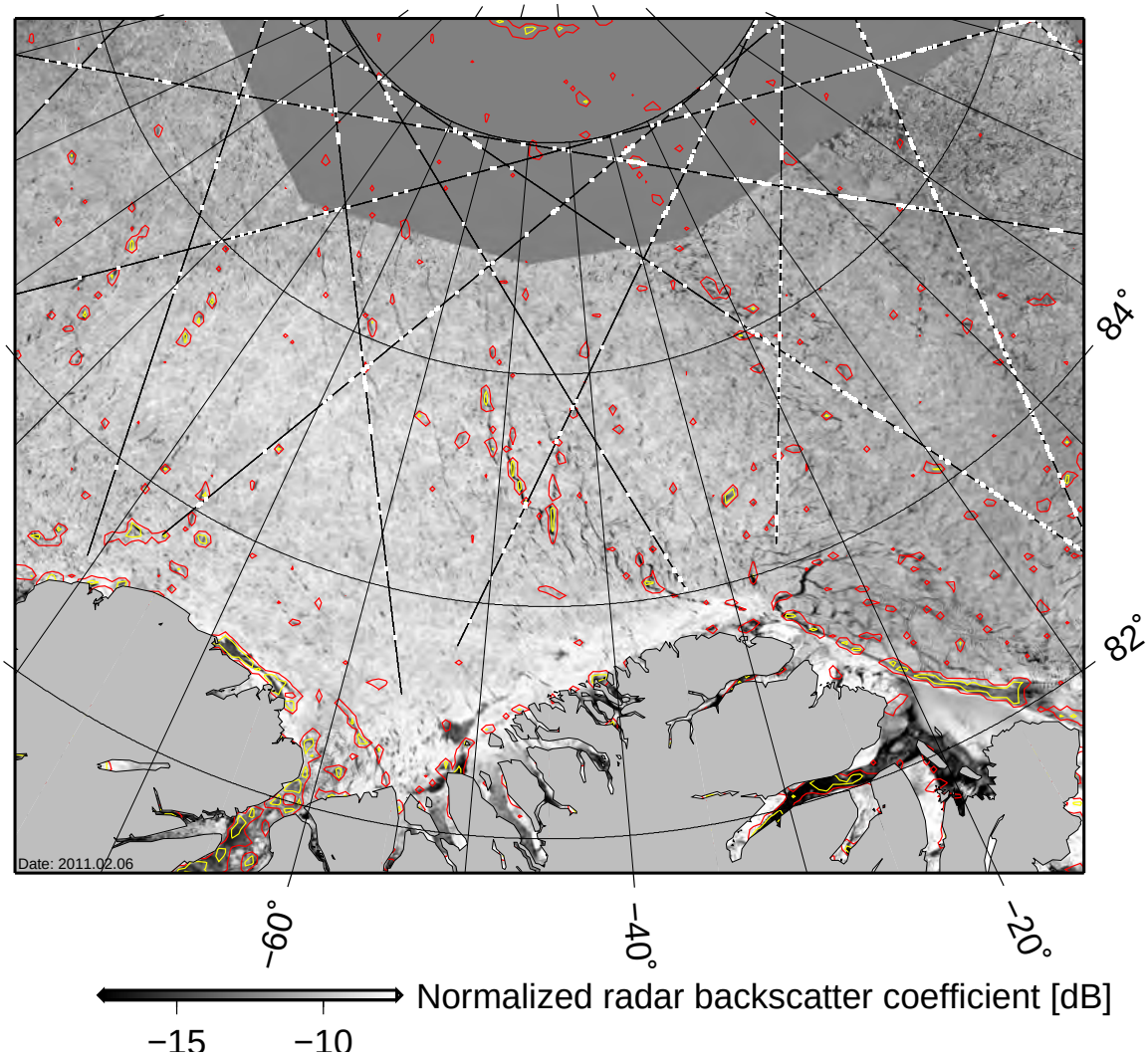

Figure A.1: Multi-sensor comparison: Composite of ASAR scenes depicted as normalized radar backscatter coefficient [dB], AMSR-E LC [%] (red isoline - 25 %, yellow isoline - 75 %), and lead positions from CryoSat-2 (white dots on top of the black CryoSat-2 track) north of Greenland on 6 February 2011.

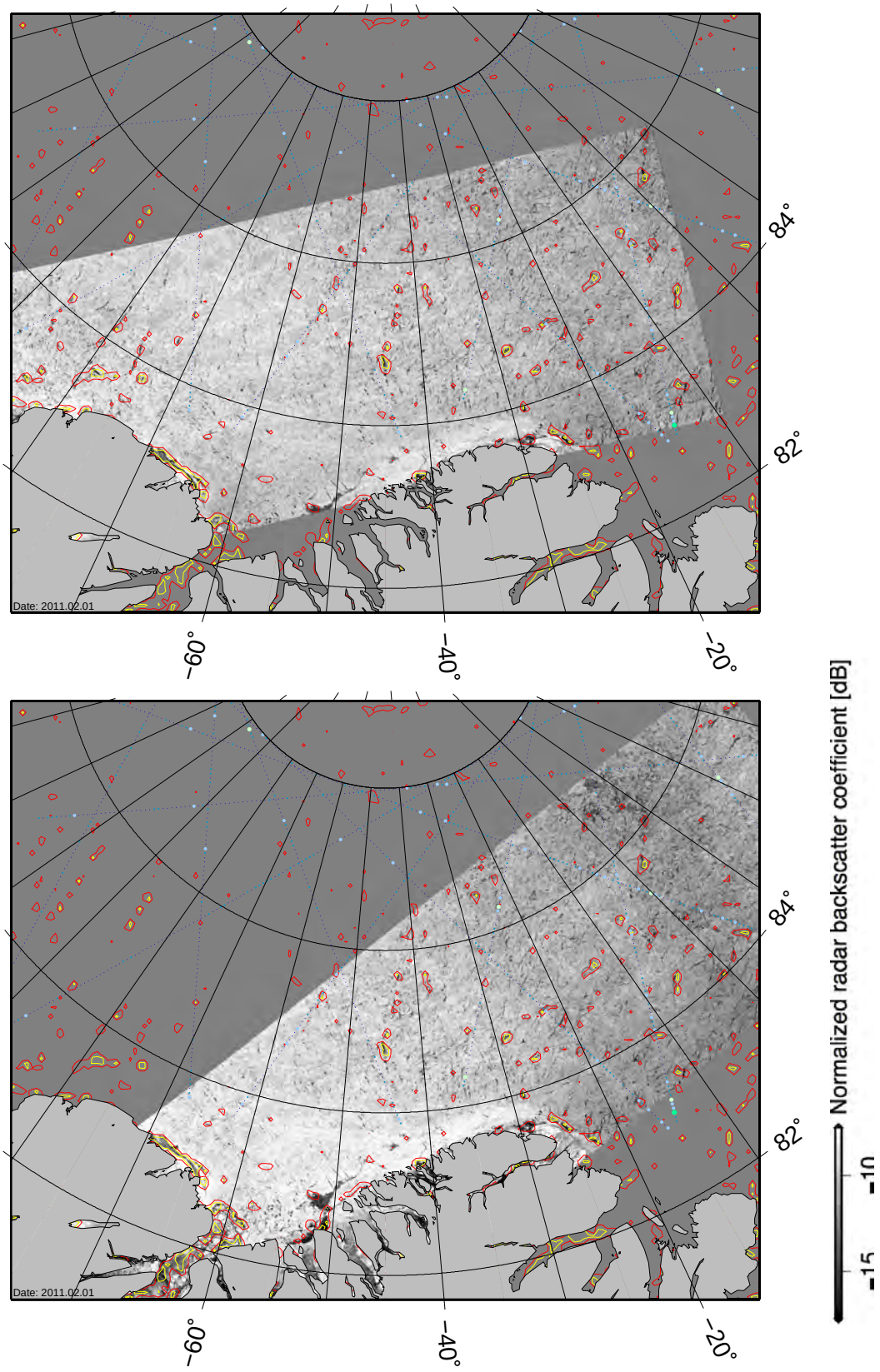

Figure A.2: Multi-sensor comparison: Two single ASAR scenes depicted as normalized radar backscatter coefficient [dB], AMSR-E LC [%] (red isoline - 25 %, yellow isoline - 75 %), and lead positions from CryoSat-2 (dark blue - no leads, light blue - a few lead detections, greenish colors - only leads within a sample of 20 measurements) north of Greenland on 1 February 2011.

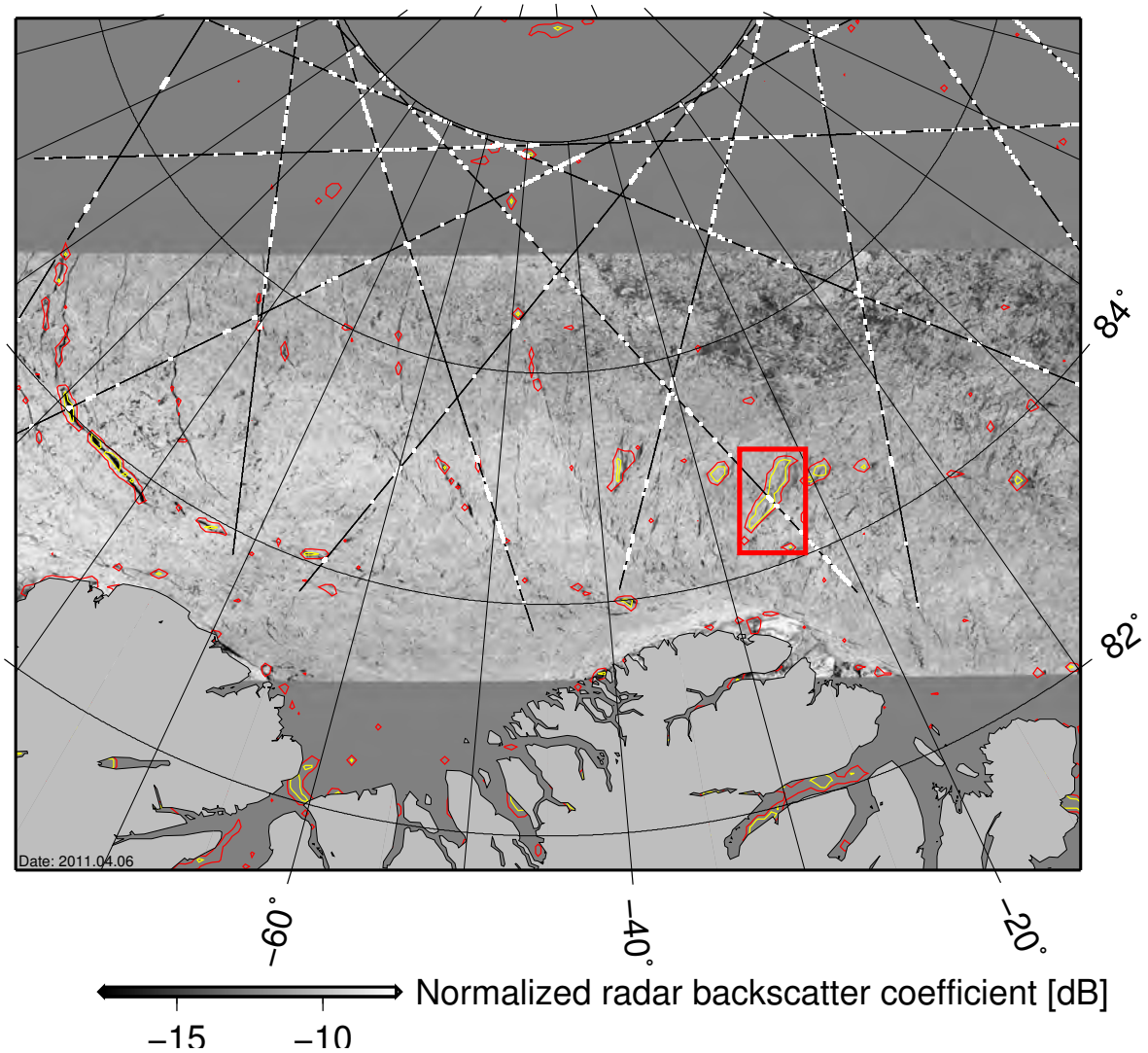

Figure A.3: Multi-sensor comparison: Composite of ASAR scenes depicted as normalized radar backscatter coefficient [dB], AMSR-E LC [%] (red isoline - 25 %, yellow isoline - 75 %), and lead positions from CryoSat-2 (white dots on top of the black CryoSat-2 track) north of Greenland on 6 April 2011. The red box marks the position of an opening lead with a long lifetime.

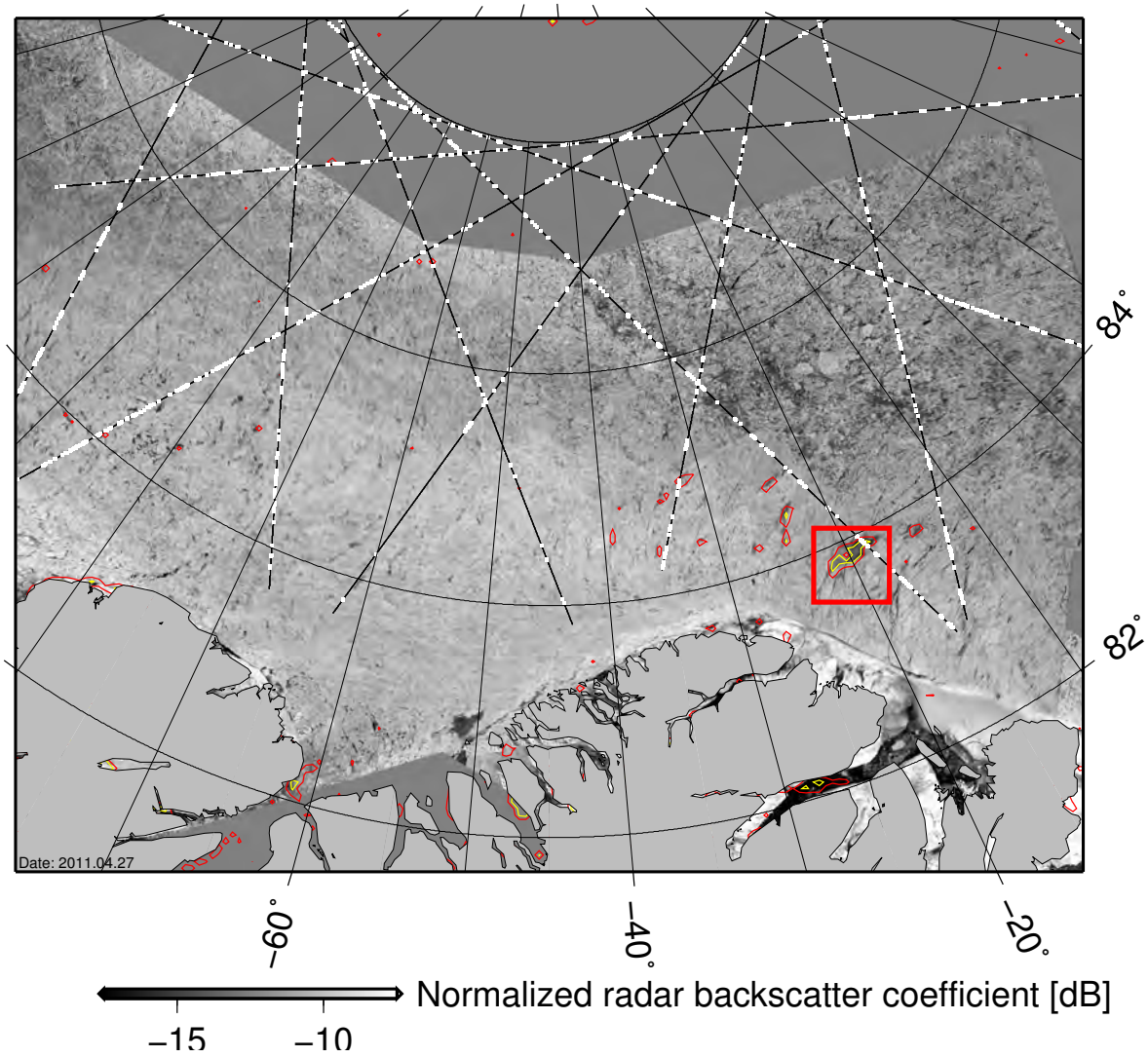

Figure A.4: Multi-sensor comparison: Composite of ASAR scenes depicted as normalized radar backscatter coefficient [dB], AMSR-E LC [%] (red isoline - 25 %, yellow isoline - 75 %), and lead positions (white dots on top of the black CryoSat-2 track) from CryoSat-2 north of Greenland on 27 April 2011. The red box marks the last observed position of a lead with a long lifetime.

A.2 Automatic Estimation of Lead Orientation

Listing A.1: Source code written in the programming language python for a function to calculate the angular standard deviation: The function needs as input a set of orientations θ_i and their corresponding mean value $\overline{\theta}$.

```
def std_ang(theta_i, theta_m):

    '''Algorithm to estimate the standard deviation of
    N lead orientations.

    Usage: astd = std_ang(angles, mean_angle)
    theta_i - np.array containing angles [degree]
    theta_m - mean value of angle array'''

    theta_diff = theta_i.max() - theta_i.min()

    if theta_diff <= 90.:
        angular_std = theta_i.std()
    else:
        theta_d = sqrt((theta_i - theta_m)**2)
        theta_out = theta_i[theta_d>90.]

        if  theta_m > 90. and theta_out.all() > 90.:
            theta_tmp = 180. - theta_m
            theta_d[theta_d>90] = sqrt((theta_out + theta_tmp)**2)
        else:
            theta_tmp = 180. - theta_out
            theta_d[theta_d>90.] = sqrt((theta_tmp - theta_m)**2)

        N = theta_i.shape[0]
        angular_std = sqrt((1./N)*np.sum(theta_d**2))

    return(angular_std)
```

Table A.1: 50 Hough input parameter combinations (threshold value (thres) and minimal line length (mll)) ranked according to the C-score for a test period covering the whole Arctic and lasting from February to April 2011.

rank	1	2	3	4	5	6	7	8	9	10	11	12	13	14	15	16	17
thres	38	31	15	48	40	36	35	29	26	25	23	22	20	17	13	50	48
mll	6	5	5	5	5	8	6	6	5	6	5	5	5	5	6	5	8
rank	18	19	20	21	22	23	24	25	26	27	28	29	30	31	32	33	34
thres	47	46	45	44	43	42	42	41	37	37	37	34	33	29	28	27	26
mll	7	6	7	5	5	8	6	6	7	6	5	6	5	5	8	5	6
rank	35	36	37	38	39	40	41	42	43	44	45	46	47	48	49	50	
thres	25	24	22	21	13	11	10	50	48	47	47	46	43	42	41	41	
mll	5	6	6	5	5	5	6	6	6	6	5	5	8	5	7	5	

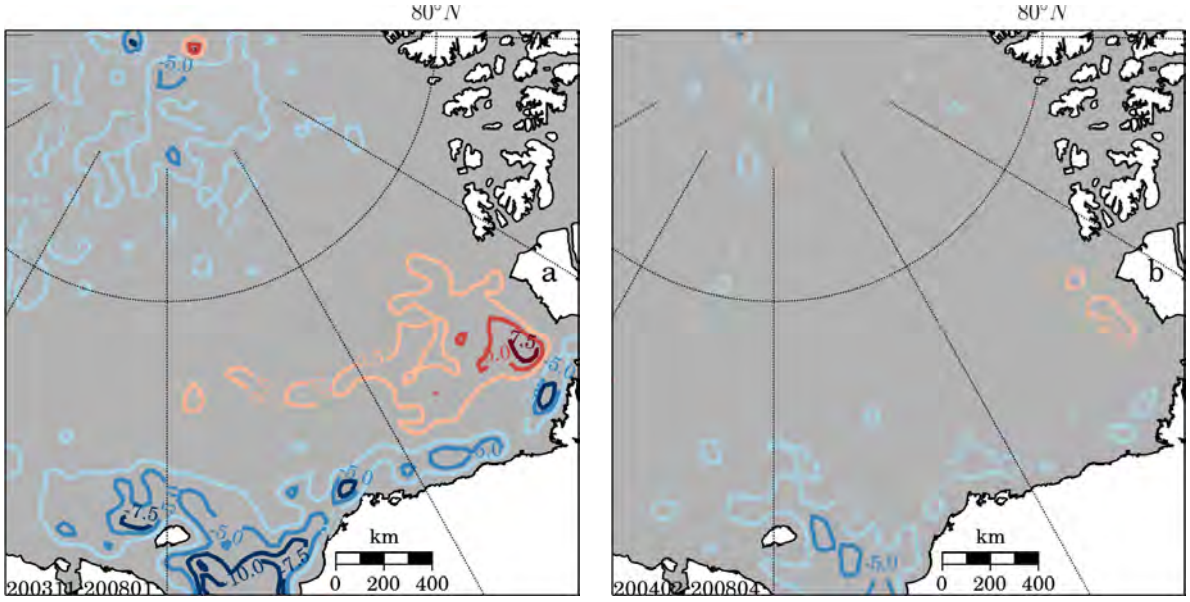

Figure A.5: Seasonally averaged sea-ice divergence in the Beaufort Sea for fall (NDJ) (**a**) and winter (FMA) (**b**) between 2003 and 2008. Divergence is depicted by contoured lines and the unit is 10^{-8} sec^{-1} similar to Miles and Barry (1998). Positions of maximal and minimal divergence are shifted in comparison to the similar Figure 7 in Miles and Barry (1998). Furthermore, the divergence values exceed the values of Miles and Barry (1998) by approximately a factor of 2. Ifremer provides the AMSR-E based 2-day sea-ice drift with a grid resolution of 31.25 km $\times$ 31.25 km.

A.3 Comparison of Leads and Sea-Ice Deformation

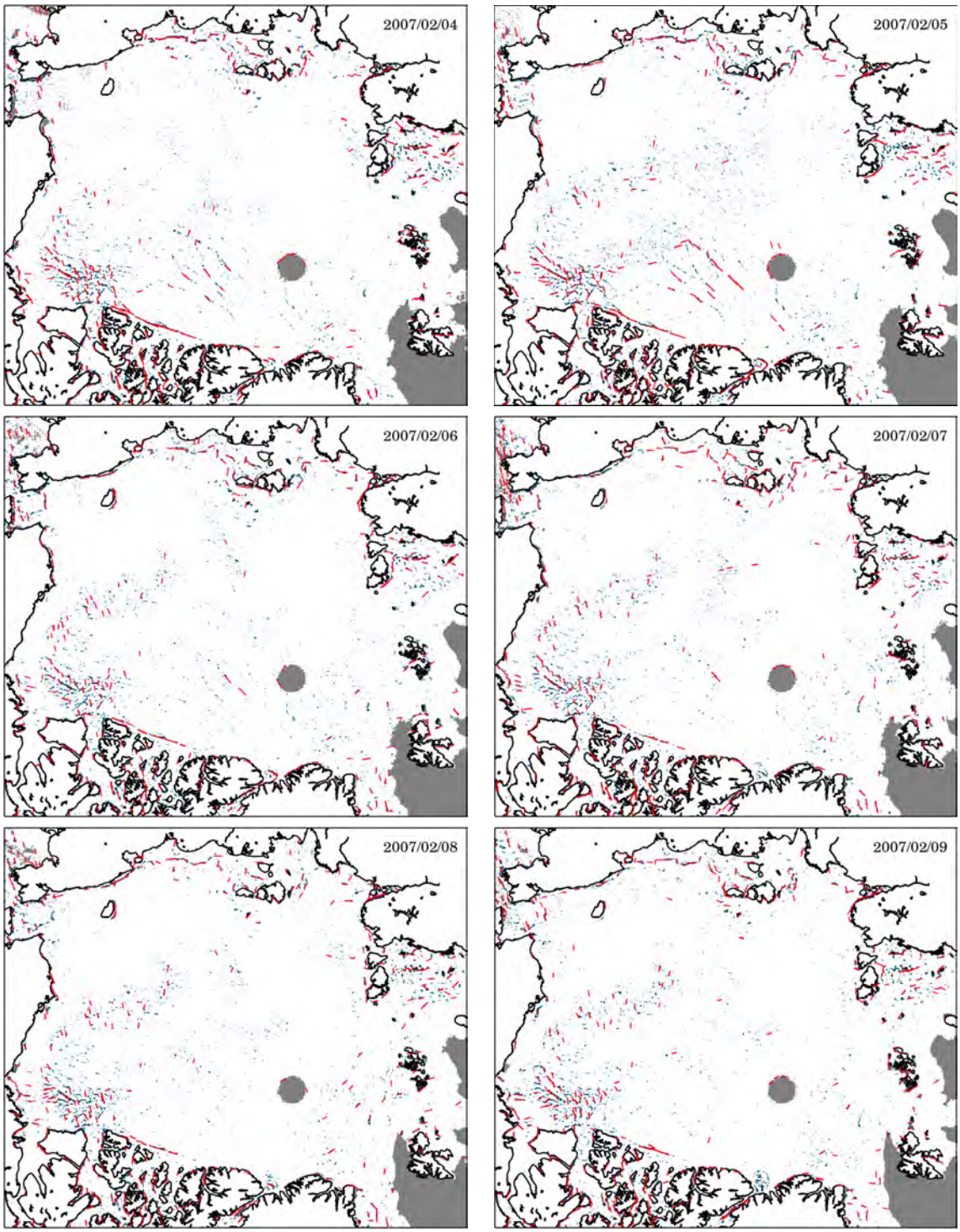

Figure A.6: Lead concentration (blueish pixels) and positions (orientation) (red lines) derived by the Hough transform in the Arctic from 4 February to 9 February 2007.

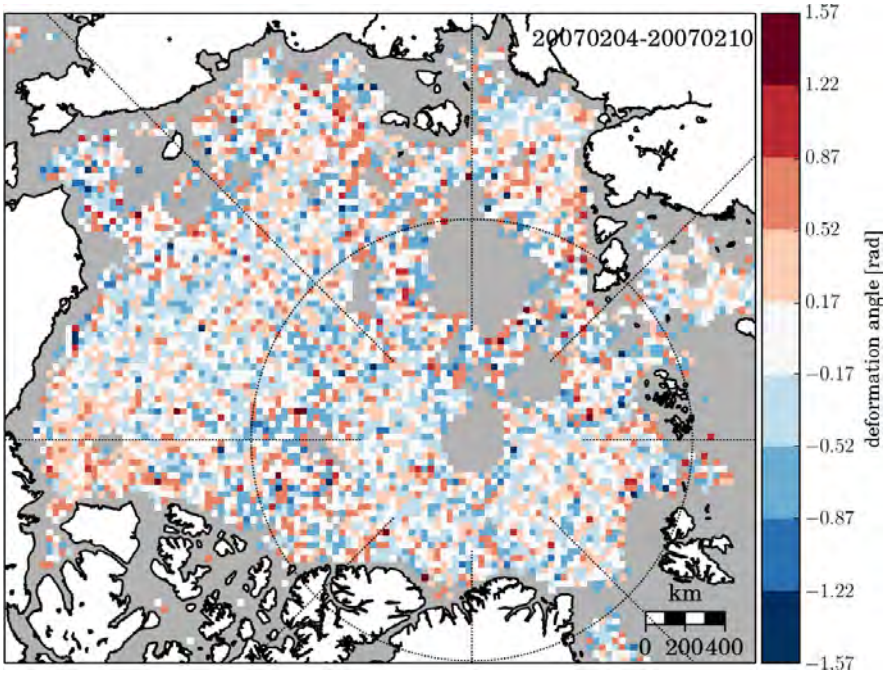

Figure A.7: Ratio between divergence, shear rate, and convergence (Unit: [rad]) (equation (5.7)) calculated from the mean sea-ice drift in the Arctic between 4 February and 10 February 2007. Ifremer provides the AMSR-E based 2-day drift. The cell size corresponds to an area of 31.25 km × 31.25 km.

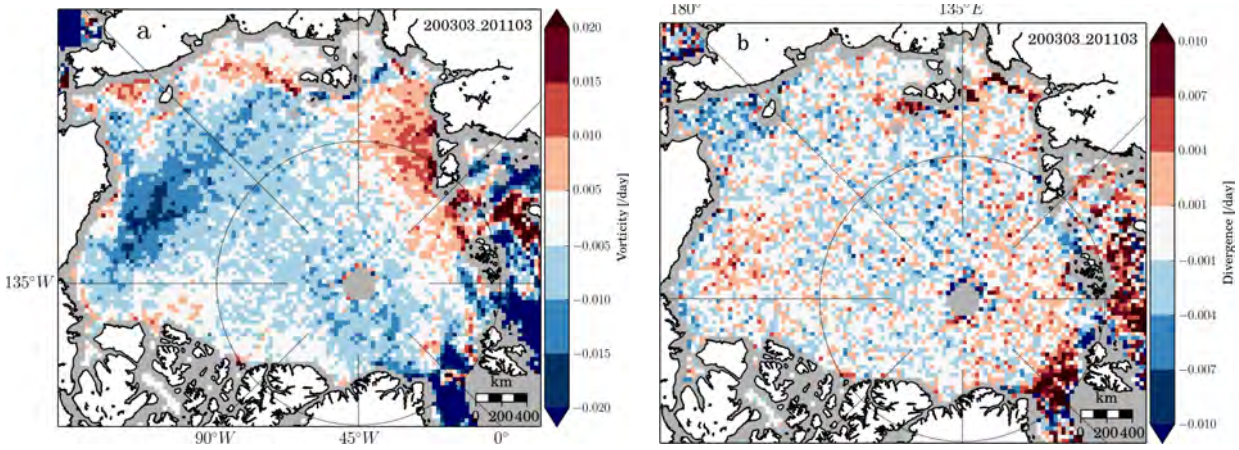

Figure A.8: Monthly averaged vorticity (**a**) and divergence (**b**) in the Arctic for March between 2003 and 2011 (Unit: [/day]). Ifremer provides the AMSR-E based 2-day sea-ice drift from which the deformation parameters are calculated. The cell size corresponds to an area of 31.25 km × 31.25 km.

Acknowledgements

Sincere thanks are given to Prof. Dr. Lars Kaleschke for his ideas concerning this thesis and his supervision of this thesis.

Furthermore, my thanks go to Dr. Dirk Notz for being in my advisory panel and reviewing this work. I thank him for his thoughtful comments regarding the structure of this thesis.

For being my panel chair and being the head of my examining board, I thank Martin Claußen. I thank also Prof. Dr. Hermann Held and Dr. Alexander Löw for being in my examining board.

For financial support, I gratefully acknowledge the Ice Route Optimization - 2 (IRO-2) project. The IRO-2 project is funded by the German Federal Ministry of Economics and Technology from October 2011 to September 2014 in the framework of the program "Shipping and ocean engineering for the 21st century".

For supplying the ASAR WSM images, I thank ESA and JAXA as well as NSIDC for supplying the AMSR-E brightness temperatures. Furthermore, I thank Ifremer for providing the sea-ice drift data and Ron Kwok for providing the high-resolution RGPS sea-ice drift.

I would like to thank for being a member of the International Max Planck Research School on Earth System Modelling (IMPRS-ESM) that helped me to improve my level of conducting science throughout the last three years.

I enjoyed the helpful and productive discussions I had with the sea-ice remote sensing group. In particular, I would like to thank my office fellow Nina Maaß and former office fellow Meike Demgen for their continuous support.

I thank Ulrike Port, Nina Maaß, and Malte Rieck for proofreading parts of this thesis.

Special thanks belong to my family who helped me with their support throughout the time working on this thesis.

David Bröhan
Hamburg, June 2, 2014

List of Figures

List of Tables

References

Bandfield, J. (1992). Skeletal modeling of ice leads. *IEEE Trans. Geosc. Remote Sens.*, 30(5):918–923.

Beitsch, A. and Kaleschke, L. (2013). The February 2013 Arctic Sea Ice Fracture in the Beaufort Sea - a case study for two different AMSR2 sea ice concentration algorithms. *Remote Sens.*

Bluestein, H. (1993). *Synoptic-Dynamic Meteorology in Midlatitudes Vol. I.* Oxford University Press, New York, New York.

Cavalieri, D. (1994). A microwave technique for mapping thin sea ice. *J. Geophys. Res.-Oceancs*, 99:12,561–12,572.

Cavalieri, D. J., Markus, T., and Comiso, J. C. (2003). AMSRE/Aqua Daily L3 12.5 km Brightness Temperature, Sea Ice Concentration, & Snow Depth Polar Grids Ver. 2. Boulder, Colorado USA: NASA DAAC at the National Snow and Ice Data Center.

Cavalieri, D. J., Markus, T., and Comiso, J. C. (2004). AMSRE/Aqua Daily L3 6.25 km 89 GHz Brightness Temperature Polar Grids Ver. 2. Boulder, Colorado USA: NASA DAAC at the National Snow and Ice Data Center.

Duda, R. O. and Hart, P. E. (1972). Use of the Hough Transformation To Detect Lines and Curves in Pictures. *Commun. ACM*, 15:11–15.

Eppler, D. T., Farmer, L. D., Lohanick, A. W., Anderson, M. R., Cavalieri, D. J., Comiso, J., Gloersen, P., Garrity, C., Grenfell, T. C., Hallikainen, M., Maslanik, J. A., Mätzler, C., Melloh, R. A., Rubinstein, I., and Swift, C. T. (1992). *Passive Microwave Signatures of Sea Ice.* Microwave Remote Sensing of Sea Ice. American Geophysical Union, Washington, D. C.

ESA (2004). *ASAR Product Handbook.* European Space Agency.

Ezraty, R., Girard-Ardhuin, F., and Croizé-Fillon, D. (2007). *Sea Ice Drift in the Central Arctic using the 89 GHz Brightness Temperatures of the Advanced Microwave Scanning Radiometer - User's Manual.* CERSAT, IFREMER, 2.0 edition.

Feltham, D. (2008). Sea Ice Rheology. 40.

Fetterer, F. and Holyer, R. (1989). A Hough Transform Technique for Extracting Lead Features from Sea Ice Imagery. *Geoscience and Remote Sensing Symposium*, 2:1125 – 1128.

Galambos, C., Matas, J., and Kittler, J. (2002). Progressive probabilistic hough transform for line detection. *Proceedings 1999 IEEE Computer Society Conference on Computer Vision and Pattern Recognition Cat No PR00149*, 1:554–560.

Giles, K., Laxon, S., Ridout, A., Wingham, D., and Bacon, S. (2012). Western arctic ocean freshwater storage increased by wind-driven spin-up of the beaufort gyre. *Nature geoscience*, 5(3):194–197.

Girard, L., Bouillon, S., Weiss, J., Amitrano, D., and Fichefet, T. (2011). A new modeling framework for sea-ice mechanics based on elasto-brittle rheology. *Annals of Glaciology*, 52(57):123–132.

Girard, L., Weiss, J., Molines, J. M., Barnier, B., and Bouillon, S. (2009). Evaluation of high-resolution sea ice models on the basis of statistical and scaling properties of arctic sea ice drift and deformation. *Journal of Geophysical Research*, 114.

Girard-Ardhuin, F., Ezraty, R., Croizé-Fillon, D., and Piollé, J.-F. (2008). *Sea Ice Drift in the Central Arctic combining QuikSCAT and SSM/I Sea Ice Drift Data - User's Manual*. CERSAT, IFREMER, 3.0 edition.

Grenfell, T., Barber, D., Fung, A., Gow, A., and Jezek, K. (1998). Evolution of Electromagnetic Signatures of Sea Ice from Initial Formation to the Establishment of Thick First-Year Ice. *IEEE Transactions on Geoscience and Remote Sensing*, 36(5):1642–1654.

Gross, D., Hauger, W., Schröder, J., and Wall, W. A. (2007). *Technische Mechanik 2: Band 2: Elastostatik (Springer-Lehrbuch)*. Springer, Berlin, 9. vollst. neu bearb. aufl. edition.

Herman, A. and Glowacki, O. (2012). Variability of sea ice deformation rates in the arctic and their relationship with basin-scale wind forcing. *The Cryosphere*, 6(6):1553–1559.

Heygster, G., Alexandrov, V., Dybkjær, G., von Hoyningen-Huene, W., Girard-Ardhuin, F., Katsev, I. L., Kokhanovsky, A., Lavergne, T., Malinka, A. V., Melsheimer, C., Toudal Pedersen, L., Prikhach, A. S., Saldo, R., Tonboe, R., Wiebe, H., and Zege, E. P. (2012). Remote sensing of sea ice: advances during the damocles project. *The Cryosphere*, 6(6):1411–1434.

Hibler, W. D. (1979). A dynamic thermodynamic sea ice model. *Journal of Physical Oceanography*, 9:815–846.

Hibler, W. D. (2001). Sea ice fracturing on the large scale. *Engineering Fracture Mechanics*, 68:2013–2043.

Hough, P. V. C. (1962). Methods and means for recognizing complex patterns.

Hutchings, J., Heil, P., and Hibler, W. (2005). On modelling Linear Kinematic Features in Sea Ice. *Monthly Weather Review*, 133(12):3481–3497.

Hutchings, J., Roberts, A., Geiger, C., and Menge, J. R. (2011). Spatial and temporal characterization of sea ice deformation. *Annals of Glaciology*, 52(57):360–368.

Integrated Climate Data Center (ICDC) (2013). AMSR-E Lead Area Fraction for the Arctic, [2002-2011]. Available online at `http://icdc.zmaw.de/lead_area_fraction_amsre.html`; visited on 8 March 2014.

Kaleschke, L., Heygster, G., Lpkes, C., Bochert, A., Hartmann, J., Haarpaintner, J., and Vihma, T. (2001). SSM/I sea ice remote sensing for mesoscale ocean-atmosphere interaction analysis: Ice and icebergs. *Can. J. Remote Sens.*, 27:526–537.

Kurtz, N. T., Galin, N., and Studinger, M. (2014). An improved CryoSat-2 sea ice freeboard and thickness retrieval algorithm through the use of waveform fitting. *The Cryosphere Discussions*, 8(1):721–768.

Kwok, R. (1998). The RADARSAT Geophysical Processor System. In Tsatsoulis, C. and Kwok, R., editors, *Analysis of SAR data of the Polar Oceans: Recent Advances*, pages 235–257. Springer Verlag, Berlin Heidelberg.

Kwok, R. (2001). Deformation of the Arctic Ocean sea ice cover: November 1996 through April 1997. In Dempsey, J. and Shen, H. H., editors, *Scaling Laws in Ice Mechanics and Dynamics*, pages 315–322. Kluwer Academic, Dordrecht.

Kwok, R. (2006). Contrasts in sea ice deformation and production in the Arctic seasonal and perennial ice zones. *Journal of Geophysical Research*, 111(C11).

Kwok, R., Pedersen, L. T., P., G., and Pang, S. S. (2010). Large sea ice outflow into the Nares Strait in 2007. *Geophysical Research Letters*, 37.

Kwok, R. and Sulsky, D. (2010). Arctic Ocean Sea Ice Thickness and Kinematics - Satellite Retrievals and Modeling. *Oceanography*, 23(4):134–143.

Leppäranta, M. (2005). *The Drift of Sea Ice*. Springer-Verlag.

Lindsay, R. and Rothrock, D. (1995). Arctic Sea-Ice Leads from Advanced Very High-Resolution Radiometer Images. *Journal of Geophysical Research-Oceans*, 100(C3):4533–4544.

Lüpkes, C., Vihma, T., Birnbaum, G., and Wacker, U. (2008). Influence of leads in sea ice on the temperature of the atmospheric boundary layer during polar night. *Geophysical Research Letters*, 35(3).

Mantoviani, P. L., Miranda, N., and Gilles, P. (2009). CRYOSAT Ground Segment Instrument Processing Facility L1b - Products Specification Format. ESA Technical Report CS-RS-ACS-GS-5106, European Space Agency (ESA) and Advanced Computer Systems.

Marcq, S. and Weiss, J. (2012). Influence of sea ice lead-width distribution on turbulent heat transfer between the ocean and the atmosphere. *The Cryosphere*, 6(1):143–156.

Mardia, K. and Jupp, P. (2000). *Directional Statistics*. Wiley.

Marsan, D., Stern, H., Lindsay, R., and Weiss, J. (2004). Scale dependence and localization of the deformation of arctic sea ice. *Phys. Rev. Lett.*, 93:178501.

Martin, S. (2001). Polynyas. In Steele, J. H., Thorpe, S., and Turekian, K. K., editors, *Encyclopedia of Ocean Sciences, Volume 4: N-R*, pages 540–545. Academic Press.

McCandless, S. and Jackson, C. (2004). Principles of Synthetic Aperature Radar. In Jackson, C. and Apel, J., editors, *Synthetic Aperture Radar Marine User's Manual*, chapter 1. National Oceanic and Atmospheric Administration (NOA), Global Ocean Associates (GOA), 1st edition.

Miles, M. W. and Barry, R. G. (1998). A 5-year satellite climatology of winter sea ice leads in the western Arctic. *J. Geophys. Res.*, 103(D10):21,723–21,734.

Morison, J., Kwok, R., Peralta-Ferriz, C., Alkire, M., Rigor, I., Andersen, R., and Steele, M. (2012). Changing arctic ocean freshwater pathways. *Nature*, 481(7379):66–70.

Olason, E. O. (2012). *Dynamical modelling of Kara Sea land-fast ice*. phdthesis, University of Hamburg, Hamburg, Germany.

Olson, E. (2011). On computing the average orientation of vectors and lines. In *On computing the average orientation of vectors and lines*, 2011 IEEE International Conference on Robotics and Automation (ICRA), pages 3869–3874.

Onstott, R. and Suchman, R. (2004). SAR Measurements of Sea Ice. In Jackson, C. and Apel, J., editors, *Synthetic Aperture Radar Marine User's Manual*, chapter 3. National Oceanic and Atmospheric Administration (NOA), Global Ocean Associates (GOA), 1st edition.

Perovich, D., Longacre, J., Barber, D., Maffione, R., Cota, G., Mobley, C., Gow, A., and Onstott, R. (1998). Field Observations of the Electromagnetic Properties of First-Year Sea Ice. *IEEE Transactions on Geoscience and Remote Sensing*, 36(5):1705–1715.

Pinto, J., Alam, A., Maslanik, J., Curry, J., and Stone, R. (2003). Surface characteristics and atmospheric footprint of springtime Arctic leads at SHEBA. *Journal of Geophysical Research*, 108(C4).

Rampal, P., Weiss, J., and Marsan, D. (2009). Positive trend in the mean speed and deformation rate of arctic sea ice, 1979–2007. *J. Geophys. Res.*, 114(C5).

Röhrs, J., Kaleschke, L., Bröhan, D., and Siligam, P. (2012). An algorithm to detect sea ice leads using AMSR-E passive microwave imagery. *The Cryosphere*, 6(2):365–365.

Rothrock, D. (1975). The energetics of the plastic deformation of pack ice by ridging. *Journal of Geophysical Research*, 80(33):4514–4519.

Sandven, S., Laxon, S., Drange, H., Lisaether, K., Sagen, H., and Evensen, G. (2001). The quantification of the Importance of the Sea Ice Budget in the Climate System. NERSC Technical Report 207, Nansen Environmental and Remote Sensing Center (NERSC) and University College London (UCL).

Schulson, E. (2004). Compressive shear faults within arctic sea ice: Fracture on scales large and small. *Journal of Geophysical Research: Oceans*, 109(C7).

Schulson, E. and Hibler, W. (1991). The fracture of ice on scales large and small: Arctic leads and wing cracks. *Journal of Glaciology*, 37(127):319–322.

Scott, D. W. (1992). *Multivariate Density Estimation: Theory, Practice, and Visualization (Wiley Series in Probability and Statistics)*. Wiley, 1 edition.

Siligam, P. K. (2012). An algorithm to detect leads in sea ice using CryoSat-2 SAR level-1b data.

Smith, S. D., Muench, R. D., and Pease, P. H. (1990). Polynyas and Leads: An Overview of Physical Processes and Environment. *Journal of Geophysical Research*, 95(C6):9461–9479.

Spreen, G., Kaleschke, L., and Heygster, G. (2008). Sea ice remote sensing using AMSR-E 89-Ghz channels. *Journal of Geophysical Research*, 113(C2).

Spreen, G., Kern, S., Stammer, D., and Hansen, E. (2009). Fram Strait sea ice volume export estimated between 2003 and 2008 from satellite data. *Geophysical Research Letters*, 36(19).

Steiner, N. S., Lee, W. G., and Christian, J. R. (2013). Enhanced gas fluxes in small sea ice leads and cracks: Effects on CO2 exchange and ocean acidification. *Journal of Geophysical Research: Oceans*, 118(3):1195–1205.

Stern, H. and Lindsay, R. (2009). Spatial scaling of Arctic sea ice deformation. *Journal of Geophysical Research*, 114.

Sulsky, D. and Peterson, K. (2011). Towards a new elastic-decohesive model of Arctic sea ice. *Physica D. Nonlinear phenomena*, 240(20):1674 – 1683.

Thorndike, A., Rothrock, D., Maykut, G., and Colony, R. (1975). The Thickness Distribution of Sea Ice. *Journal of Geophysical Research*, 80(33):4501–4513.

Tonboe, R. T. (2010). The simulated sea ice thermal microwave emission at window and sounding frequencies. *Tellus. Series A, Dynamic meteorology and oceanography*, 62(3):333–344.

Tsamados, M., Feltham, D. L., and Wilchinsky, A. V. (2013). Impact of a new anisotropic rheology on simulations of Arctic sea ice. *J. Geophys. Res. Oceans*, 118(1):91–107.

Ulaby, F. T., Moore, R. K., and Fung, A. K. (1981). *Microwave Remote Sensing - Active and Passive - Vol I. - Microwave Remote Sensing Fundamentals and Radiometry*. Remote sensing. Addison-Wesley Norwood, Ma, Reading, Ma, London, Amsterdam.

Ulaby, F. T., Moore, R. K., and Fung, A. K. (1986). *Microwave Remote Sensing - Active and Passive - Vol III. - From Theory to Applications*. Remote sensing. Addison-Wesley Norwood, Ma, Reading, Ma, London, Amsterdam.

Wensnahan, M., Maykut, G., Grenfell, T., and Winebrenner, D. (1993). Passive microwave remote sensing using a pricipal component analysis. *J. Geophys. Res.-Oceans*, 98:12,453–12,468.

Wilchinsky, A. and Feltham, D. (2004). A continuum anisotropic model of sea-ice dynamics. *Proceedings - Royal Society. Mathematical, physical and engineering sciences*, 460(2047):2105–2140.

Wilchinsky, A. and Feltham, D. (2012). Rheology of discrete failure regimes of anisotropic sea ice. *Journal of physical oceanography*, 42(7):1065–1082.

Willmes, S., Nicolaus, M., and Haas, C. (2013). The microwave emissivity variability of snow covered first-year sea ice from late winter to early summer: a model study. *The Cryosphere Discussions*, 7(6):5711–5734.

Wingham, D. J., Francis, C. R., Baker, S., Bouzinac, C., and Brockley, D. (2006). Cryosat: A mission to determine the fluctuations in earth's land and marine ice fields. *Advances in Space Research*, 37(4):841–871.

Yu, J., Liu, A. K., Yang, Y., and Zhao, Y. (2013). Analysis of sea ice motion and deformation using AMSR-E data from 2005 to 2007. *International Journal of Remote Sensing*, 34(12):4127–4141.

Zakhvatkina, N., Alexandrov, V., Johannessen, O., Sandven, S., and Frolov, I. (2013). Classification of sea ice types in envisat synthetic aperture radar images. *IEEE Transactions on Geoscience and Remote Sensing*, 51(5):2587–2600.

Zygmuntowska, M., Khvorostovsky, K., Helm, V., and Sandven, S. (2013). Waveform classification of airborne synthetic aperture radar altimeter over Arctic sea ice. *The Cryosphere*, 7(4):1315–1324.

Aus dieser Dissertation hervorgegangene Vorveröffentlichungen

Röhrs, J., Kaleschke, L., **Bröhan, D.**, and Siligam, P. (2012). An algorithm to detect sea ice leads using AMSR-E passive microwave imagery. The Cryosphere, 6(2):343-352.

Bröhan, D., Kaleschke, L. (2014). A Nine-Year Climatology of Arctic Sea Ice Lead Orientation and Frequency from AMSR-E. Remote Sens., 6(2):1451-1475.

Erklärung

Hiermit erkläre ich an Eides statt, dass ich die vorliegende Dissertationsschrift selbst verfasst und keine anderen als die angegebenen Quellen und Hilfsmittel benutzt habe.

Hamburg, den 2. Juni 2014

David Bröhan

Die gesamten Veröffentlichungen in der Publikationsreihe des MPI-M
„Berichte zur Erdsystemforschung“,
„Reports on Earth System Science“,
ISSN 1614-1199

sind über die Internetseiten des Max-Planck-Instituts für Meteorologie erhältlich:

http://www.mpimet.mpg.de/wissenschaft/publikationen.html



ISSN 1614-1199